

POSITIVE ANISOTROPIC GROUP SCATTERING
CROSS SECTIONS FOR RADIATION
TRANSPORT

DISSERTATION

J. Mark DelGrande, Major, USAF
AFIT/DS/ENP/99-03

19990823 090

DEPARTMENT OF THE AIR FORCE
AIR UNIVERSITY
AIR FORCE INSTITUTE OF TECHNOLOGY

Wright-Patterson Air Force Base, Ohio

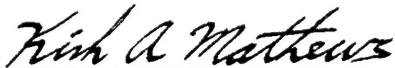
Approved for Public Release; Distribution unlimited

DTIC QUALITY INSPECTED 4

POSITIVE ANISOTROPIC GROUP
SCATTERING CROSS SECTIONS
FOR RADIATION TRANSPORT

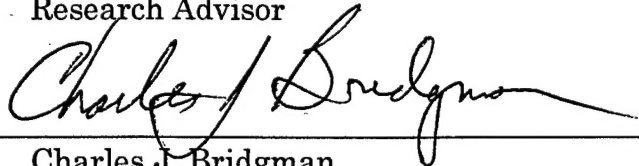
J. Mark DelGrande, B.S., M.S.
Major, USAF

Approved:



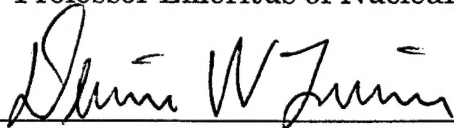
Kirk A. Mathews
Associate Professor of Nuclear Engineering
Research Advisor

16 July 1999



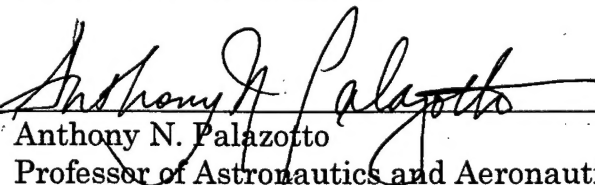
Charles J. Bridgman
Professor Emeritus of Nuclear Engineering

16 JULY '99



Dennis W. Quinn
Professor of Mathematics

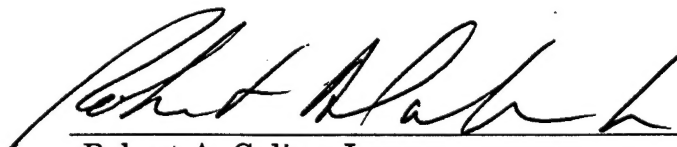
16 JULY '99



Anthony N. Palazotto
Professor of Astronautics and Aeronautics
Dean's Representative

16 July 99

Accepted:



Robert A. Calico, Jr.
Dean, Graduate School of Engineering

POSITIVE ANISOTROPIC GROUP SCATTERING
CROSS SECTIONS FOR RADIATION TRANSPORT

DISSERTATION

Presented to the Faculty of the School of Engineering
Of the Air Force Institute of Technology
Air University in Partial Fulfillment of the
Requirements for the Degree of
Doctor of Philosophy

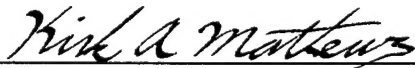
J. Mark DelGrande, B.S., M.S.
Major, USAF
May 1999

Approved for Public Release; distribution unlimited

POSITIVE ANISOTROPIC GROUP
SCATTERING CROSS SECTIONS
FOR RADIATION TRANSPORT

J. Mark DelGrande, B.S., M.S.
Major, USAF

Approved:



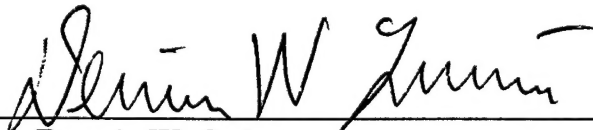
Kirk A. Mathews
Associate Professor of Nuclear Engineering
Research Advisor

15 JULY 1999



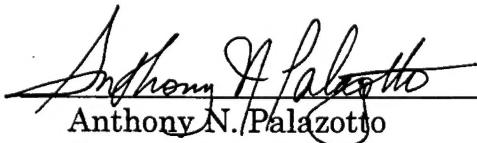
Charles J. Bridgman
Professor Emeritus of Nuclear Engineering

15 July 1999



Dennis W. Quinn
Professor of Mathematics

15 JULY 1999



Anthony N. Palazotto
Professor of Astronautics and Aeronautics
Dean's Representative

15 July 1999

ACKNOWLEDGEMENTS

In the dimly lit, hazy world of doctoral research, sometime the shifting sands of science, sometimes the fickle fate of physics, and sometimes just plain dumb luck lead to something truly spectacular. This isn't one of those times. This work is the result of hard work, determination and the help of a number of people.

I am thankful to my committee members Dr. Charles Bridgman and Dr. Dennis Quinn, who have consistently offered their advice and, more importantly, words of encouragement. I am grateful to the efforts of Dr. Rodney Miller, who's development of the transport code TETRAN, made analysis of my cross section libraries possible. I'm thankful to Dr. Kirk Mathews, my advisor, whose inventiveness and insight has guided me to try novel approaches and innovative techniques. I am forever indebted to my wife, Angela and our children Mason, Antonio, and Ariacella whose steadfast love and support have made these years in Dayton truly wonderful.

TABLE OF CONTENTS

ACKNOWLEDGEMENTS	III
TABLE OF CONTENTS	IV
LIST OF FIGURES	VI
ABSTRACT	IX
NEUTRON TRANSPORT WITH HIGHLY ANISOTROPIC SCATTERING	1
1. INTRODUCTION	1
2. THE DISCRETE ORDINATES METHOD	5
Energy Discretization	6
Angular Discretization	8
Material Dependence	9
3. CALCULATING THE MULTIGROUP SCATTERING CROSS SECTION	11
Using Spherical Harmonics	12
4. ATTEMPTS TO FIX NEGATIVITY	17
Exact Ordinate-to-Ordinate Scatter	17
Non-negative Functional Scattering Cross Section Representation	22
Use of Piecewise Constant Functions	24
The Monte Carlo Facet Method	29
Advantages of the MC Facet Method	37
5. IMPLICATIONS OF FACET TRANSFERS ON NEUTRAL PARTICLE TRANSPORT	39
Effect of Scatter Averaging	39
Standard MC Facet Method Implementation	40
6. DESCRIPTION OF THE MONTE CARLO TRANSPORT APPROACH	42
Sample the Incident Energy	43
Sample Incident Direction	43
Select the Collision Nuclide	49
Determine Type of Scatter	50
Finding the New Direction	58
Identifying Scattered Energy Group and Facet	60
7. CONSERVING THE FIRST ANGULAR MOMENT OF THE T-MATRIX	63
The P_1 Approximation and Diffusion Theory	63
Validity of the MC Facet Method in the Diffusion Limit	65
T-Matrix Rebalance to Conserve First Angular Moment	67
Process of Rebalancing	69
Results of the First Moment Rebalance	77
General Summary of First Moment Conservation	82
8. CODE DEVELOPMENT, CAPABILITIES AND OPERATION	85
From Continuous to Discrete: The Path for Benchmarking	85
The Triad of Discretization	86
Cross Section Libraries	88
T-Scat's Current Capabilities	92
9. CALCULATIONS: INVESTIGATIONS OF THE T-MATRIX	101
Visualizing the Scattering Physics	102
Visualizing the physics of group-to-group scatter	110
Convergence, Error Tracking and Calculation Time	117
The MC Facet Approach vs. the Spherical Harmonic Method	127

The Impact of the Angular Quadrature	133
Angular Dispersion.....	139
The Effects of Angular Rebalance	140
Scattering Matrix Conclusions	144
10. TRANSPORT CODE PERFORMANCE.....	146
Overview of the Transport Codes	147
Nuclides Investigated	148
Definition of Terms.....	148
Uniform Cube Test Problems.....	151
Nested Cube Test Problems	170
Transport Summary	182
11. CONCLUSIONS.....	184
APPENDIX A: SAMPLE MEAN MONTE CARLO INTEGRATION	186
APPENDIX B: THE INELASTIC NEUTRON SCATTERING LAWS OF MCNP.....	188
APPENDIX C: SCATTERING LEVELS OF OXYGEN (^{16}O).....	189
APPENDIX D: LANL 30 GROUP STRUCTURE	190
APPENDIX E: VITAMIN-J 175 GROUP STRUCTURE.....	191
REFERENCES	192

LIST OF FIGURES

Figure 1. Within group (13.5-14.9 MeV) elastic scattering cross section of ^{238}U (ref. 5).....	1
Figure 2. Group 1→5 scatter for hydrogen, ^1H , in the lab frame.	15
Figure 3. Group-to-group Scattering Geometry ⁵	19
Figure 4. Borsari scattering cross-section p.c.f.	25
Figure 5. Scattering from $\Delta\Omega' \rightarrow \Delta\Omega$	30
Figure 6. 74 Facet Polecap Quadrature.....	43
Figure 7. 74 Facet Structure on a Cartesian map.	44
Figure 8. Quadrature schemes proposed by Lebedev ¹⁹	48
Figure 9. Total collision ^{16}O cross section from ACE file.....	51
Figure 10. Total collision ^{16}O cross section from ACE file (1-20 MeV).....	51
Figure 11. ^1H Equi-Probable Bins Elastic Scattering Table	54
Figure 12. ^7Li Equi-Probable Bins Elastic Scattering Table.....	54
Figure 13. CDF of the CM elastic scatter for ^7Li at 1 and 10 MeV.....	55
Figure 14. Scattered energy spectrum for ^{16}O for incident $E' \in [17.333, 19.64]$	60
Figure 15. Tracking average scattering direction within a facet.....	69
Figure 16. Case 1 rebalance.	70
Figure 17. Geometry for 3-point rebalance.	73
Figure 18. Division of the polecap into sub-facets.	76
Figure 19. Rebalancing between 4-points.	78
Figure 20. Rebalance fractions between F_1 & F_2 with no polar component.....	79
Figure 21. Applying flat thinking to curved surfaces: 4-Point Rebalance.	80
Figure 22. Great circles define the shaded area.	80
Figure 23. Rebalance at the pole. ($\zeta_1 = 0.905$, $\xi_0 = 0.95$)	82
Figure 24. Flow of the Cross-Section Data to the Transport Codes	89
Figure 25. Group size in lethargy for selected group structures	91
Figure 26. 74 Facet Structure.....	94
Figure 27. $T(56 \rightarrow 23)$ facet transfer on the sphere.....	95
Figure 28. Scattering Cone After Collision.	102
Figure 29. Scattering circle of the sphere on a Cartesian map.....	103
Figure 30. Progressive increases in scattering angle on the Cartesian grid.	103
Figure 31. Group-to-group differential scattering cross section of hydrogen.	104
Figure 32. Three dimensional look at within group scatter of ^1H	106
Figure 33. Hydrogen within group scatter showing the explicit facet values.....	107

Figure 34. Hydrogen within group scatter showing the explicit facet values.....	107
Figure 35. 3-Dimensional representation of within group scatter for hydrogen.	108
Figure 36. Explicit representation of T-matrix data as scatter points.....	109
Figure 37. Cartesian contour of the first five scatter groups of hydrogen.	111
Figure 38. Kinematics for the group 1→2 scatter of ^{16}O	113
Figure 39. The scattering of ^{16}O . Group one to the first four groups.....	114
Figure 40. Group-to-group T-matrix of ^{16}O on the Cartesian map (LANL-30 Group).	115
Figure 41. Detail of (1→2) T-matrix scatter of ^{16}O on the Cartesian map.....	116
Figure 42. T value of the oxygen 1→1 group and facet transfer.	118
Figure 43. T value of the oxygen transfer with error bars.....	119
Figure 44. Fractional Error matches $N^{-1/2}$ convergence.....	119
Figure 45. Increasing the number of draws on the $^{16}\text{O}(1\rightarrow 2)$ transfer.	120
Figure 46. Within group scatter $^{16}\text{O}(1\rightarrow 1)$ at 40 million draws.....	122
Figure 47. Absolute error for $^{16}\text{O}(1\rightarrow 1)$ transfer at 5 and 20 million draws.	122
Figure 48. Fractional error of $^{16}\text{O}(1\rightarrow 1)$ transfer (20 million draws).	123
Figure 49. Fractional error of one group, 160 facet isotropic scatter.	124
Figure 50. Run time for a single incident group and facet.....	125
Figure 51. Legendre Expansion of the hydrogen scattering cross section.	128
Figure 52. Cartesian map of the P3 and P7 spherical harmonic expansions of ^1H	129
Figure 53. Group 1→2 transfer for ^{16}O using spherical harmonics.....	130
Figure 54. Group 1→2 transfer for ^{16}O using T-Scat.....	130
Figure 55. Spherical harmonic comparison with T-Scat.....	131
Figure 56. Guaranteed within group scatter [$^1\text{H}(1\rightarrow 1)$] for the MC Facet Method.....	138
Figure 57. Facet angular dispersion for $^1\text{H}(1\rightarrow 1)$ scatter (expanded axis).	139
Figure 58. Reduction of dispersion using angular rebalancing.	141
Figure 59. Effects of angular rebalance for hydrogen (1→1).	142
Figure 60. Effect of angular rebalance for equatorial facets, ^1H (1→1).	142
Figure 61. Rebalance of ^{16}O (1→2) T-matrix for 12 equatorial facets.	143
Figure 62. Rebalance of ^{16}O (1→2) T-matrix for 20 equatorial facets.	144
Figure 63. Dimensions of the simple cube.....	151
Figure 64. Hydrogen cube test problem comparing volume scalar flux.	153
Figure 65. Hydrogen cube volume scalar flux spectrum.	154
Figure 66. Relative difference between TETRAN methods and MCNP (^1H).....	154
Figure 67. Reducing the T-Scat difference by increasing from 74 to 86 facets.....	155
Figure 68. Simple cube for ^{10}B shows marked improvement for T-Scat.	156
Figure 69. Simple cube for ^{10}B shows marked improvement for T-Scat.	156

Figure 70. Hydrogen using VITAMIN-J structure.	157
Figure 71. Error of hydrogen 161 cell cube using fine group structure.	157
Figure 72. Scalar flux for a small number of directional ordinates.....	158
Figure 73. Flux differences for a small number of directional ordinates.	158
Figure 74. Error reduction using finer spatial mesh.....	159
Figure 75. MCSN applied to the 161 cell hydrogen cube.	161
Figure 76. Error of TETTRAN and MCSN methods using T-Scat library.	161
Figure 77. Difference between MCSN and TETTRAN for two spatial meshes.....	162
Figure 78. Transport error may depend on the number of draws.	163
Figure 79. Close look at group two improvement as the number of draws is increased.....	164
Figure 80. Flux comparisons for the water cube.....	165
Figure 81. Error of the methods in the water cube.....	165
Figure 82. Stochastic errors of MCSN and MCNP in the H ₂ O cube.....	166
Figure 83. Effects of rebalancing 74 facets for the hydrogen cube.	167
Figure 84. Total group 1 cube surface currents of H ₂ O cube.	169
Figure 85. Total group 2 cube surface currents of H ₂ O cube	169
Figure 86. Mesh and dimensions of the cube-cube-cube geometry.....	171
Figure 87. Water-iron-water fluxes for six groups.....	172
Figure 88. Presentation of H ₂ O-Fe-H ₂ O differences with MCNP by region.	173
Figure 89. Relative difference in source region of H ₂ O-Fe-H ₂ O problem.....	174
Figure 90. Relative difference in middle region of H ₂ O-Fe-H ₂ O problem	175
Figure 91. Relative difference in outer region of H ₂ O-Fe-H ₂ O problem.....	175
Figure 92. H ₂ O-B-H ₂ O: LC produces negative fluxes in the outer region.....	177
Figure 93. Scalar flux differences of source region relative to MCNP	178
Figure 94. Scalar flux differences of middle region relative to MCNP.....	179
Figure 95. Scalar flux differences of outer region relative to MCNP	179
Figure 96. Scalar flux map of the tetrahedra along the x-axis.	180
Figure 97. Scalar flux from TETTRAN's EC method.....	181
Figure 98. Scalar flux goes negative for water-iron-water problem too.	182

ABSTRACT

In solving the Boltzmann transport equation, most discrete ordinates codes calculate the source term by first approximating the scattering cross section using a Legendre polynomial expansion. Such expansions are insufficient when scattering is anisotropic and the Legendre expansion is truncated prematurely. This can lead to nonphysical negative cross sections, negative source terms and negative angular fluxes. While negative sources are problematic for standard discrete ordinates methods leading to poor convergence or convergence to incorrect results, they are of particular concern to exponential methods, causing such calculations to fail.

We've developed and tested a new technique to solve this problem called the *Monte Carlo Facet Method*. This method is an extension of standard Monte Carlo techniques. It guarantees non-negative cross sections at all directional ordinates. It also ensures within group and next group scatter.

This dissertation outlines previous attempts to handle anisotropic scattering to achieve non-negative sources. It develops the theory of the Monte Carlo facet method and its first angular moment conservation. Results are presented examining the scattering matrices for various materials, and finally demonstrating that these scattering matrices perform exceptionally well in a multi-group, anisotropic, unstructured mesh discrete ordinates transport code.

NEUTRON TRANSPORT WITH HIGHLY ANISOTROPIC SCATTERING

1. Introduction

Open any standard transport textbook from the 50's or 60's, and in the chapter on discrete ordinates, one of the first things you'll need to do is approximate the scattering source with a Legendre polynomial. These codes were run on machines where memory was at a premium. The problem, however, is that such expansions, among other things, lead directly to the calculation of negative scattering sources and, in turn, negative fluxes. This happens when the group-to-group scattering cross section is anisotropic. Polynomials can't easily approximate such behavior (Figure 1).

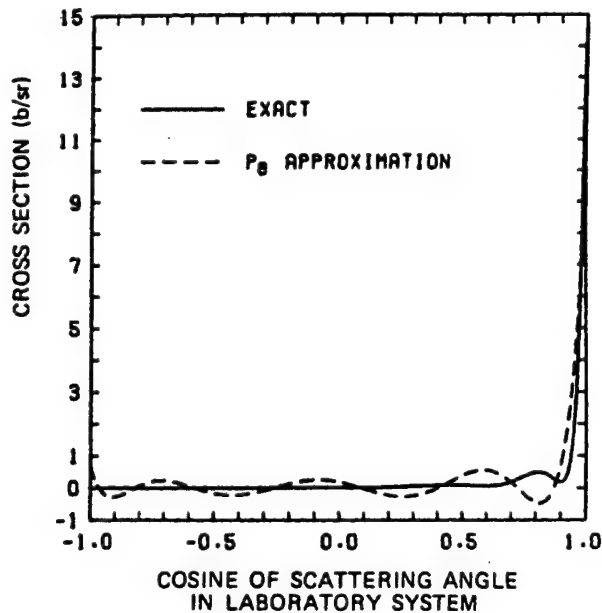


Figure 1. Within group (13.5-14.9 MeV) elastic scattering cross section of ^{238}U (ref. 5).

Today, we have desktop machines with 10 gigabyte hard drives, 100's of megabytes of RAM and processors that outperform the mainframes of yesteryear. Yet, as it was 40 years ago, open up a new transport textbook, and in the chapter on discrete ordinates, you'll still need to approximate the scattering source with a Legendre polynomial.

The point is that even with the advent of new technology, the computational paradigms of the past remain. This research breaks those paradigms and develops a wholly new approach to create scattering cross sections for discrete ordinates codes. In so doing, we demonstrate the ability to perform accurate deep penetration, multi-group, anisotropic scattering transport problems without unphysical artifacts. The solution of such problems is essential to understand and model the penetration of radiation through shields on everything from nuclear reactors to bomb shelters to waste transportation containers.

The dissertation is divided into a number of chapters. The first few look at the discrete ordinates method and solutions to the scattering source. The discrete ordinates method is introduced and the scattering source is defined. Various approaches used in calculating this source for discrete ordinates transport calculations are then compared. In so doing, we show how spherical harmonic (SH) methods using Legendre polynomials lead to negative sources, and how current attempts to solve such negativity are inadequate.

The next few chapters develop the theory of our proposed solution, the Monte Carlo (MC) facet method. This method takes advantage of today's computing power, offers a direct link to the physics of the scattering, and guarantees a non-negative scattering source. The theoretical development of the method is presented as well as the general algorithm the code follows to create the non-negative scattering matrices. Also presented is a method to conserve the first angular moment of the scatter (important in diffusion like problems) for these new scattering matrices.

The next chapter discusses the codes and cross section libraries used for this research. This chapter outlines the benchmarking used and explains the basic operation of the code. It also discusses the capabilities and limitations of the codes developed as part of this research.

The final two chapters present the results. These are broken into two main categories:

1. Results examining the new scattering matrices.
2. Results using those matrices in a transport code.

The first of these chapters demonstrates the non-negativity of the new approach and compares and contrasts this method with other attempts to solve the same problem. The second chapter demonstrates that we're able to perform real transport problems with real materials. It also compares transport results using the facet method to those using the standard spherical harmonic method. What is found is that the MC facet method

provides superior performance while guaranteeing non-negative cross-section data.

2. The Discrete Ordinates Method

This chapter outlines the discretization of the transport equation in energy, angle and space. It begins with the time independent, non-multiplying, transport equation¹,

$$\begin{aligned} \left[\hat{\Omega} \cdot \vec{\nabla} + \sigma(\vec{r}, E) \right] \psi(\vec{r}, \hat{\Omega}, E) \\ = q_{in}(\vec{r}, \hat{\Omega}, E) + \int dE' \int d\Omega' \sigma_s(\vec{r}, E' \rightarrow E, \hat{\Omega}' \cdot \hat{\Omega}) \psi(\vec{r}, \hat{\Omega}', E'), \end{aligned} \quad (1)$$

where ψ is the angular flux, σ is the total macroscopic neutron scattering cross section, and q_{in} is the time independent intrinsic source. The source, $q_{in}(\vec{r}, \hat{\Omega}, E) dV d\Omega dE$, is the rate of source particles emitted in dV about \vec{r} , traveling in a cone of directions $d\Omega$ about $\hat{\Omega}$ with energies between E and $E + dE$, and σ_s is the differential scattering cross section. In general,

$$\sigma_s(\vec{r}, E' \rightarrow E, \hat{\Omega}' \cdot \hat{\Omega}) = \sigma_s(\vec{r}, E') f_s(\vec{r}, E' \rightarrow E, \hat{\Omega}' \rightarrow \hat{\Omega}) \quad (2)$$

where $\sigma_s(\vec{r}, E')$ is the total macroscopic scattering cross section (m^{-1}) and $f_s(\vec{r}, E' \rightarrow E, \hat{\Omega}' \rightarrow \hat{\Omega}) d\Omega dE$ is the conditional probability that, given that an incident neutron of direction Ω' and energy E' is involved in a scattering collision, a scattered neutron will emerge from the collision in the direction interval $d\Omega$ about Ω with energy between E and $E+dE$.² The probability density function is normalized so that $\iint d\Omega dE f_s(\vec{r}, E' \rightarrow E, \hat{\Omega}' \rightarrow \hat{\Omega})$ equals the expectation value of the number of neutrons that emerge from such a scattering collision.

At this point, the scattering source is defined as

$$q^s(\vec{r}, \hat{\Omega}, E) = \int dE' \int d\Omega' \sigma_s(\vec{r}, E' \rightarrow E, \hat{\Omega}' \cdot \hat{\Omega}) \psi(\vec{r}, \hat{\Omega}', E'), \quad (3)$$

where the integration over Ω on the unit sphere, \mathcal{U} , is normalized so that

$$\int_{\mathcal{U}} d\Omega = \int_{-1}^1 \frac{d\xi}{2} \int_0^{2\pi} \frac{d\omega}{2\pi} = 1, \quad (4)$$

and may be approximated by

$$\int_{\mathcal{U}} d\Omega f(\hat{\Omega}) \approx \sum_n w_n f(\hat{\Omega}_n), \quad (5)$$

for some quadrature set, $\{(w_n, \hat{\Omega}_n) | n = 1, \dots, N\}$, where the quadrature weights

are normalized such that

$$\sum_n w_n = 1. \quad (6)$$

Energy Discretization

The BTE, equation (1), is integrated over energy where the energy integral is partitioned into groups. Namely,

$$\int_0^\infty dE = \sum_{g=1}^G \int_{E_g}^{E_{g-1}} dE = \sum_{g=1}^G \int_g dE, \quad (7)$$

where G is the number of energy groups and g is the group number. In general, $E_0 > E_1 > E_2 \dots > E_G = 0$. The first assumption in discrete ordinates is energy separability of the angular flux, so that

$$\psi(\vec{r}, E, \hat{\Omega}) \approx \tilde{W}_g(E) \psi_g(\vec{r}, \hat{\Omega}), \quad (8)$$

where

$$\int_g dE \tilde{W}_g(E) = 1, \quad (9)$$

and \tilde{W}_g is constructed from an assumed energy distribution, $W(E)$ as

$$\tilde{W}_g(E) = \frac{W(E)}{\int_g dE W(E)}. \quad (10)$$

A typical choice is $W(E) = E^{-1}$ often called the slowing down spectrum.

Here, the angular flux $\psi_g(\vec{r}, \hat{\Omega})$ is a group, angular flux, integrated over the given group, and remaining a distribution in $\hat{\Omega}$.

With this assumption, the group form of equation (1) is¹

$$\left[\hat{\Omega} \cdot \vec{\nabla} + \sigma_g(\vec{r}) \right] \psi_g(\vec{r}, \hat{\Omega}) = q_g^{in}(\vec{r}, \hat{\Omega}) + q_g^s(\vec{r}, \hat{\Omega}), \quad (11)$$

where the group variables are defined as

$$q_g^s(\vec{r}, \hat{\Omega}) = \sum_{g'=1}^G \int d\Omega' \sigma_{g'g}^s(\vec{r}, \hat{\Omega}' \cdot \hat{\Omega}) \psi_{g'}(\vec{r}, \hat{\Omega}'), \quad (12)$$

$$\sigma_g(\vec{r}) = \int_g dE \sigma(\vec{r}, E) \tilde{W}_g(E), \quad (13)$$

$$q_g^{in}(\vec{r}, \hat{\Omega}) = \int_g dE q^{in}(\vec{r}, \hat{\Omega}, E), \quad (14)$$

$$\text{and } \sigma_{g'g}^s(\vec{r}, \hat{\Omega}' \cdot \hat{\Omega}) = \int_g dE \int_{g'} dE' \sigma^s(\vec{r}, E' \rightarrow E, \hat{\Omega}' \cdot \hat{\Omega}) \tilde{W}_{g'}(E'). \quad (15)$$

This research seeks an effective approximation of the group scattering source term in equation (11), or using equations (12) through (15),

$$q_g^s(\vec{r}, \hat{\Omega}) = \sum_{g'=1}^G \int d\Omega' \int_g dE \int_{g'} dE' \sigma^s(\vec{r}, E' \rightarrow E, \hat{\Omega}' \cdot \hat{\Omega}) \tilde{W}_{g'}(E') \psi_{g'}(\vec{r}, \hat{\Omega}'). \quad (16)$$

Angular Discretization

Standard discrete ordinates theory assumes that equation (11) holds for N distinct angles ($n=1, 2, \dots, N$) where an appropriate angular quadrature is applied giving

$$[\hat{\Omega}_n \cdot \vec{\nabla} + \sigma_g(\vec{r})] \psi_{g,n}(\vec{r}) \approx q_{g,n}^{in}(\vec{r}) + q_{g,n}^s(\vec{r}), \quad (17)$$

where

$$\begin{aligned} q_{g,n}^s(\vec{r}) &= q_g^s(\vec{r}, \hat{\Omega}_n) \\ &= \sum_{g'=1}^G \int d\Omega' \int_g dE \int_{g'} dE' \sigma^s(\vec{r}, E' \rightarrow E, \hat{\Omega}' \cdot \hat{\Omega}_n) \tilde{W}_{g'}(E') \psi_{g'}(\vec{r}, \hat{\Omega}'). \end{aligned} \quad (18)$$

Applying the angular quadrature, equation (5),

$$q_{g,n}^s(\vec{r}) = \sum_{g'=1}^G \sum_{n'=1}^N w_{n'} \sigma_{g'g}^s(\vec{r}, \hat{\Omega}_{n'} \cdot \hat{\Omega}_n) \psi_{g',n'}(\vec{r}), \quad (19)$$

so that, using the definition of $\sigma_{g'g}^s$,

$$q_{g,n}^s(\vec{r}) = \sum_{g'=1}^G \sum_{n'=1}^N w_{n'} \int_g dE \int_{g'} dE' \sigma^s(\vec{r}, E' \rightarrow E, \hat{\Omega}_{n'} \cdot \hat{\Omega}_n) \tilde{W}_{g'}(E') \psi_{g',n'}(\vec{r}) . \quad (20)$$

With this notation, $\psi_{g,n}(\vec{r})$, is the angular flux integrated over group g , evaluated at the directional ordinate $\hat{\Omega}_n$. Similarly, $q_{g,n}^s(\vec{r})$ is the scattered group source evaluated at the directional ordinate $\hat{\Omega}_n$.

Material Dependence

While the source and angular flux may vary through a single material as \vec{r} changes, it is assumed here that the total and scattering cross sections do not. While the cross sections differ among materials, there is no variation within any single material. Hence, $\sigma^s(\vec{r}, E' \rightarrow E, \hat{\Omega}_{n'} \cdot \hat{\Omega}_n)$ can really be thought of as $\sigma_{material(\vec{r})}^s(E' \rightarrow E, \hat{\Omega}_{n'} \cdot \hat{\Omega}_n)$ or $\sigma_{m(\vec{r})}^s(E' \rightarrow E, \hat{\Omega}_{n'} \cdot \hat{\Omega}_n)$. Unless specifically required, the material dependence can be assumed for all cross sections, and the \vec{r} or *material* designation will be left out of further derivations. The scattering source is then written as

$$q_{g,n}^s(\vec{r}) = \sum_{g'=1}^G \sum_{n'=1}^N w_{n'} \int_g dE \int_{g'} dE' \sigma^s(E' \rightarrow E, \hat{\Omega}_{n'} \cdot \hat{\Omega}_n) \tilde{W}_{g'}(E') \psi_{g',n'}(\vec{r}) \quad (21)$$

Most modern transport codes approximate this scattering source with a truncated spherical harmonics expansion. This leads to the calculation of negative sources when the scattering is anisotropic. Such an expansion, and

attempts to eliminate negative cross sections and hence, negative sources are discussed in the following chapter.

3. Calculating the Multigroup Scattering Cross Section

The previous chapter developed the standard discrete ordinates theory leading to the definition of the scattering source term. This chapter examines the standard method used to calculate the scattering source, namely the use of Legendre polynomials to approximate $\sigma_{g'g}^s(\hat{\Omega}_{n'} \cdot \hat{\Omega}_n)$.

In the past, direct calculation of the scattering source in equation (19) was impossible because of the memory requirement to store the scattering matrix. A typically used, S_8 , quadrature in three dimensions consists of 80 angular directions. If equation (19) is used directly for each ordinate, then

$\sigma_{g'g}^s(\hat{\Omega}_{n'} \cdot \hat{\Omega}_n)$ is an 80x80 matrix for each group-to-group transfer for each material used in the problem. For a group structure consisting of 30 groups the cross-section matrix, $\sigma_{g'g}^s(\hat{\Omega}_{n'} \cdot \hat{\Omega}_n)$ consists of $N^2 G^2 = 5,760,000$ elements. Stored as four-byte floating-point numbers, the file containing the matrix would be large, about 20 Mbytes. A further memory penalty is that the angular flux values for each group and angle, $\psi_{g'n'}$, must be stored for the source calculations of all lower groups ($g > g'$), assuming down scatter only. Historically, authors of production codes have considered this too heavy a computational cost. With the increased memory and storage capabilities of modern machines, the storage difficulties become less and less an issue. In fact, we will demonstrate later that such codes can be run on even a desktop machine. Still, problems requiring a large number of materials and fine

discretizations in space, angle and energy may not be able to accept the storage and memory burden of direct calculation. They require that the source be approximated with spherical harmonics.

Using Spherical Harmonics

This method is the dominant method among production codes and transport texts. The group-to-group scattering cross section is approximated by¹

$$\sigma_{g'g}^s(\hat{\Omega}_{n'} \cdot \hat{\Omega}_n) \approx \sum_{l=0}^L (2l+1) \sigma_{lg'g}^s P_l(\hat{\Omega}_{n'} \cdot \hat{\Omega}_n), \quad (22)$$

where P_l are the Legendre polynomials and $\sigma_{lg'g}^s$ are the Legendre coefficients of the group-to-group scattering cross section found from

$$\sigma_{lg'g}^s = \int_{g'} dE' \int_g dE \sigma_l^s(E' \rightarrow E) \tilde{W}(E'). \quad (23)$$

The addition theorem for Legendre polynomials is

$$P_l(\hat{\Omega}_{n'} \cdot \hat{\Omega}_n) = \frac{1}{2l+1} \sum_{m=-l}^l Y_{lm}^*(\hat{\Omega}_{n'}) Y_{lm}(\hat{\Omega}_n), \quad (24)$$

where the Y_{lm} are the normalized spherical harmonics¹. Using this substitution, the scattering cross section is

$$\sigma_{g'g}^s(\hat{\Omega}_{n'} \cdot \hat{\Omega}_n) \approx \sum_{l=0}^L \sum_{m=-l}^l \sigma_{lg'g}^s Y_{lm}^*(\hat{\Omega}_{n'}) Y_{lm}(\hat{\Omega}_n). \quad (25)$$

Finally the scatter source is found by substituting equation (25) into the source of equation (19) resulting in

$$q_{g,n}^s(\vec{r}) \approx \sum_{g'=1}^G \sum_{n'=1}^N w_{n'} \sum_{l=0}^L \sum_{m=-l}^l Y_{lm}^*(\hat{\Omega}_n) Y_{lm}(\hat{\Omega}_{n'}) \sigma_{lgg'} \psi_{g',n'}(\vec{r}). \quad (26)$$

One crucial aspect in solving these equations is that the scattering coefficients $\sigma_{lg'g}$ are known calculated *a priori* using codes such as AMPX³ or NJOY⁴. Still, once they are known, for the small cost of calculating the spherical harmonics, the memory requirement is significantly reduced.

In a standard transport code, the source is typically found by first calculating the moments of the total group flux

$$\phi_{lg'}^m(\vec{r}) \approx \sum_{n'=1}^N w_{n'} Y_{lm}(\hat{\Omega}_{n'}) \psi_{g',n'}(\vec{r}). \quad (27)$$

Once moments of the group flux are found, there is no longer a need for the $\psi_{g',n'}$ reducing memory requirements further. The source is found from

$$q_{g,n}^s(\vec{r}) \approx \sum_{l=0}^L \sum_{m=-l}^l Y_{lm}^*(\hat{\Omega}_n) \sum_{g'=1}^G \sigma_{lgg'} \phi_{lg'}^l(\vec{r}). \quad (28)$$

Of course, the spherical harmonic approximation is just that, an approximation. It is an attempt to model the physics with a polynomial. In many cases such an approximation may be sufficient. Unfortunately, the method becomes woefully inadequate in a number of ways particularly for anisotropic scattering.

Anisotropic scattering becomes significant when considering

- a. scattering of high energy particles from nuclei of all mass numbers,
- b. scattering of any energy particle from light nuclei, and
- c. when the group structure is so fine that the allowed angular region of scatter is also small⁵.

Such scattering can be highly peaked and, because of the group structure used, be positive for only a small portion of the scattering range and zero over the rest of the angular domain.

Because $\sigma_{g'g}^s(\hat{\Omega}_{n'} \rightarrow \hat{\Omega}_n) = \sigma_{g'g}^s(\hat{\Omega}_{n'} \cdot \hat{\Omega}_n)$, we define $\mu_L \equiv \hat{\Omega}_{n'} \cdot \hat{\Omega}_n$, the cosine of the scattering angle in the laboratory frame. It is often convenient to examine the behavior of the cross-section in terms of $\sigma_{g'g}^s(\mu_L)$. We use this form of the scattering cross section to demonstrate the problems Legendre polynomials have approximating the type of anisotropic behavior described above. Figure 2 shows an exact group-to-group scatter, $\sigma_{g'g}^s(\mu_L)$, for hydrogen. Also shown in the figure are three Legendre approximations of the cross section using the Legendre expansion of equation (22) for $L = 1, 3$, and 7.

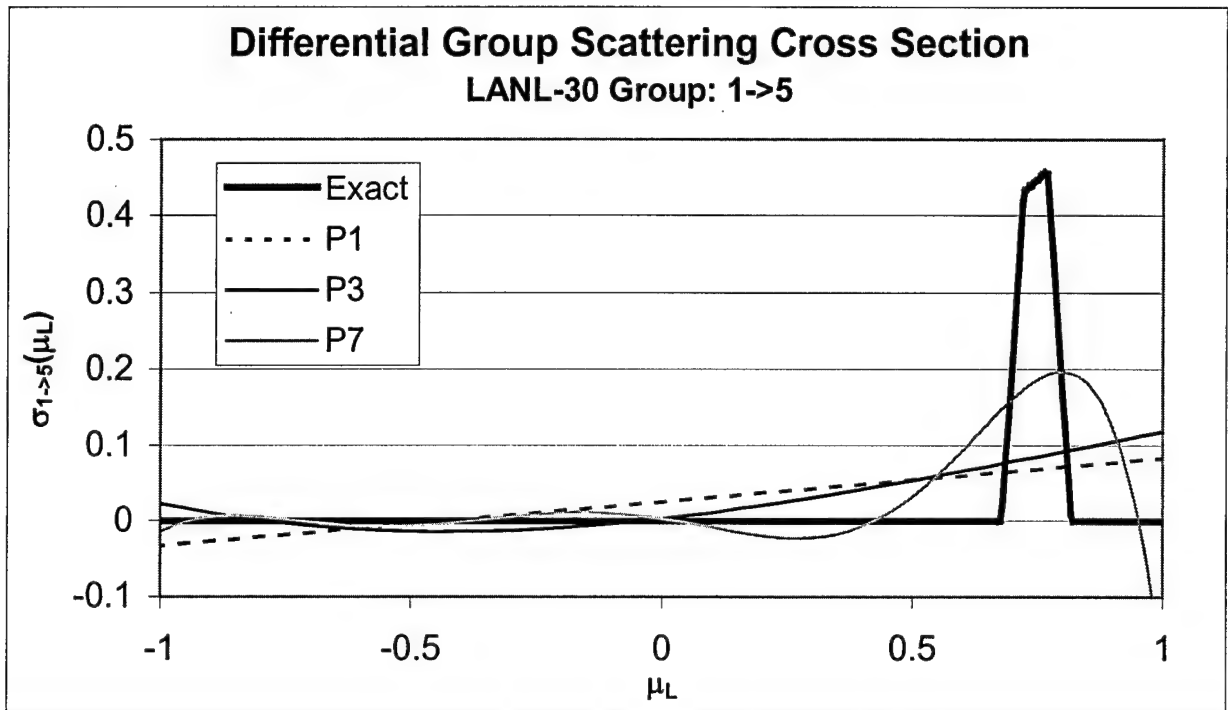


Figure 2. Group 1→5 scatter for hydrogen, ^1H , in the lab frame.

The Legendre expansion of such a scatter fails in two ways. First, because the polynomial is unable to model such a step function, it spreads the distribution of scatters to other angles, causing an angular diffusion of the scatters that is a computational artifact. Second, the expansion may become negative in some angular regions. This may lead to the calculation of negative sources, which are non-physical. Worse, the calculation of such sources can cause certain spatial quadrature techniques used in transport codes to fail^{6,7}. Particularly vulnerable are exponential methods that guarantee non-negative flux solutions, but require non-negative sources⁸. In the case when negative sources appear in codes that don't care or when such sources are *fixed* by setting them to zero significant convergence problems

may arise⁹. Such difficulties have led researchers to attempt alternative approaches that would eliminate negative cross-section values.

4. Attempts to Fix Negativity

A number of attempts have been made to eliminate negative sources. Each of the techniques described here use the full scattering matrices to calculate the scattering source term (possible now with today's computational capabilities). This chapter outlines three techniques, each with its shortcomings, and introduces the method we propose.

Exact Ordinate-to-Ordinate Scatter

Odom was one of the first to try to eliminate the problem of negative sources in anisotropic scattering¹⁰. To calculate the source from equation (20) directly, he calculated the ordinate-to-ordinate ($\hat{\Omega}_{n'} \rightarrow \hat{\Omega}_n$) scattering cross section from the physics, but only for elastic and level inelastic scattering. With this approach, he was able to devise a number of different cases to calculate the scattering cross section dependent on the angle and energies involved. In particular, the group-to-group scattering cross section

$$\sigma_{g'g}^s(\hat{\Omega}_{n'} \cdot \hat{\Omega}_n) = \frac{\int_g dE \int_{g'} dE' \sigma^s(\vec{r}, E' \rightarrow E, \hat{\Omega}_{n'} \cdot \hat{\Omega}_n) W(E')}{\int_{g'} dE' W(E')} \quad (29)$$

was reduced to the calculation of a 1-D integral⁵.

The integration must be performed for each ordinate-to-ordinate combination (dependent on the quadrature used), and for each group-to-group combination (dependent on the group structure used). For some scattering

combinations, dependent on the energy-angle combination, the integration must be performed more than once. If level inelastic scattering is to be calculated, the integration must be performed again for each elastic and level inelastic transfer. In oxygen, for example there are 38 inelastic levels from the evaluated nuclear data files, ENDF/B-VI. The results are then summed to provide the total transfer cross-section. Fortunately the integration is only one dimensional, but the number of cases that must be considered make the method computationally burdensome, although no mention is made of the time required to compute the integration even from more recent authors⁵. While elastic and level-inelastic scatter can be treated with a complicated case structure, other types of scatter (e.g., $(n, 2n)$) become too difficult to put the 1-D integral equation of Odom in a readily integrable form and are instead treated as isotropic even when they are not.

While the technique requires a complicated number of integration cases to account for variations in group structure, the process guarantees a non-negative scattering cross-section. In addition to the complexity of the integration, the method suffers from one major drawback. As Brockman⁵ notes, for elements with a highly anisotropic angular distribution or for light elements along with a fine energy group structure, the group-to-group transfer cross section is confined to a small angular range (Figure 3). If the angular quadrature used is too sparse (lack of *angular support*), particles traveling in one direction may never scatter into another.

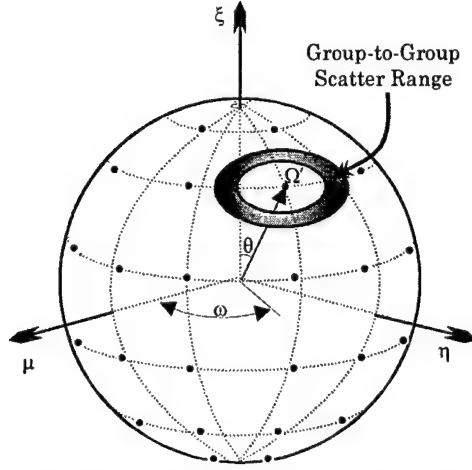


Figure 3. Group-to-group Scattering Geometry⁵.

Angular Support

Lack of angular support is shown by examining the lab frame scattering cosine

$$\mu_L = S(E, E') \equiv \frac{1}{2} \left[(A+1) \sqrt{\frac{E}{E'}} - (A-1) \sqrt{\frac{E'}{E}} - \frac{QA}{\sqrt{EE'}} \right]. \quad (30)$$

For elastic scattering, $Q = 0$, and equation (30) can be re-written as

$$\mu_L = \frac{1}{2} \left[(A+1) \sqrt{\frac{E' - \Delta E}{E'}} - (A-1) \sqrt{\frac{E'}{E' - \Delta E}} \right], \quad (31)$$

where ΔE is the energy lost by the neutron in the collision. Expanding equation (31) in a power series about $\Delta E = 0$, the scattering angle for small energy loss is

$$\mu_L = 1 - \frac{A}{2} \frac{\Delta E}{E'} + O(\Delta E^2). \quad (32)$$

Because, $\mu_L = \cos(\theta_L) \approx 1 - \frac{\theta_L^2}{2} + O(\theta_L^4)$ for small θ_L , equation (32) can be written in terms of the scattering angle

$$\theta_L \approx \sqrt{\frac{2A}{E'} \Delta E}. \quad (33)$$

Using fine energy group structures the within group and next group scattering angles will be small. For within group scatter, the greatest scattering angle (smallest μ_L) occurs when a neutron scatters from the top of the group to the bottom of the group or $\Delta E = \Delta E_g + \alpha_1$ where α_1 is an arbitrarily small number greater than zero.

For ordinate-to-ordinate methods, the θ_L 's corresponding to the various combinations of n and n' are fixed based on the selected angular quadrature. To guarantee within group scatter, two directional ordinates must be close enough so that

$$\theta_L(\hat{\Omega}_{n'} \rightarrow \hat{\Omega}_n) \leq \sqrt{\frac{2A}{E'} (\Delta E_g + \alpha_1)}. \quad (34)$$

If θ_{\min} is the smallest angle of all the possible ordinate-to-ordinate scatters, then as the group structure becomes fine enough, $\Delta E_g \rightarrow \alpha_2$ (where again α_2 is an arbitrarily small number greater than zero), we can find an α_2 such that

$$\theta_{\min} > \sqrt{\frac{2A}{E'} (\alpha_1 + \alpha_2)}, \quad (35)$$

and within group scatter is not possible for any of the ordinate-to-ordinate scatter combinations.

The same analysis holds for downscattering to the next lowest group. Here, the greatest scattering angle (smallest μ_L) occurs when a neutron scatters from the top of the incident group to the bottom of the scattered group or $\Delta E = \Delta E_g + \Delta E_{g+1} + \alpha_1$. This scattering is not as restrictive on the angular quadrature as within group scattering. Because $\Delta E_g \rightarrow \alpha_2$ and $\Delta E_{g+1} \rightarrow \alpha_3$ results in

$$\theta_{\min} > \sqrt{\frac{2A}{E'}(\alpha_1 + \alpha_2 + \alpha_3)}. \quad (36)$$

Still, it will always be possible to find a fine enough group structure such that downscatter to the next lower group is not supported by the angular quadrature.

Does such a failure in angular support occur with typical angular quadratures and standard group structures? The answer is yes. As is shown in detail in chapter 9, for example, the nearest scattering cosine in an S_8 level symmetric angular quadrature is $\mu_L = 0.922$ ($\theta_L \approx 23^\circ$). If Oak Ridge National Laboratory's 175 group VITAMIN-J group structure is used (see appendix E), 109 of the 175 groups are unable to downscatter to the next lower group using an ordinate-to-ordinate approach. Lack of such angular support is particularly troublesome for within group and next group scatter.

Mikols provided a means of analyzing such behavior. He showed where quadrature and group structure combinations fail for neutral particle scattering¹¹. Using the same type of analysis, it is also possible to show that some group-to-group scatters get skipped even though the physics says they shouldn't.

The difficulties encountered in calculating the ordinate-to-ordinate cross-sections and the failure of the method for sparse angular quadratures have made it an unacceptable choice in the transport community.

Non-negative Functional Scattering Cross Section Representation

Another method to solve the source negativity problem is to represent the scattering cross-section with a strictly non-negative function. One such method was proposed by Dahl⁶.

Dahl also attempted to calculate the group-to-group scattering cross section as a function of angle, and, like Odom, Dahl's method requires storage of the angular fluxes during the transport calculation. Dahl replaces the conventional finite Legendre scattering cross section representation with an exponential form

$$\sigma_{g'g}^s(\hat{\Omega}' \cdot \hat{\Omega}) = \exp\left(\sum_{l=0}^L \lambda_{g'g}^l P_l(\hat{\Omega}' \cdot \hat{\Omega})\right). \quad (37)$$

To determine each $\lambda_{g',g}^l$, the constraint that the original cross section moments, $\sigma_{g',g}^l$, be preserved is imposed. This results in $L+1$ coupled non-linear equations which are solved for the $\lambda_{g',g}^l$'s:

$$\sigma_{g',g}^l - \int_{-1}^1 P_l(\mu_L) \exp\left(\sum_{l'=0}^L \lambda_{g',g}^{l'} P_{l'}(\mu_L)\right) d\mu_L = 0, \quad l = 0, 1, \dots, L. \quad (38)$$

Unfortunately, Dahl found it computationally impossible to match all the moments of the Legendre polynomial representation. He presented an example in which the zeroth through fifth moments were matched, and showed that the sixth through fifteenth moments of the exponential approximation were quite close to the corresponding moments of the actual cross section. While this is promising, he has not presented a reliable method for finding the values of the coefficients, $\lambda_{g',g}^l$. Dahl warns that the accuracy of the method is sensitive to the number of equations the non-linear solver must evaluate. If too many input moments are used, the exponential expansion calculated using the code, XREP¹², no longer preserves the original moments. Thus, there is an inherent limit to the accuracy of the method. Further, while the method is strictly positive, it should only be non-negative. Even where there are scattering transfers which are strictly not allowed, the exponential representation has a non-zero value. Finally, even if this method could match the scattering cross section exactly, the same ordinate-to-ordinate scattering limitations described above (lack of the angular support) apply.

Use of Piecewise Constant Functions

The methods described so far treat the scatter as being only from one directional ordinate to another. Namely $\sigma_{g'g}^s(\hat{\Omega}_{n'} \cdot \hat{\Omega}_n)$ corresponds to the scatter from $\hat{\Omega}_{n'} \rightarrow \hat{\Omega}_n$ on the unit sphere. Borsari suggests an alternate approach¹³. He suggests thinking of the transfer as being the average scatter from one patch of solid angle on the sphere to another.

Instead of the directional ordinates representing a single direction in space, consider partitioning the possible angular directions of a sphere into (what we call) facets. With each facet representing a separate and distinct patch of solid angle or area on the sphere. Mathematically, a facet on the unit sphere, \mathcal{U} , corresponds to a portion, $\Delta\Omega$, of the sphere's total solid angle. The union of these non-intersecting patches, or facets, cover the sphere, so that

$$\sum_{n=1}^N \Delta\Omega_n = \int_{\mathcal{U}} d\Omega = 1. \quad (39)$$

The scattering from ordinate-to-ordinate ($\hat{\Omega}_{n'} \rightarrow \hat{\Omega}_n$) is now represented as an average of the scatter from facet to facet ($\Delta\hat{\Omega}_{n'} \rightarrow \Delta\hat{\Omega}_n$)¹³. And the *average* scattering cross section is defined as

$$\bar{\sigma}_{g'g}^{n'n} \equiv \int_{n'} \frac{d\Omega'}{\Delta\Omega_{n'}} \int_n \frac{d\Omega}{\Delta\Omega_n} \sigma_{g'g}^s(\hat{\Omega}' \cdot \hat{\Omega}). \quad (40)$$

To accomplish the integration, Borsari assumed a piecewise continuous function (p.c.f.) of $\sigma_{g'g}(\mu_L)$, so that $\sigma_{g'g}(\mu_L)$ is approximated as stepwise bands on the sphere (Figure 4).

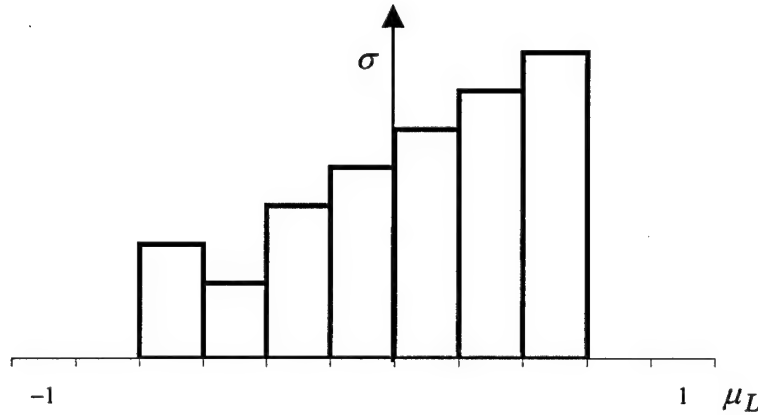


Figure 4. Borsari scattering cross-section p.c.f.

Borsari spent much of his effort looking at the best way to create the cross section values at the given $\sigma_{g'g}(\mu_L)$ mesh points (referred to as the gamma grid). He examined gamma grids that depended only on the facet quadrature, and gamma grids that depended on the behavior of $\sigma_{g'g}(\mu_L)$. In either case, the accuracy of the method depended on the resolution of the gamma grid. To calculate the average cross section, grid values were interpolated. A Cartesian product angular quadrature simplified finding the intersections of the gamma grid with facet boundaries. This, in turn, made calculating the integral of equation (40) simpler, but restricts Borsari's method to Cartesian product quadratures.

The implication in calculating the scattering source can be found by returning to equation (16)

$$q_g^s(\vec{r}, \hat{\Omega}) = \sum_{g'=1}^G \int d\Omega' \int_g dE \int_{g'} dE' \sigma^s(E' \rightarrow E, \hat{\Omega}' \cdot \hat{\Omega}) \tilde{W}_g(E') \psi(\vec{r}, \hat{\Omega}'), \quad (41)$$

where the source is now approximated as

$$q_{g,n}^s(\vec{r}) \approx \sum_{g'=1}^G \sum_{n'=1}^N \Delta\Omega_{n'} \times \int_{n'} \frac{d\Omega'}{\Delta\Omega_{n'}} \int_n \frac{d\Omega}{\Delta\Omega_n} \int_g dE \int_{g'} dE' \sigma^s(E' \rightarrow E, \hat{\Omega}' \cdot \hat{\Omega}) \tilde{W}_g(E') \psi_{g',n'}(\vec{r}). \quad (42)$$

The scattering source term takes on the exact same form as equation (19),

$$q_{g,n}^s(\vec{r}) = \sum_{g'=1}^G \sum_{n'=1}^N w_{n'} \sigma_{g'g}^s(\hat{\Omega}_{n'} \cdot \hat{\Omega}_n) \psi_{g',n'}(\vec{r}), \quad (43)$$

with

$$w_{n'} = \Delta\Omega_{n'}, \quad (44)$$

$$\sigma_{g'g}^s(\hat{\Omega}_{n'} \cdot \hat{\Omega}_n) = \bar{\sigma}_{g'g}^{n'n} \equiv \int_{n'} \frac{d\hat{\Omega}'}{\Delta\Omega_{n'}} \int_n \frac{d\hat{\Omega}}{\Delta\Omega_n} \int_g dE \int_{g'} dE' \sigma^s(E' \rightarrow E, \hat{\Omega}' \cdot \hat{\Omega}) \tilde{W}_g(E'), \quad (45)$$

and the angular flux unaltered.

Not discussed by Borsari, but mentioned here is the immediate advantage of this technique over ordinate-to-ordinate methods in that it guarantees angular support.

In averaging the scatter over the facets some of the scatters will take place near facet boundaries. As $\hat{\Omega}_{n'}$ and $\hat{\Omega}_n$ approach each other on a facet

boundary, $\theta_L \rightarrow 0$. Thus, from equation (34), for any fixed group structure there will always be some scatter such that

$$\theta_L(\hat{\Omega}' \rightarrow \hat{\Omega}) \leq \sqrt{\frac{2A}{E'}(\Delta E_g + \alpha 1)}, \quad \hat{\Omega}' \in \hat{\Omega}_{n'}, \hat{\Omega} \in \hat{\Omega}_n. \quad (46)$$

where $\alpha 1$ is an arbitrarily small number greater than zero. Such behavior is independent of the facet dimension (or quadrature size) Because the scatter occurs at the facet boundary. Because the separation between neighboring facets is zero, there is always the possibility of scattering from one facet to the other no matter how small the loss of energy in the collision. And because the entire sphere is tiled with facets, every group-to-group scatter that can occur (based on the scattering physics) will occur.

The Borsari method is essentially an ordinate-to-ordinate paradigm that required interpolation schemes over his μ_L values when scatter spanned multiple squares on his Cartesian grid. The intricate relations between the way the source facet was partitioned for integration and the way the grid of μ_L values is selected affects accuracy and non-negativity. Solving the integration of equation (42), Borsari did not discuss how $\sigma_{g'g}^s(\vec{r}, \mu_L)$ is found at the requisite gamma grid points. Further, using such a grid required that the sphere be tiled with a Cartesian facet quadrature. This made calculation of the integrals simpler, but the method can not modified to use more symmetric quadratures.

The use of piecewise continuous functions (or facets) also required the rebalance of the cross section matrices to conserve the first angular moments of the scatter (thus preserving the currents). Borsari's approach requires that the rebalance be performed during execution of the transport code, thus adding another level of complexity to the method. Further, his rebalance technique may destroy source non-negativity¹³.

While Borsari's idea of the facet representation holds promise, his implementation is complicated, dependent on the appropriateness of the facet gridding for the type of scatter, and wed to a Cartesian angular quadrature type. As a consequence, most of the paper is more mathematical rather than practical. No effort was made to actually calculate $\bar{\sigma}_{g'g}^{n'n}$ for real materials.

Present methods fail to adequately address the problems of anisotropic scattering in neutral particle transport. There is a need within the transport community for the creation of a new approach that is simple to calculate and implement in transport codes. We propose a completely novel approach -- an approach that incorporates the sampling of the physics used by MCNP at its heart, and takes advantage of the benefits a facet method has over ordinate-to-ordinate techniques. Our goal, as always, is to *return to the physics* and model the transfer matrix as accurately as possible without resorting to expansions and fix-ups.

The Monte Carlo Facet Method

Return to the physics is the overarching philosophy of this approach.

When the results of discrete ordinates codes are presented, they are almost universally benchmarked, validated and otherwise compared to similar problems run using the Monte Carlo transport code MCNP¹⁴. MCNP stochastically models the transport process as continuous in space, energy and angle. Experimentally measured cross sections are combined with predictions from nuclear model calculations. The results of this combination are incorporated into sets of data such as the Evaluated Nuclear Data File (ENDF) libraries¹⁵. MCNP samples this data directly from continuous energy cross section information obtained from the ENDF data. The continuous energy cross section library used by MCNP is known as an ACE library. Of course, discrete ordinates methods are discrete in space, energy and angle. Our goal is to model the energy-angle relationship as closely to the continuous model (much like MCNP) as is possible. To this end, our technique samples directly from the ACE tables in much the same way as MCNP.

Following Borsari, we define the average group-to-group scattering cross section as

$$\bar{\sigma}_{g'g}^{n'n} = \frac{\int_{n'} \frac{d\Omega'}{\Delta\Omega_{n'}} \int_n \frac{d\Omega}{\Delta\Omega_n} \int_{g'} dE' \int_g dE \sigma^s(E' \rightarrow E, \hat{\Omega}' \cdot \hat{\Omega}) W(E')}{\int_{g'} dE' W(E')}, \quad (47)$$

where, as Borsari did , we consider the average scatter of particles from one facet, $\Delta\Omega'$, to another, $\Delta\Omega$ as shown in Figure 5.

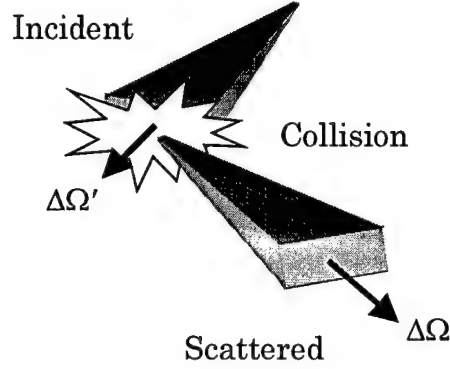


Figure 5. Scattering from $\Delta\Omega' \rightarrow \Delta\Omega$.

Substituting equation (2),

$$\bar{\sigma}_{g'g}^{n'n} = \frac{\int_{n'} \frac{d\Omega'}{\Delta\Omega_{n'}} \int_n \frac{d\Omega}{\Delta\Omega_n} \int_{g'} dE' \int_g dE \sigma^s(E') f(E' \rightarrow E, \hat{\Omega}_{n'} \cdot \hat{\Omega}_n) W(E')}{\int_{g'} dE' W(E')}, \quad (48)$$

Unlike Borsari, we chose to evaluate the integral in equation (47) by Monte Carlo integration. Before that can be accomplished, equation (48) needs to be put into a form that is readily evaluated using MC techniques.

For simplicity the numerator and denominator of equation (48) are examined separately and re-written as

$$\bar{\sigma}_{g'g,n'n}^{Num} = \frac{1}{\Delta\Omega_{n'} \Delta\Omega_n} \int_{g'} dE' \int_{n'} d\Omega' \sigma^s(E') W(E') \int_n d\Omega \int_g dE f(E' \rightarrow E, \hat{\Omega}_{n'} \cdot \hat{\Omega}_n), \quad (49)$$

and

$$\overline{\sigma}_{g'g,n'n}^{Den} = \int_{g'} dE' W(E') . \quad (50)$$

Recall that the integration over all scattered energies and angles of $f(E' \rightarrow E, \hat{\Omega}_n \cdot \hat{\Omega}_n)$ equals the expectation value of the number of neutrons that emerge from the collision given an incident energy, E' . The same integration over the scattered group and facet, namely

$$\int_n d\Omega \int_g dE f(E' \rightarrow E, \hat{\Omega}_n \cdot \hat{\Omega}_n)$$

is the expectation value of the number of neutrons that emerge from a collision and scatter into energy group g and facet n .

In the MC facet method this is sampled in a specific way. For a given material, the type of scatter is determined. This scattering physics might be elastic, inelastic, thermal, etc. The material dependent sampling of the physics will be represented with the variable, τ . This may involve sampling the scattering angle, μ_{cm} , to find μ_L and E , or it may involve sampling E to then find μ_L . In either case, based on the physics model and the incident energy the lab frame scattering angle, μ_L , and scattered energy, E , are determined. The lab frame azimuthal scattering angle, ω_L , is sampled uniformly in 2π . The scattered direction, $\hat{\Omega}$, is constructed from $\hat{\Omega}'$, μ_L , and ω_L . Finally, the appropriate scattered group and facet are determined such that $E \in \Delta E_g$, and $\hat{\Omega} \in \Delta \Omega_n$.

We now define the distributions $f_\tau(\tau; E', \hat{\Omega}')$ and $f_{\omega_L}(\omega_L)$ such that

$$\begin{aligned}
& \int_{-\infty}^{\infty} d\tau \int_{-1}^1 \frac{d\mu_L}{2} \int_0^{2\pi} \frac{d\omega_L}{2\pi} \int_{\mathcal{U}} d\Omega \int_0^{\infty} dE f_\tau(\tau; E', \hat{\Omega}') f_{\omega_L}(\omega_L) \\
& \quad \times \delta(\mu_L - \tilde{\mu}_L) \delta^2(E - \tilde{E}) \delta(\hat{\Omega} - \tilde{\Omega}) \chi_g^E(E) \chi_n^{\hat{\Omega}}(\hat{\Omega}) \\
& \equiv \int_n d\Omega \int_g dE f(E' \rightarrow E, \hat{\Omega}_n, \hat{\Omega}_n)
\end{aligned} \tag{51}$$

where in general

$$\int_0^{\infty} dE g(E) \delta(E - \tilde{E}) = g(\tilde{E}), \tag{52}$$

$$\int_{\mathcal{U}} d\Omega g(\hat{\Omega}) \delta^2(\hat{\Omega} - \tilde{\Omega}) = g(\tilde{\Omega}), \tag{53}$$

$$\int_{-1}^1 d\mu_L g(\mu_L) \delta(\mu_L - \tilde{\mu}_L) = g(\tilde{\mu}_L), \tag{54}$$

and \tilde{E} , $\tilde{\Omega}$, and $\tilde{\mu}_L$, are constructed by

$$\tilde{E} = \tilde{E}(\tau, E'), \tag{55}$$

$$\tilde{\Omega} = \tilde{\Omega}(\hat{\Omega}', \mu_L, \omega_L), \tag{56}$$

and $\tilde{\mu}_L = \tilde{\mu}_L(\tau, E').$ (57)

The characteristic functions, $\chi_g^E(E)$, and $\chi_n^{\hat{\Omega}}(\hat{\Omega})$, are found from

$$\chi_g^E(E) = \begin{cases} 1 & E \in \Delta E_g, \\ 0 & \text{else,} \end{cases} \tag{58}$$

and

$$\chi_n^{\hat{\Omega}}(\hat{\Omega}) = \begin{cases} 1 & \hat{\Omega} \in \Delta \Omega_n, \\ 0 & \text{else.} \end{cases} \tag{59}$$

Substituting equation (51) into (49) gives

$$\begin{aligned} \bar{\sigma}_{g'g,n'n}^{Num} = & \frac{1}{\Delta\Omega_{n'}\Delta\Omega_n} \int_{g'} dE' \int_{n'} d\Omega' \int_{-\infty}^{\infty} d\tau \int_0^{2\pi} d\omega_L \sigma^s(E') W(E') \chi_g^E(\tilde{E}) \chi_n^{\hat{\Omega}}(\tilde{\Omega}) \\ & \times f_{\tau}(\tau; E', \hat{\Omega}') f_{\omega_L}(\omega_L). \end{aligned} \quad (60)$$

Applying Monte Carlo sample mean integration to approximate the integral above (Appendix A), the integrals in τ and ω_L are sampled using the distributions shown. The integration over g' is found by sampling E' uniformly over $\Delta E_{g'}$ (represented by the distribution $f_{g'}(E')$). Similarly the integral over n' is found by sampling $\hat{\Omega}'$ uniformly over $\Delta\Omega_{n'}$, or $f_{n'}(\hat{\Omega}')$.

Showing the sampling distributions explicitly in (60) we have

$$\begin{aligned} \bar{\sigma}_{g'g,n'n}^{Num} = & \frac{\Delta E_{g'}}{\Delta\Omega_n} \int_{g'} dE' \int_{n'} d\Omega' \int_{-\infty}^{\infty} d\tau \int_0^{2\pi} d\omega_L \sigma^s(E') W(E') \chi_g^E(\tilde{E}) \chi_n^{\hat{\Omega}}(\tilde{\Omega}) \\ & \times f_{g'}(E') f_{n'}(\hat{\Omega}') f_{\tau}(\tau; E', \hat{\Omega}') f_{\omega_L}(\omega_L), \end{aligned} \quad (61)$$

and for the denominator

$$\bar{\sigma}_{g'g,n'n}^{Den} = \Delta E_{g'} \int_{g'} dE' W(E') f_{g'}(E'). \quad (62)$$

The resulting Monte Carlo approximation is

$$\bar{\sigma}_{g'g}^{n'n} \approx \frac{\frac{1}{\Delta\Omega_n} \frac{1}{M} \sum_{i=1}^M \left[\sigma^s(E'_i) W(E'_i) \chi_g^E(\tilde{E}_i) \chi_n^{\hat{\Omega}}(\tilde{\Omega}_i) \right]}{\frac{1}{M_{g,n}} \sum_{i=1}^M W(E'_i) \chi_g^E(\tilde{E}_i) \chi_n^{\hat{\Omega}}(\tilde{\Omega}_i)}, \quad (63)$$

where M is the total number of incident particles, $M_{g,n} = \sum_{i=1}^M \chi_g^E(\tilde{E}_i) \chi_n^{\hat{\Omega}}(\tilde{\Omega}_i)$

the number of scatters to group g and facet n , and the sampling of incident

energy, E'_i , is done coherently for the two summations to guarantee appropriate normalization over the selected scatters. The sampling is performed as follows:

1. E'_i is sampled uniformly in $\Delta E_{g'}$,
2. $\hat{\Omega}'_i$ is sampled uniformly in $\Delta \Omega_{n'}$,
3. \tilde{E}_i and $\tilde{\Omega}_i$ are found consistently from the scattering physics by sampling $f_\tau(\tau; E', \hat{\Omega}')$;

Typically (for elastic and level inelastic scatter) the sampling variable τ represents μ_{cm} which is sampled from a distribution table based on the selected physics model and E'_i . From μ_{cm}

μ_L is calculated using scattering kinematics, and

\tilde{E}_i is found using scattering kinematics, then

ω_L is sampled from $f_{\omega_L}(\omega_L)$ uniformly in $[0, 2\pi)$,

and

$\tilde{\Omega}_i$ is constructed geometrically from $\hat{\Omega}'_i$, $\mu_L = \hat{\Omega}'_i \cdot \hat{\Omega}_i$, and ω_L .

4. The scattered group and facet are rejected unless $\tilde{E}_i \in \Delta E_g$, and $\tilde{\Omega}_i \in \Delta \Omega_n$.

Implementation of the MC facet method is simple and straight forward.

The scattering data is taken directly from the continuous ACE tables

constructed directly from ENDF data. Any energy weighting function can be used. Algorithm 1, below, outlines the essential steps of the MC facet method. The remaining theory sections explain how each step is performed. The approach is completely general. To demonstrate it, we used a particularly convenient angular quadrature and implemented only a few of the MCNP scattering laws.

Algorithm 1. Basic Algorithm for the MC Facet Method

Set desired facet quadrature, total facets = N .

Set desired group structure, total groups = G .

Do $g'=1..G$

Do $n'=1..N$

TallyNum = 0 Array Dimension ($N \times G$)

TallyDen = 0 Array Dimension ($N \times G$)

TallyErr = 0 Array Dimension ($N \times G$)

Do $i = 1..M$ (until converged or some max sample size reached)

Draw E' uniformly in $\Delta E_{g'}$.

Draw $\hat{\Omega}'$ uniformly in $\Delta\Omega_{n'}$.

Draw E and μ_L consistently from scattering physics.

--(Incorporates MCNP/ACE models of ENDF-B data)

Draw ω_L uniformly in $[0, 2\pi)$.

Construct $\hat{\Omega}$ geometrically from $\hat{\Omega}'$, μ_L , and ω_L .

Find g such that $E \in \Delta E_g$.

Find n such that $\hat{\Omega} \in \Delta\Omega_n$.

TallyNum(n, g) = TallyNum(n, g) + $\sigma^s(E')W(E')$

TallyDen(n, g) = TallyDen(n, g) + $W(E')$

TallyErr(n, g) = TallyErr(n, g) + $[\sigma^s(E')W(E')]^2$

End Do

$$\bar{\sigma}_{g'g}^{n'n} \approx \frac{M_{g,n}}{M} \Delta\Omega_{n'} [\text{TallyNum}(n, g) / \text{TallyDen}(n, g)]$$

$$\text{Err}_{g'g}^{n'n} \approx 1.96 \Delta\Omega_{n'} \frac{\sqrt{\frac{1}{M} \left\{ \left[\frac{1}{M} \text{TallyErr}(n, g) \right] - \left[\frac{1}{M} \text{TallyNum}(n, g) \right]^2 \right\}}}{\left[\frac{1}{M_{g,n}} \text{TallyDen}(n, g) \right]}$$

Save $\bar{\sigma}_{g'g}^{n'n}$ and $\text{Err}_{g'g}^{n'n}$ to file for $n = 1..N$, and $g = 1..G$.

End Do (Incident Facets)

End Do (Incident Groups)

Advantages of the MC Facet Method

The Monte Carlo facet method has a number of advantages over previously discussed methods:

Guaranteed Non-Negative. Equation (48) is approximated using a Monte Carlo method, where the values are accumulations of non-negative values. The scattering matrix is zero where scattering is not allowed and positive for values where scattering is allowed.

Guaranteed Within Group Scatter. Adjacent facets will always scatter into each other no matter how small the energy loss (equation (46)). This means that particles can't be trapped in a group (as in the ordinate-to-ordinate method) because of the group structure used no matter how sparse the angular quadrature. Similarly, down scatter groups can't be skipped as an artifact of the angular quadrature. This will be demonstrated in chapter 9.

Adjustable accuracy. Unlike the method proposed by Dahl, which fails if one attempts to match too many moments, the user can achieve the desired cross-section accuracy by simply increasing the number of trials in the calculation.

Arbitrary Quadratures. Because particles are tracked directly from one facet to another, any shaped facet or quadrature structure may be used. This is distinct from Borsari's analysis which applied only to Cartesian type grids. Hence, the quadrature can be triangular, icosahedral, etc.

Incorporates ENDF Scattering Laws. A number of techniques (e.g., Odom) consider only elastic and level inelastic scattering because the integration of the scattering kernel is simplified. Other methods, such as Borsari, make no attempt to address the type of scattering involved. In fact, such scattering can be quite complicated. There are a number of different ways to describe the types of scattering involved. The Monte Carlo facet method is able to take advantage of all the ENDF scattering laws in exactly the same way that MCNP does. Any neutral particle scattering law (neutrons or photons) can follow the exact same formalism developed here. All the scattering possibilities are accounted for in one integration of the average cross section (unlike Odom's, for example, which requires a separate integral calculation for each type of scatter). Taken together, these advantages suggest a significant breakthrough in the attempt to account for anisotropic scatter in neutral particle transport.

5. Implications of Facet Transfers on Neutral Particle Transport

This chapter outlines some mathematical cautions concerning application of the average scattering technique to the transport code. It ends by demonstrating how this method is used with TETRAN, which is the neutral particle transport code developed at AFIT⁷.

Effect of Scatter Averaging

Recall that in discrete ordinates theory the scattered angular flux is approximated by

$$q_{g,n}^s(\vec{r}) = \sum_{g'=1}^G \sum_{n'=1}^N w_{n'} \int_g dE \int_{g'} dE' \sigma^s(\vec{r}, E' \rightarrow E, \hat{\Omega}_{n'} \cdot \hat{\Omega}_n) \tilde{W}_{g'}(E') \psi_{g',n'}(\vec{r}) \quad (64)$$

where $\psi_{g',n'}$ is the total group angular flux evaluated at a specific directional ordinate. Here, evaluation of the group-to-group scattering source represents the explicit transfer of particles from all incident groups to one scattered group and all incident directions to a specific directional ordinate.

Use of the average scattering cross section, $\bar{\sigma}_{g'g}^{n'n}$, puts a small but important conceptual twist on this transfer. Here the scattering from all incident directions to a specific scattered directional ordinate is approximated as the average scatter of all incident directions to a facet surrounding (in an appropriate way) the scattered directional ordinate.

One advantage of such a method, previously discussed, was that this guarantees that all group-to-group scatters will have somewhere to scatter—regardless of the scattering anisotropy. The disadvantage of such a method is that it can contribute to angular dispersion of the scatter and that it fails to conserve the first angular moment of the scatter, which is important for diffusion problems. We examine the dispersion effects in subsequent chapters and discover that their impact on the transport results is minimal. In the following chapter we address how to redistribute the scattering matrix in order to conserve the first angular moment of the scatter.

Standard MC Facet Method Implementation

To speed the calculation of the scattering source

$$q_{g,n}^s = \sum_{g'=1}^G \sum_{n'=1}^N w_{n'} \bar{\sigma}_{g'g}^{n'n} \psi_{g'n'} \quad (65)$$

we define the group-to-group, facet-to-facet transfer matrix, T , as

$$T_{g'g}^{n'n} = w_{n'} \bar{\sigma}_{g'g}^{n'n} = \Delta\Omega_{n'} \bar{\sigma}_{g'g}^{n'n}. \quad (66)$$

Although T is an array of rank 4, we think of it as a matrix because only the rank two array section $T_{n'n}$, for one combination of groups, g' and g , need be loaded into memory during the transport code run at any given time. This allows the transport code to perform a direct matrix multiply using an optimized intrinsic routine in Fortran-90. The scattering source becomes

$$q_{g,n}^s = \sum_{g'=1}^G \sum_{n'=1}^N T_{g'g}^{n'n} \psi_{g',n'}. \quad (67)$$

The transport code, TETRAN, used for this research only allows for downscatter, so equation (67) is

$$q_{g,n}^s = \sum_{g'=1}^g \sum_{n'=1}^N T_{g'g}^{n'n} \psi_{g',n'}. \quad (68)$$

Using the equations for $w_{n'}$ and $\bar{\sigma}_{g'g}^{n'n}$ from the previous chapter, and because $\Delta\Omega_{n'} = \Delta\Omega_n$ for the Cartesian quadrature we've selected, the T-matrix is

$$T_{g'g}^{n'n} \approx \frac{M_{g,n}}{M} \frac{\sum_{i=1}^M \left[\sigma^s(E_i') W(E_i') \chi_g^E(\tilde{E}_i) \chi_n^{\hat{\Omega}}(\tilde{\Omega}_i) \right]}{\sum_{i=1}^M W(E_i') \chi_g^E(\tilde{E}_i) \chi_n^{\hat{\Omega}}(\tilde{\Omega}_i)}. \quad (69)$$

Finally, for ease of notation when describing error calculations, we define

$$\zeta_{g'g}^{n'n} \equiv \frac{M_{g,n}}{M} \frac{\sum_{i=1}^M \left[\left(\sigma^s(E_i') W(E_i') \right)^2 \chi_g^E(\tilde{E}_i) \chi_n^{\hat{\Omega}}(\tilde{\Omega}_i) \right]}{\sum_{i=1}^M W(E_i') \chi_g^E(\tilde{E}_i) \chi_n^{\hat{\Omega}}(\tilde{\Omega}_i)}. \quad (70)$$

In later chapters, we examine the behavior of the T-matrix, and demonstrate its application in a number of transport calculations.

6. Description of the Monte Carlo Transport Approach

Use of Monte Carlo (MC) integration is advantageous for two reasons.

First, Monte Carlo methods tend to be more efficient for integrals of greater than a few dimensions (here there are five: E' , $\hat{\Omega}'(\xi', \omega')$, μ_L , and ω_L).

Second, the way the MC draws are performed to calculate the scattering cross sections, angular distributions and neutron energies after collision follows the physics of the scatter and closely resembles the methodology of Los Alamos National Laboratory's (LANL) Monte Carlo transport code MCNP.

The previous chapter briefly described how $\bar{\sigma}_{g'g}^{n'n}$ is calculated. This chapter details the implementation of the steps in our code, T-Scat. T-Scat models the physics of the scattering kernel as described in the previous chapter and performs the requisite Monte Carlo calculations. It is based on MCNP¹⁴ and, as such, its capabilities can be greatly expanded. This research examined only the scatter of neutrons, although the same formalism holds for gammas as well.

Where variables are described below, it can be assumed that they come directly from the ACE cross section library. Where exact tabular values are not available, linear interpolationⁱ is typically applied.

ⁱ Some tables (typically of larger nuclides) require other types of interpolation (e.g., Log-Log). Such interpolation is not required for the light nuclei examined here.

Sample the Incident Energy

Once the ACE library is read in, the first step is to draw E' uniformly from the incident energy group. First determine E' from

$$E' = E'_{g+1} + \rho (E'_g - E'_{g+1}) \quad (71)$$

where ρ is a random number on the interval $[0,1)$.

Sample Incident Direction

Facet Quadrature

A preliminary step is to define the tiling of the sphere, \mathcal{U} , into facets, $\Delta\Omega_n$. This defines the angular quadrature. This effort used a modified Cartesian grid with *polecaps*. While any facet quadrature (or surface tiling) can be used (an icosahedron for example) the Cartesian grid makes sampling of the incident facet simple and determination of the scattered facet straight forward. A 74 facet quadrature is shown in Figure 6 and Figure 7.

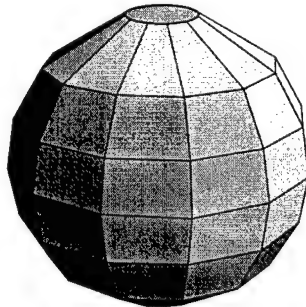


Figure 6. 74 Facet Polecap Quadrature

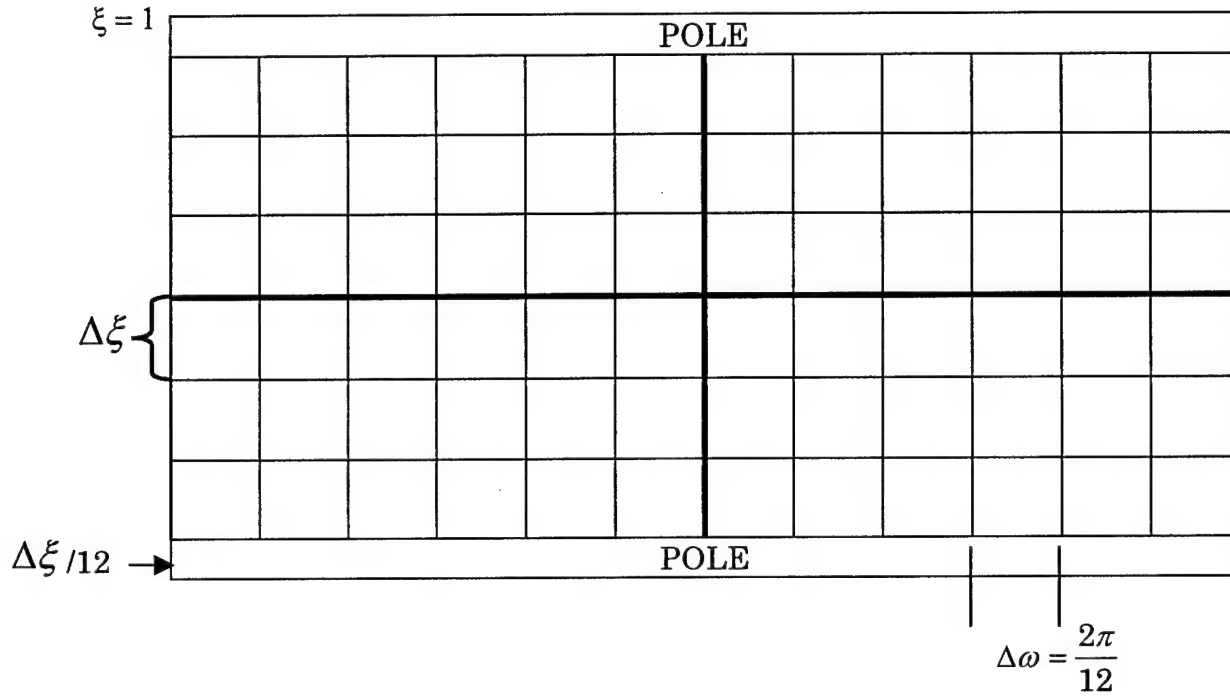


Figure 7. 74 Facet Structure on a Cartesian map.

Most transport codes are unable to use this quadrature set because there are ordinates at the poles. The transport code used for this research, TETRAN, uses an unstructured tetrahedral mesh and can use any ordinates. The polecap quadrature facilitates rebalancing to conserve the first angular moment of the scatter, as described in the next chapter. To be general, T-Scat can also create scattering matrices for Cartesian meshes without ordinates at the poles, but no rebalancing technique has been developed for such a quadrature set.

Each facet of the sphere has the same solid angle. The azimuth is divided with equally spaced lines of longitude ($\Delta \omega = \text{constant}$). If N_ω is the number of longitudinal lines dividing the azimuth then

$$\Delta\omega = \frac{2\pi}{N_\omega}. \quad (72)$$

The same equi-partition is applied to the polar angle with a different treatment at the poles. To assist in the conservation of the first angular moment of the scatter, a cap has been placed on each pole. This polecap has the same solid angle as the other rectangular (in ξ, ω coordinates) facets. The result is that the polecap has a smaller polar width than the other facets.

Dividing the polar angle $[-1,1]$ with N_ξ divisions the polecap polar width is

$$\Delta\xi_{pole} = \frac{2}{2 + N_\omega(N_\xi - 2)}, \quad (73)$$

while for a *rectangular* facet

$$\Delta\xi = \frac{2N_\omega}{2 + N_\omega(N_\xi - 2)}. \quad (74)$$

The total number of facets, N , is

$$N = 2 + N_\omega(N_\xi - 2). \quad (75)$$

As a means of simplifying the description of the quadrature, this paper refers to a given quadrature set as $N_\xi \times N_\omega \rightarrow N$ so that $8 \times 12 \rightarrow 74$ defines a

quadrature set that has $6 \times 12 = 72$ rectangular facets and two polecaps for a total of 74 facets or angular ordinates.

In general, the directional ordinates for any arbitrary facet quadrature are found from

$$\hat{\Omega}_n \equiv \frac{\int_n \frac{d\hat{\Omega}}{\Delta\Omega_n} \hat{\Omega}}{\left\| \int_n \frac{d\hat{\Omega}}{\Delta\Omega_n} \hat{\Omega} \right\|} = \frac{\int_n d\hat{\Omega} \hat{\Omega}}{\left\| \int_n d\hat{\Omega} \hat{\Omega} \right\|}. \quad (76)$$

where the directional vector, $\hat{\Omega}$, is

$$\hat{\Omega}(\omega, \xi) = \sqrt{1 - \xi^2} \cos(\omega) \hat{i} + \sqrt{1 - \xi^2} \sin(\omega) \hat{j} + \xi \hat{k}, \quad (77)$$

and $\|\hat{\Omega}\|$ is the Euclidean norm of $\hat{\Omega}$,

$$\|\hat{\Omega}\| = \sqrt{\Omega_i^2 + \Omega_j^2 + \Omega_k^2}. \quad (78)$$

Integrating equation (76) over a given facet where $\omega \in [\omega_-, \omega_+]$, and

$\xi \in [\xi_-, \xi_+]$ gives

$$\int_n d\hat{\Omega} \hat{\Omega} = \int_{\xi_-}^{\xi_+} d\xi \int_{\omega_-}^{\omega_+} d\omega \left[\sqrt{1 - \xi^2} \cos(\omega) \hat{i} + \sqrt{1 - \xi^2} \sin(\omega) \hat{j} + \xi \hat{k} \right]. \quad (79)$$

The azimuthal angle, relative to the facet edge, is easily found as

$$\omega = \tan^{-1} \left[\int_{\omega_-}^{\omega_+} d\omega \sin(\omega) / \int_{\omega_-}^{\omega_+} d\omega \cos(\omega) \right] = \omega_- + \frac{1}{2}(\omega_+ - \omega_-). \quad (80)$$

The polar cosine is a bit more difficult to calculate. The \hat{k} component of equation (76) is

$$\begin{aligned} \xi \equiv \Omega_{\hat{k}} &= \Delta\omega(\xi_+^2 - \xi_-^2) \\ &\div \left[\Delta\omega^2(\xi_+^2 - \xi_-^2)^2 \right. \\ &\quad \left. + 4\sin^2\left(\frac{\Delta\omega}{2}\right) \left(\xi_+ \sqrt{1 - \xi_+^2} - \xi_- \sqrt{1 - \xi_-^2} + \sin^{-1}(\xi_+) - \sin^{-1}(\xi_-) \right)^2 \right]^{1/2}. \end{aligned} \quad (81)$$

For even modest facet widths, $\Delta\omega < \pi/4$, this is approximated by

$$\begin{aligned} \xi &\approx (\xi_+^2 - \xi_-^2) \\ &\div \left[(\xi_+^2 - \xi_-^2)^2 + \left(\xi_+ \sqrt{1 - \xi_+^2} - \xi_- \sqrt{1 - \xi_-^2} + \sin^{-1}(\xi_+) - \sin^{-1}(\xi_-) \right)^2 \right]^{1/2}, \end{aligned} \quad (82)$$

and for $\Delta\xi < 0.3$, this is further simplified by

$$\xi \approx \frac{(\xi_+ + \xi_-)}{2} = \xi_- + \frac{\Delta\xi}{2}, \quad (83)$$

which is good to about one percent. For the 8 x 12→74 facet quadrature set,

the polar angles of the ordinates using equation (81) are found at

$\xi = \pm 0.165, \pm 0.494, \pm 0.826, \pm 1.00$. While the polar angles using equation (83)

are found at $\xi = \pm 0.162, \pm 0.486, \pm 0.811, \pm 1.00$. For this research,

equations (80) and (81) are used to obtain directional ordinates.

There is a substantial literature discussing more complicated two-angle quadrature sets particularly in modeling molecular structures^{16,17,18,19}. Some of these could be drawn from to create more appropriate quadrature sets.

The Monte Carlo facet method could be used for such quadratures as shown in Figure 8.

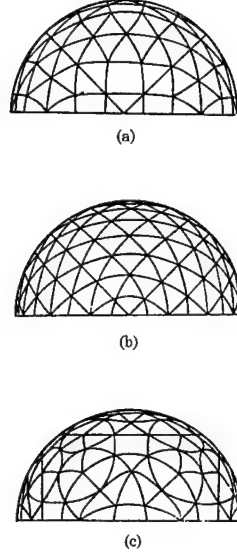


Figure 8. Quadrature schemes proposed by Lebedev¹⁹. a) Lebedev quadrature, b) Uniform triangulation, c) Chebyshev quadrature

Facet Sampling

The incident facet is sampled in the following way. Let ρ_1 and ρ_2 again be random numbers on $[0,1)$. Then for the given incident facet, n' ,

$$\xi' = \xi'_- + \rho_1(\xi'_+ - \xi'_-), \quad (84)$$

and
$$\omega' = \omega'_- + \rho_2(\omega'_+ - \omega'_-). \quad (85)$$

These values are stored until the lab frame scattering angle is determined.

Select the Collision Nuclide

There are two ways multiple nuclei (or isotopes) in a material may be handled. In the first method, the scattering matrices for the nuclides (or isotopes) are calculated separately. The resultant matrices are then mixed in an appropriate way after the calculation. In general, when there are M different nuclides forming the material then

$$T_{tot} = \sum_{i=1}^M T_i f_i , \quad (86)$$

where f_i is the atom fraction of nuclide i . For H_2O this is

$$T_{H_2O} = 2T_H + T_O . \quad (87)$$

The alternative is to have T-Scat select the collision nuclide as part of the sampling of the physics. When this is done, T-Scat follows the methodology of MCNP. If there are M different nuclides forming the material then the k^{th} nuclide is selected if

$$\sum_{i=1}^{k-1} \sigma_i^t f_i < \xi \sum_{i=1}^M \sigma_i^t f_i \leq \sum_{i=1}^k \sigma_i^t f_i , \quad (88)$$

where ξ is a random number on $[0,1)$, and σ_i^t is the total cross section of nuclide i . The total and scattering cross sections are found as

$$\sigma^t(E') = \sum_{i=1}^M \sigma_i^t(E') f_i , \quad (89)$$

and,
$$\sigma^s(E') = \sum_{i=1}^M \sigma_i^s(E') f_i . \quad (90)$$

While the second method provides the user with a scattering matrix that doesn't need further mixing, the first method has a number of advantages. If five million draws were used to create each of T_H , T_O , and T_{H_2O} , then by mixing T_H with T_O the number of samples has effectively doubled. Further, once the scattering matrices have been created for a number of selected isotopes, they form a fixed data library. The user can then select desired nuclides to build the material of choice. This is comparable to present cross section libraries ENDF/B-VI and MATXS-10 discussed in detail later.

Determine Type of Scatter

For a known nuclide and incident neutron energy in the lab frame, E' , the next step is to determine if the scatter is elastic or inelastic. We proceed in the following way: Selection of an elastic collision is made with probability

$$P_{el} = \frac{\sigma_{el}(E')}{\sigma_{in}(E') + \sigma_{el}(E')} = \frac{\sigma_{el}(E')}{\sigma_T(E') - \sigma_a(E')} \quad (91)$$

where

σ_{el} is the elastic scattering cross section,

σ_{in} is the inelastic scattering cross section,

σ_a is the absorption cross section, and

σ_T is the total cross section, $\sigma_T = \sigma_{el} + \sigma_{in} + \sigma_a$.

For an incident neutron energy (in the lab frame), E' , bounded by two values on the cross section table $E'_k < E' \leq E'_{k+1}$, where k is the table index, the cross section, $\sigma(E')$, is found from

$$\sigma(E') = \sigma(E'_k) + \frac{E' - E'_k}{E'_{k+1} - E'_k} [\sigma(E'_{k+1}) - \sigma(E'_k)]. \quad (92)$$

A plot of the total collision scattering cross section, $\sigma_T(E'_k)$, taken from the continuous energy ACE file for oxygen is shown in Figure 9 and Figure 10.

The plot of Figure 10 shows the detail of the resonance region for oxygen.

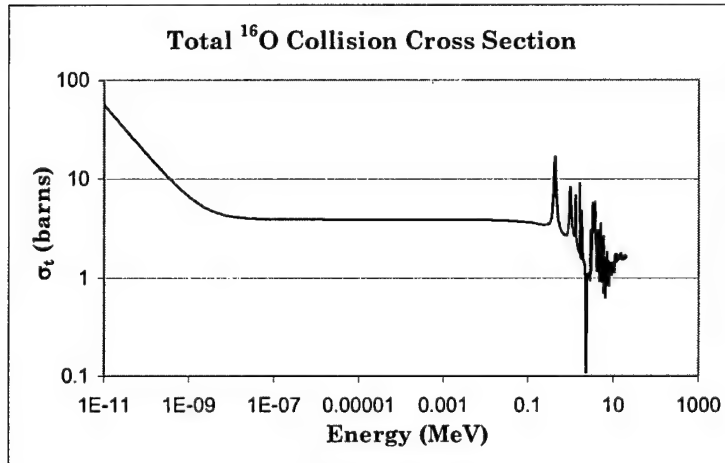


Figure 9. Total collision ^{16}O cross section from ACE file.

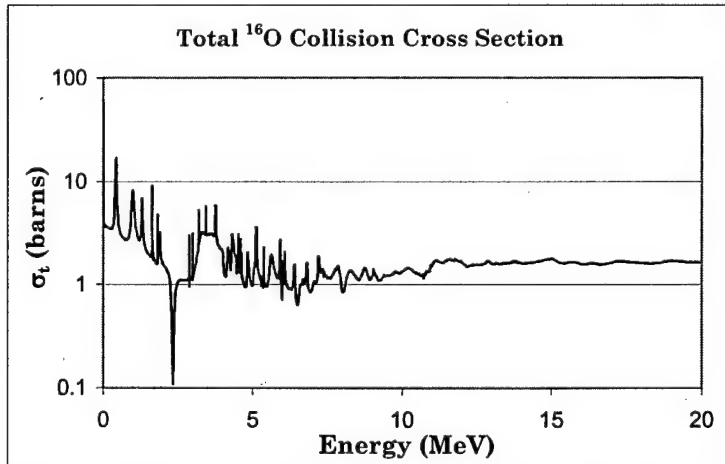


Figure 10. Total collision ^{16}O cross section from ACE file (1-20 MeV)

If the collision is determined to be inelastic, the type of inelastic reaction, n , is sampled from

$$\sum_{i=1}^{n-1} \sigma_i(E') < \rho \sum_{i=1}^N \sigma_i(E') \leq \sum_{i=1}^n \sigma_i(E'), \quad (93)$$

where N is the number of inelastic reactions [e.g., (n,2n), (n,n1), (n,n2), etc.] with cross sections found from the σ_i 's. The same random number used to determine if the scatter was elastic is now re-normalized to the interval [0,1) to select the type of inelastic collision. This new random number, ρ , is found from the old random number with

$$\rho = \frac{\rho_{old} - P_{el}}{1 - P_{el}} \quad (94)$$

thus saving another call to the random number generator.

Just as in MCNP, for elastic and discrete inelastic scatters, the scattered angle is determined from equi-probable angular distribution tables, and the scattered energy is determined from two-body kinematics. For other inelastic processes, the energy of the scattered particle is determined from secondary energy distribution laws, which vary according to the particular inelastic collision modeled¹⁴. To simplify development of the code while still demonstrating the potential of the MC facet method, T-Scat limits its calculations to elastic, discrete inelastic, and continuum scattering using the inelastic evaporative spectrum scattering law (described below). The other

ENDF scattering laws used by MCNP can be easily added to the T-Scat code as simple *case* options in FORTRAN-90.

For both elastic and level inelastic scattering τ is the scattering angle in the center-of-mass frame, μ_{cm} . Thus, μ_{cm} is sampled from its tabulated distribution, and it determines μ_L and E . The μ_{cm} angular distribution tables are represented in the same way. The tables consist of 32 equiprobable cosine bins in the center-of-mass frame (μ_{cm}), and are given at a number of different incident lab frame energies, E'_j , where j is the table index. (Typically the table for the lowest incident energy, E'_0 , for the selected reaction is assumed isotropic.) The table format is outlined in Table 1. Note that there are 33 scattering angles defining the 32 bins.

Table 1. Equiprobable scattering bins from ACE file.

Table Energies	CM Scattering angles			
E'_0	$\mu^{cm}_{0,0}$	$\mu^{cm}_{0,1}$...	$\mu^{cm}_{0,32}$
\vdots	\vdots	\vdots	\ddots	\vdots
E'_j	$\mu^{cm}_{j,0}$	$\mu^{cm}_{j,1}$...	$\mu^{cm}_{j,32}$

The table values for hydrogen are shown in Figure 11, while the same type of chart is shown for ^7Li in Figure 12.

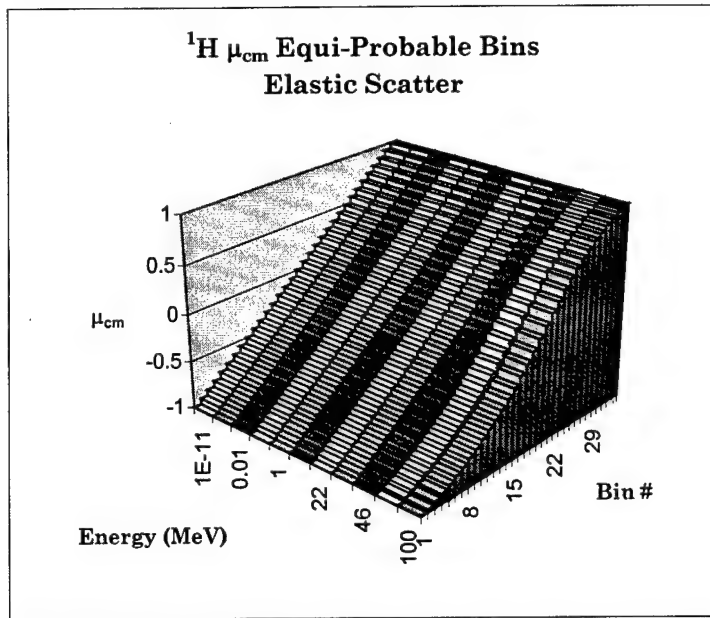


Figure 11. ^1H Equi-Probable Bins Elastic Scattering Table

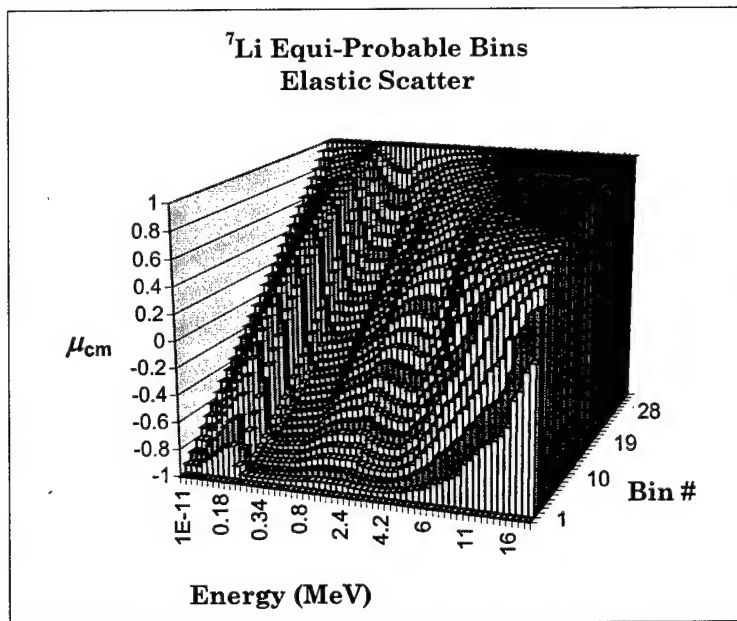


Figure 12. ^7Li Equi-Probable Bins Elastic Scattering Table

Note that the table for hydrogen is nearly isotropic for all energies in the center-of-mass frame. Hydrogen gets its anisotropy when the scatter is converted to the lab frame because of its low atomic weight. The anisotropy

in the center-of-mass frame is seen at high energy for lithium. The data table can be used to create a cumulative distribution function of the scatter at the given energies. Such a table is shown in Figure 13 for ${}^7\text{Li}$. From the figure, it is easy to see that at high energies the probability of drawing a scatter in the forward direction ($\mu_{cm} = 1$) is greater than at low energies. This forward distribution is enhanced when converting the scatter to the lab frame for light nuclides.

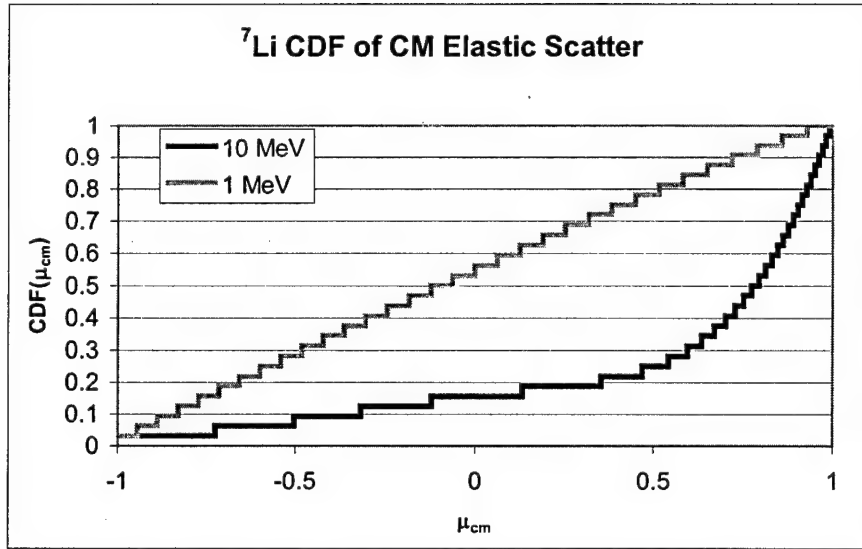


Figure 13. CDF of the CM elastic scatter for ${}^7\text{Li}$ at 1 and 10 MeV.

If E'_j is the energy of table j and E'_{j+1} is the energy of table $j+1$ then a value of the scattering angle μ_{cm} is sampled from table $j+1$ with probability $(E' - E'_j) / (E'_{j+1} - E'_j)$ and from table j with probability $(E'_{j+1} - E') / (E'_{j+1} - E'_j)$. A random number ρ on the interval $[0,1)$ is then used to select the i^{th} cosine bin such that $i = \text{floor}[32\rho + 1]$. The value of μ_{cm} is then computed as

$$\mu_{cm} = \mu_i + (32\rho - i)(\mu_{i+1} - \mu_i). \quad (95)$$

If μ_{cm} is isotropic it is found on $[-1,1)$ as

$$\mu_{cm} = 2\rho - 1. \quad (96)$$

Elastic Scattering

For elastic scattering, once the scattering angle is calculated the scattered energy E is determined from two-body kinematics. In the laboratory frame it is

$$E = E' \left[\frac{1 + A^2 + 2A\mu_{cm}}{(1 + A)^2} \right], \quad (97)$$

where A is the atomic weight and E' is the incident neutron energy.

Level Inelastic scattering

For level inelastic scattering (a.k.a. MCNP law 3), the energy of the scattered neutron is found from basic kinematics. In the center-of mass frame the scattered energy is

$$E_{cm} = \left(\frac{A}{A+1} \right)^2 \left[E' - \frac{|Q|(A+1)}{A} \right], \quad (98)$$

where Q is the excitation energy of the nucleus. This equation can also be used to find the exiting energy in the center of mass frame for elastic scattering by setting $Q=0$. The outgoing energy in the laboratory frame is

$$E = E_{cm} + \frac{E' + 2\mu_{cm}(A+1)\sqrt{E'E_{cm}}}{(A+1)^2}. \quad (99)$$

Evaporation Spectrum

The evaporation spectrum reaction is one way to model scattering to the continuum. The distribution is sampled independently of the angular draw. Hence, energy conservation is not strictly enforced for each individual collision, but overall energy conservation is approached as the number of draws becomes large. The spectrum is given as¹⁴

$$f(E' \rightarrow E) = CE_{cm} e^{-E_{cm}/T(E')}, \quad (100)$$

where the nuclear temperature, $T(E')$, is a tabulated function of the incident energy. The energy U is provided in the library and is assigned so that E_{cm} is limited by $0 \leq E_{cm} \leq E' - U$. The normalization constant C is given by

$$C^{-1} = T^2 \left[1 - e^{-(E' - U)/T} (1 + (E' - U)/T) \right]. \quad (101)$$

As in MCNP, T-Scat samples the density function with

$$E_{cm} = -T(E') \ln(\rho_1 \rho_2), \quad (102)$$

where ρ_1 and ρ_2 are random numbers on $(0,1]$ and are rejected if $E_{cm} > E' - U$.

This completes the set of scatter reactions that are currently implemented in T-Scat. There are some thirteen different laws for neutrons and more for photons (See Appendix B: The Inelastic Neutron Scattering Laws of MCNP). All could be incorporated into the same algorithm with the goal of determining the scattered angle, μ_L , and scattered energy E .

Finding the New Direction

Once the scattering angle (in the center-of-mass frame) and energy (in both center-of-mass frame and lab frame) are known, the direction of the exiting neutron is found in the following way where we assume that the target is at rest. First the cosine of the scattering angle in the laboratory frame, μ_L , is found from

$$\mu_L = \mu_{cm} \sqrt{\frac{E_{cm}}{E}} + \frac{1}{A+1} \sqrt{\frac{E'}{E}}. \quad (103)$$

The incident particle direction cosines, (μ', η', ξ') are rotated to new scattered cosines (μ, η, ξ) , through a polar angle whose cosine is μ_L , and through an azimuthal angle sampled uniformly. Conceptually, we sample ω_L as discussed above. However, to avoid expensive evaluations of trigonometric functions, we sample its components by rejection as follows.

For random numbers ρ_1 and ρ_2 on the interval $[-1,1)$ with rejection criterion

$\rho_1^2 + \rho_2^2 \leq 1$, the general equations are

$$\mu = \mu' \mu_L + \frac{\sqrt{1 - \mu_L^2} (\rho_1 \mu' \xi' - \rho_2 \eta')}{\sqrt{(\rho_1^2 + \rho_2^2)(1 - \xi'^2)}}, \quad (104)$$

$$\eta = \eta' \mu_L + \frac{\sqrt{1 - \mu_L^2} (\rho_1 \eta' \xi' - \rho_2 \mu')}{\sqrt{(\rho_1^2 + \rho_2^2)(1 - \xi'^2)}}, \quad (105)$$

and

$$\xi = \xi' \mu_L + \frac{\sqrt{(1 - \mu_L^2)(1 - \xi'^2)}}{\sqrt{(\rho_1^2 + \rho_2^2)}}. \quad (106)$$

If $1 - \xi'^2 \approx 0$, then an alternative approach is needed to avoid catastrophic cancellation:

$$\mu = \mu' \mu_L + \frac{\sqrt{1 - \mu_L^2} (\rho_1 \mu' \eta' + \rho_2 \xi')}{\sqrt{(\rho_1^2 + \rho_2^2)(1 - \eta'^2)}}, \quad (107)$$

$$\eta = \eta' \mu_L - \frac{\rho_1 \sqrt{(1 - \mu_L^2)(1 - \eta'^2)}}{\sqrt{(\rho_1^2 + \rho_2^2)}}, \quad (108)$$

and

$$\xi = \xi' \mu_L + \frac{\sqrt{(1 - \mu_L^2)} (\rho_1 \xi' \eta' - \rho_2 \mu')}{\sqrt{(\rho_1^2 + \rho_2^2)(1 - \eta'^2)}}. \quad (109)$$

If the scattering distribution is isotropic in the lab frame, it is possible to use an even simpler formulation that takes advantage of the exiting direction cosines being independent of the incident direction cosines. In this case,

$$\mu = 2(\rho_1^2 + \rho_2^2) - 1, \quad (110)$$

$$\eta = \rho_1 \sqrt{\frac{1 - \mu^2}{\rho_1^2 + \rho_2^2}}, \quad (111)$$

and

$$\xi = \rho_2 \sqrt{\frac{1 - \mu^2}{\rho_1^2 + \rho_2^2}}. \quad (112)$$

where ρ_1 and ρ_2 are rejected if $\rho_1^2 + \rho_2^2 > 1$.

A simple variance reduction technique would be to split the scattered neutron for a fixed number of azimuthal angles, rather than draw the

azimuthal angle for a single number. For example, select a random number, ρ , on $[0,1)$. Then, for $i=1,2,..360$ select 360 azimuthal angles by

$$\omega_i = (i + \rho - 1) \frac{2\pi}{360}. \quad (113)$$

Now that the physics has been applied to the scattering, the next step is to identify the facet and group in which $\hat{\Omega}$, and E lie.

Identifying Scattered Energy Group and Facet

As required by equation (63), for each sample, once the scattered energy and direction are known the appropriate scattered group and facet must be identified. In many cases, particularly at high energies for heavy nuclei, little energy is lost in the collision. An example of this for oxygen is shown in Figure 14. This suggests that using the previous scattered energy as a first guess for the next search might improve performance.

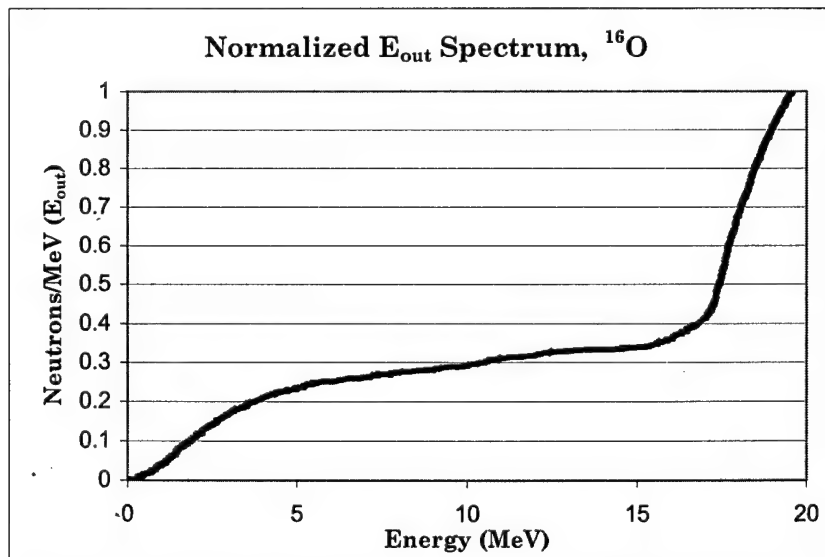


Figure 14. Scattered energy spectrum for ^{16}O for incident $E' \in [17.333, 19.64]$.

Once the scattered energy, E , is known, a search is performed on the group structure to determine the appropriate scattered group $E_i \in (E_g, E_{g-1}]$. A bisection search can be done, but we've found that at high energies using the last known scattered energy as a first guess improves code performance by about 2% (175 group structure). The *hunt* routine was found in Numerical Recipes²⁰.

The next step is to find the facet for which $\hat{\Omega}_i \in \Delta\Omega_n$. For the Cartesian grid, no search really needs to be performed. Once the scattered direction $\hat{\Omega}_i = (\mu_i, \eta_i, \xi_i)$ is determined, the azimuthal angle, ω , is found from

$$\omega_i = \tan^{-1}\left(\frac{\eta_i}{\mu_i}\right), \quad \omega_i \in [-\pi, \pi]. \quad (114)$$

The azimuthal facet index, i_ω , is

$$i_\omega = \text{int}\left(N_\omega \frac{\omega + \pi}{2\pi}\right) + 1, \quad (115)$$

while the latitudinal facet index, i_ξ , is

$$i_\xi = \text{int}\left(\frac{\xi}{\Delta\xi} + 0.5N_\xi\right) + 1. \quad (116)$$

The scattered facet index, n , is then

$$n = i_\omega + N_\omega(i_\xi - 1). \quad (117)$$

For the given incident group, g' , and facet, n' , the scattered group, g , and facet, n , have now been determined. The following tallies are accumulated:

$$\bar{\sigma}_{g'g,n'n}^{Num}(new) = \bar{\sigma}_{g'g,n'n}^{Num}(old) + \sigma(E_i')W(E_i'), \quad (118)$$

$$\bar{\sigma}_{g'n'}^{Den}(new) = \bar{\sigma}_{g'n'}^{Den}(old) + W(E_i'), \quad (119)$$

and
$$\bar{\sigma}_{g'g,n'n}^{Err}(new) = \bar{\sigma}_{g'g,n'n}^{Err}(old) + [\sigma(E_i')W(E_i')]^2. \quad (120)$$

After a set number of draws, M , the T-matrix is calculated from

$$T_{g'g}^{n'n} \approx \frac{\Delta\Omega_{n'}}{\Delta\Omega_n} \frac{M_{g,n}}{M} \frac{\bar{\sigma}_{g'g,n'n}^{Num}(new)}{\bar{\sigma}_{g'g,n'n}^{Den}(new)}, \quad (121)$$

where $M_{g,n}$ is the number of counts in group g and facet n . The T-matrix error is found from

$$\varepsilon_{g'g}^{n'n} \approx 1.96 \frac{\Delta\Omega_{n'}}{\Delta\Omega_n} \frac{\sqrt{\frac{1}{M} \left\{ \left[\frac{1}{M} \bar{\sigma}_{g'g,n'n}^{Err}(new) \right] - \left[\frac{1}{M} \bar{\sigma}_{g'g,n'n}^{Num}(new) \right]^2 \right\}}}{\left[\frac{1}{M_{g,n}} \bar{\sigma}_{g'g,n'n}^{Den}(new) \right]}. \quad (122)$$

If the desired error is not met, or the maximum number of draws has not been exceeded, the number of draws is doubled and the process is repeated.

A number of data files are output including the T-matrix, the error in the T-matrix, the counts, $M_{g,n}$, for each incident to scattered facet and group, as well as the average angle of scatter, $\hat{\Omega}_{g'g}^{n'n}$, which is used to conserve the first angular moment of the scatter.

7. Conserving the First Angular Moment of the T-Matrix

In the Monte Carlo facet method, scattered neutrons are tallied according to the facet and energy group into which they scatter. In the transport code, the angular flux, $\psi_{g,n}$, is discretized such that the neutrons propagate along the directional ordinate, $\hat{\Omega}_n$. When calculating the average scatter in the MC facet method, in the case of highly anisotropic scattering, only a small part of a scattered facet may be reached. The assumption that these neutrons travel in the direction of that facet's ordinate (equation (76)) is tantamount to a very large redistribution of the scattered neutrons away from their intended direction.

Here we fix this redistribution, to first order, by actually tracking the first angular moment of the scatter (or average scattering angle) within each angular facet. As is shown below, conserving first angular moments is required if the T-matrix is to support codes running diffusion-like problems.

In this chapter we describe the diffusion theory's requirement for first angular moment conservation. We then describe the theory behind the rebalance of the T-matrix. Impact of this rebalance technique on transport computations is shown in subsequent chapters.

The P₁ Approximation and Diffusion Theory

This discussion follows the presentations of Bell and Glasstone², and Marchuck and Lebedev²¹. It is a brief review of diffusion theory, and helps

explain why conserving the average angle of scatter is important in diffusion theory.

The steady state P_1 equations used in diffusion theory are

$$\nabla \cdot \vec{J}(\vec{r}, E) + \sigma(\vec{r}, E)\phi(\vec{r}, E) = q_0(r, E) + \int dE' \sigma_{S0}(\vec{r}, E' \rightarrow E)\phi(\vec{r}, E'), \quad (123)$$

and

$$\frac{1}{3}\nabla\phi(\vec{r}, E) + \sigma(\vec{r}, E)\vec{J}(\vec{r}, E) = \vec{q}_1(r, E) + \int dE' \sigma_{S1}(\vec{r}, E' \rightarrow E)\vec{J}(\vec{r}, E'), \quad (124)$$

where

$$q_0(\vec{r}, E) = \int d\Omega q(\vec{r}, \hat{\Omega}, E), \quad (125)$$

$$\vec{q}_1(\vec{r}, E) = \int d\Omega \vec{\Omega} q(\vec{r}, \hat{\Omega}, E), \quad (126)$$

and, for azimuthally symmetric scattering

$$\sigma_{S0}(\vec{r}, E' \rightarrow E) = \int d\Omega \int d\Omega' \sigma_S(\vec{r}, E' \rightarrow E, \hat{\Omega}' \cdot \hat{\Omega}), \quad (127)$$

$$\sigma_{S1}(\vec{r}, E' \rightarrow E) = \int d\Omega \int d\Omega' \hat{\Omega}' \cdot \hat{\Omega} \sigma_S(\vec{r}, E' \rightarrow E, \hat{\Omega}' \cdot \hat{\Omega}), \quad (128)$$

where $\mu_L = \hat{\Omega}' \cdot \hat{\Omega}$.

In the diffusion approximation, $\vec{q}_1(\vec{r}, E)$ is assumed to be isotropic. Then the current density, defined as

$$\vec{J}(\vec{r}, E) \equiv \int d\hat{\Omega} \hat{\Omega} \psi(\vec{r}, \hat{\Omega}, E), \quad (129)$$

can be represented in terms of the scalar flux, $\phi(\vec{r}, E)$, as

$$\bar{J}(\vec{r}, E) = -D(\vec{r}, E) \nabla \phi(\vec{r}, E), \quad (130)$$

where

$$D(\vec{r}, E) = \frac{1}{3} [\sigma(\vec{r}, E) - \bar{\mu}_L(\vec{r}, E) \sigma_{S0}(\vec{r}, E)]^{-1}, \quad (131)$$

and the average angle of scatter, $\bar{\mu}_L(\vec{r}, E)$, is found from

$$\bar{\mu}_L(\vec{r}, E) = \frac{\int_0^E dE'' \int d\Omega' \int d\Omega \hat{\Omega}' \cdot \hat{\Omega} \sigma_S(\vec{r}, E \rightarrow E'', \hat{\Omega}' \cdot \hat{\Omega})}{\int_0^E dE'' \int d\Omega' \int d\Omega \sigma_S(\vec{r}, E \rightarrow E'', \hat{\Omega}' \cdot \hat{\Omega})}. \quad (132)$$

Equation (130) is used instead (124) to eliminate $\bar{J}(\vec{r}, E)$ from equation (123) and gives the diffusion equation

$$\begin{aligned} -\nabla \cdot [D(\vec{r}, E) \nabla \phi(\vec{r}, E)] + \sigma(\vec{r}, E) \phi(\vec{r}, E) &= q_0(r, E) \\ &+ \int dE' \sigma_{S0}(\vec{r}, E' \rightarrow E) \phi(\vec{r}, E'). \end{aligned} \quad (133)$$

Knowing the total cross section, $\sigma(\vec{r}, E)$, the scattering cross section, $\sigma_{s0}(\vec{r}, E)$, and the average scattering angle, $\bar{\mu}_0(\vec{r}, E)$, we can calculate the diffusion coefficient and use it in diffusion problems. T-Scat tracks all these quantities (groupwise) as is discussed below.

Validity of the MC Facet Method in the Diffusion Limit

Proper calculation of both the scalar flux and current are necessary for proper transport code operation in the diffusion limit. To accurately calculate

the currents, we need the scattering cross sections to be accurate at least to the first angular moment of scatter. Further, the facet quadrature employed must integrate the zeroth and first moment of the angular flux accurately.

Conserving the first angular moment of the scatter is described in the following section. Here, we perform a quick check on the accuracy of the Cartesian quadrature (with *polecaps*).

The $\frac{1}{3}$ in equation (124) arises as²³

$$\frac{\int d\Omega \hat{\Omega} \hat{\Omega}}{\int d\Omega} = \frac{1}{3} \begin{bmatrix} 1 & 0 & 0 \\ 0 & 1 & 0 \\ 0 & 0 & 1 \end{bmatrix}. \quad (134)$$

For our quadrature, we would want

$$\frac{\int d\Omega \mu^2}{\int d\Omega} = \frac{\int d\Omega \eta^2}{\int d\Omega} = \frac{\int d\Omega \xi^2}{\int d\Omega} = \frac{1}{3}. \quad (135)$$

To get proper performance in the diffusion limit, we need

$$\frac{\sum_{n=1}^N \mu_n^2 \Delta\Omega_n}{\sum_{n=1}^N \Delta\Omega_n} = \frac{1}{3} \quad (136)$$

exactly, and similarly for η and ξ direction cosines. As long as

$$\hat{\Omega}_n = \frac{\int_{\Delta\Omega_n} d\Omega \hat{\Omega}}{\left\| \int_{\Delta\Omega_n} d\Omega \hat{\Omega} \right\|}, \quad (137)$$

this will never be exact. Still, the values are close. For the 74 facet quadrature described earlier,

$$\frac{\sum_{n=1}^N \mu_n^2 \Delta\Omega_n}{\sum_{n=1}^N \Delta\Omega_n} = \frac{\sum_{n=1}^N \eta_n^2 \Delta\Omega_n}{\sum_{n=1}^N \Delta\Omega_n} = 0.332, \quad (138)$$

and

$$\frac{\sum_{n=1}^N \xi_n^2 \Delta\Omega_n}{\sum_{n=1}^N \Delta\Omega_n} = 0.336, \quad (139)$$

corresponding to less than a 1% error in the approximation.

T-Matrix Rebalance to Conserve First Angular Moment

Just as diffusion theory requires knowledge of the first angular moment of the scattering cross section, for diffusion-like problems, the T-matrix should accurately represent the angular structure of the scatter to first order. Secondly, it would be useful if the diffusion coefficient could be calculated directly from the T-matrix, providing another use for the T-matrix scattering libraries.

The facet tallies described earlier only recorded zeroth order scatter.

T-Scat, however, also tracks the first angular moment of the scatter into each facet for each energy group. Knowledge of the first angular moment within a facet is used to adjust the zeroth moment of the facet's neighbors to preserve the first angular moment within the discrete ordinate structure. This section describes how that is done.

For discrete ordinates, a single angular ordinate represents a facet. If we simply sum the total number of counts within a facet and determine the average (based on their weights), we have a zeroth order approximation and lose the information concerning the average scattering angle within the facet. It is possible within the T-Scat code, however, to track the average scattering angle within a given facet. As the T-matrix is calculated, for each count within a given scattered facet (and energy), we record the angular direction of the scattered particle, $\hat{\Omega}_i$, and its appropriate scattering weight (equation (69)). The average of the scattering direction ($\bar{\hat{\Omega}}$) is calculated from

$$\bar{\hat{\Omega}}_{g'g}^{n'n} = \frac{\sum_{i=1}^N \left[\hat{\Omega}_i \sigma^s(E'_i) W(E'_i) \chi_g^E(\tilde{E}_i) \chi_n^{\hat{\Omega}}(\tilde{\Omega}_i) \right]}{\left\| \sum_{i=1}^N \left[\hat{\Omega}_i \sigma^s(E'_i) W(E'_i) \chi_g^E(\tilde{E}_i) \chi_n^{\hat{\Omega}}(\tilde{\Omega}_i) \right] \right\|}, \quad (140)$$

and is output from the code along with the zeroth moment T-matrix. This is graphically represented in Figure 15.

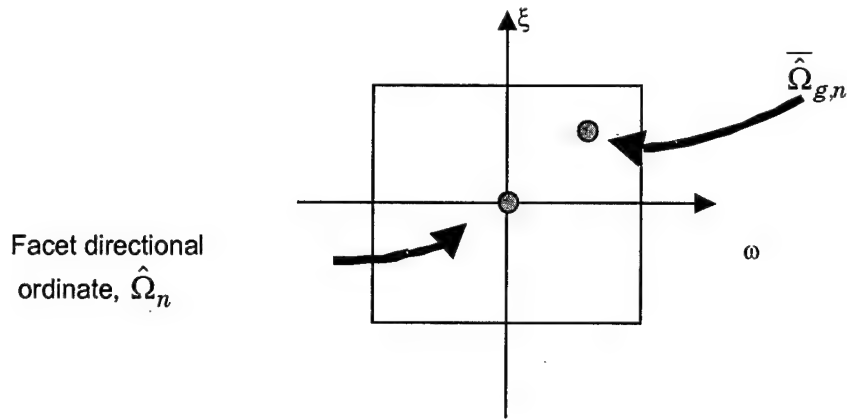


Figure 15. Tracking average scattering direction within a facet.

Process of Rebalancing

There are three general cases for the polecap quadrature that must be considered:

1. Rebalance among *rectangular* facets (*4-point*).
2. Rebalance from a *rectangular* facet to the polecap and a neighboring *rectangular* facet (*3-point*).
3. Rebalance from a polecap to two *rectangular* facets (*3-point*).

In each case, two rules must be followed:

1. Conserve the average angle of scatter.
2. Conserve the zeroth moment of the scatter.

Case 1: Rebalance between normal *rectangular* facets (*4-point*).

For simplicity we discuss facets in the northern hemisphere only.

Realize that the southern hemisphere is handled with a simple reflection of

the theory presented. Consider a scattered facet in which the first moment of the scatters lies in the upper-right quadrant of the facet, here labeled as F_1 (Figure 16).

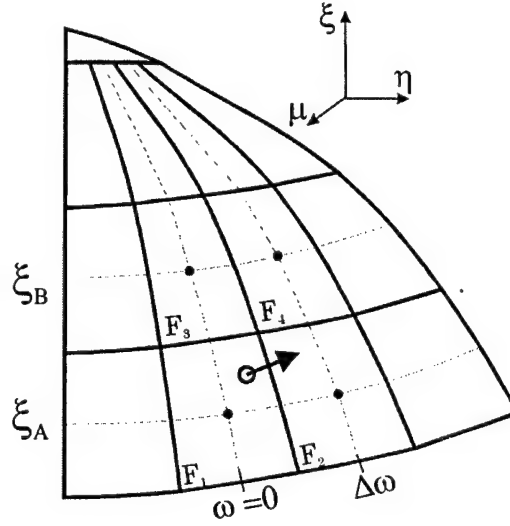


Figure 16. Case 1 rebalance.

The azimuthal angle is rotated so that $\omega = 0$ at the centroid of F_1 . To do this, let

$$\tilde{\omega} = \omega - \omega_j, \quad (141)$$

where the index, j , corresponds to the facet being rebalanced. With this substitution $\tilde{\omega}_1 = \tilde{\omega}_3 = 0$, and $\tilde{\omega}_2 = \tilde{\omega}_4 = \Delta\omega$. The polar variable, ξ , requires no modification. The average direction of scatter is located at $(\tilde{\omega}_o, \xi_o)$. In terms of the directional cosines, the average direction of scatter is $(\tilde{\mu}_o, \tilde{\eta}_o, \xi_o)$.

Let S be the initial zeroth moment of the scatter found for F_1 . After rebalancing, S is apportioned to the appropriate nearest neighbors adding to

the zeroth moments of F_1, F_2, F_3 , and F_4 by s_1, s_2, s_3 , and s_4 respectively.

The directional ordinates of the four facets in terms of $(\tilde{\omega}, \xi)$ or $(\tilde{\mu}, \tilde{\eta}, \xi)$ are simply

$$\hat{\Omega}_1 = (0, \xi_A) \Rightarrow (\tilde{\mu}_1, \tilde{\eta}_1, \xi_A) = (\sqrt{1 - \xi_A^2}, 0, \xi_A), \quad (142)$$

$$\hat{\Omega}_2 = (\Delta\omega, \xi_A) \Rightarrow (\tilde{\mu}_2, \tilde{\eta}_2, \xi_A) = (\sqrt{1 - \xi_A^2} \cos(\Delta\omega), \sqrt{1 - \xi_A^2} \sin(\Delta\omega), \xi_A), \quad (143)$$

$$\hat{\Omega}_3 = (0, \xi_B) \Rightarrow (\tilde{\mu}_3, \tilde{\eta}_3, \xi_B) = (\sqrt{1 - \xi_B^2}, 0, \xi_B), \quad (144)$$

$$\hat{\Omega}_4 = (\Delta\omega, \xi_B) \Rightarrow (\tilde{\mu}_4, \tilde{\eta}_4, \xi_B) = (\sqrt{1 - \xi_B^2} \cos(\Delta\omega), \sqrt{1 - \xi_B^2} \sin(\Delta\omega), \xi_B). \quad (145)$$

Rule 1: Conserve the average angle of scatter. To ensure that the average angle of scatter is conserved we set the tangents of the original and rebalanced directional ordinates equal to each other such that

$$\frac{\tilde{\mu}_o}{\tilde{\eta}_o} = \frac{s_1 \tilde{\mu}_1 + s_2 \tilde{\mu}_2 + s_3 \tilde{\mu}_3 + s_4 \tilde{\mu}_4}{s_1 \tilde{\eta}_1 + s_2 \tilde{\eta}_2 + s_3 \tilde{\eta}_3 + s_4 \tilde{\eta}_4}, \quad (146)$$

and

$$\frac{\tilde{\mu}_o}{\xi_o} = \frac{s_1 \tilde{\mu}_1 + s_2 \tilde{\mu}_2 + s_3 \tilde{\mu}_3 + s_4 \tilde{\mu}_4}{s_1 \xi_1 + s_2 \xi_2 + s_3 \xi_3 + s_4 \xi_4}. \quad (147)$$

We now have two of the four equations necessary to solve the rebalance distribution. Conservation of the zeroth moment with a self-imposed constraint (described below) provides the other two.

Rule 2: Conserve the zeroth moment of the scatter. A 4-point rebalance allows an extra degree of freedom in determining how the zeroth moment is shared between the four facets. Here we choose a bi-linear approach. Of the total amount of S , g is a fraction redistributed to the right, and h is a fraction redistributed up, so that

$$s_1 = (1 - g)(1 - h)S, \quad (148)$$

$$s_2 = g(1 - h)S, \quad (149)$$

$$s_3 = (1 - g)hS, \quad (150)$$

and $s_4 = ghS. \quad (151)$

Summing these equations demonstrates zeroth moment conservation

$$s_1 + s_2 + s_3 + s_4 = S. \quad (152)$$

Thus equations (146) through (151) constitute six equations in six unknowns (s_1, s_2, s_3, s_4, g , and h).

Mathematica was used to solve this system of six equations in six unknowns. The resultant rebalance equations are

$$s_1(\tilde{\omega}_0, \xi_0) = S \frac{N(\xi_B, \tilde{\omega}_0, \xi_0)}{D(\tilde{\omega}_0, \xi_0)} \sin(\Delta\omega - \tilde{\omega}_0), \quad (153)$$

$$s_2(\tilde{\omega}_0, \xi_0) = S \frac{N(\xi_B, \tilde{\omega}_0, \xi_0)}{D(\tilde{\omega}_0, \xi_0)} \sin(\tilde{\omega}_0), \quad (154)$$

$$s_3(\tilde{\omega}_0, \xi_0) = -S \frac{N(\xi_A, \tilde{\omega}_0, \xi_0)}{D(\tilde{\omega}_0, \xi_0)} \sin(\Delta\omega - \tilde{\omega}_0), \quad (155)$$

$$s_4(\tilde{\omega}_0, \xi_0) = -S \frac{N(\xi_A, \tilde{\omega}_0, \xi_0)}{D(\tilde{\omega}_0, \xi_0)} \sin(\tilde{\omega}_0), \quad (156)$$

where,

$$N(\xi_k, \tilde{\omega}_0, \xi_0) = \frac{1}{2} \left[\xi_k \sqrt{1 - \xi_0^2} \csc(\Delta\omega/2) - \xi_0 \sqrt{1 - \xi_k^2} \cot(\Delta\omega/2) \sec(\Delta\omega/2 - \tilde{\omega}_0) \right], \quad (157)$$

where $\xi_k = \xi_A$ or ξ_B , and

$$D(\tilde{\omega}_0, \xi_0) = \xi_0 \left(\sqrt{1 - \xi_A^2} - \sqrt{1 - \xi_B^2} \right) \cos(\Delta\omega/2) + (\xi_B - \xi_A) \sqrt{1 - \xi_0^2} \cos(\Delta\omega/2 - \tilde{\omega}_0). \quad (158)$$

Case 2: Rebalance from a rectangular facet involving the polecap.

The next case to consider is the rectangular facet to polecap rebalance. Again, the first moment lies in the upper, right quadrant of a rectangular facet, directly above which is the polecap. The geometry for this case is shown in Figure 17.

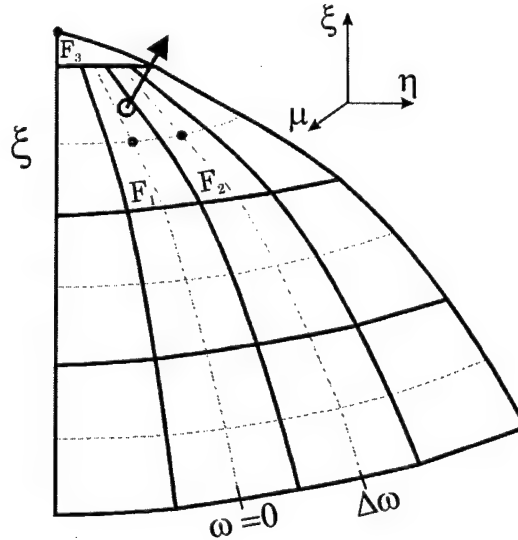


Figure 17. Geometry for 3-point rebalance.

The directional ordinates of the three facets in terms of $(\tilde{\omega}, \xi)$ or $(\tilde{\mu}, \tilde{\eta}, \xi)$

are

$$\hat{\Omega}_1 = (0, \xi) \Rightarrow (\tilde{\mu}_1, \tilde{\eta}_1, \xi) = \left(\sqrt{1 - \xi^2}, 0, \xi \right), \quad (159)$$

$$\hat{\Omega}_2 = (\Delta\omega, \xi) \Rightarrow (\tilde{\mu}_2, \tilde{\eta}_2, \xi) = \left(\sqrt{1 - \xi^2} \cos(\Delta\omega), \sqrt{1 - \xi^2} \sin(\Delta\omega), \xi \right), \quad (160)$$

$$\text{and, } \hat{\Omega}_3 = (NA, 1) \Rightarrow (\tilde{\mu}_3, \tilde{\eta}_3, \xi_3) = (0, 0, 1). \quad (161)$$

As before, we set the tangents of the directional ordinates equal to each other such that

$$\frac{\tilde{\mu}_o}{\tilde{\eta}_o} = \frac{s_1 \tilde{\mu}_1 + s_2 \tilde{\mu}_2 + s_3 \tilde{\mu}_3}{s_1 \tilde{\eta}_1 + s_2 \tilde{\eta}_2 + s_3 \tilde{\eta}_3}. \quad (162)$$

and

$$\frac{\tilde{\mu}_o}{\xi_o} = \frac{s_1 \tilde{\mu}_1 + s_2 \tilde{\mu}_2 + s_3 \tilde{\mu}_3}{s_1 \xi_1 + s_2 \xi_2 + s_3 \xi_3}. \quad (163)$$

We now have two of the three equations necessary to solve the rebalance distribution. Conservation of the zeroth moment provides the other:

$$S = s_1 + s_2 + s_3. \quad (164)$$

The resultant rebalance equations are

$$s_1(\tilde{\omega}_0, \xi_0) = S \frac{\sqrt{1 - \xi_0^2} \csc(\Delta\omega)}{D(\tilde{\omega}_0, \xi_0)} \sin(\Delta\omega - \tilde{\omega}_0), \quad (165)$$

$$s_2(\tilde{\omega}_0, \xi_0) = S \frac{\sqrt{1 - \xi_0^2} \csc(\Delta\omega)}{D(\tilde{\omega}_0, \xi_0)} \sin(\tilde{\omega}_0), \quad (166)$$

$$s_3(\tilde{\omega}_0, \xi_0) = S \frac{\left[\xi_0 \sqrt{1 - \xi^2} - \xi \sqrt{1 - \xi_0^2} \cos(\Delta\omega/2 - \tilde{\omega}_0) \sec(\Delta\omega/2) \right]}{D(\tilde{\omega}_0, \xi_0)}, \quad (167)$$

where,

$$D(\tilde{\omega}_0, \xi_0) = \left[\xi_0 \sqrt{1 - \xi^2} - (\xi - 1) \sqrt{1 - \xi_0^2} \cos(\Delta\omega/2 - \tilde{\omega}_0) \sec(\Delta\omega/2) \right]. \quad (168)$$

Case 3: Rebalance from a polecap to two *rectangular* facets.

Rebalancing from the polecap to its neighbors is done in exactly the same way as the case 2 rebalance. The concept of “nearest neighbor”, however, leads to the conundrum – which neighboring facets are used in the rebalance? A straightforward approach is to say that a first moment slightly offset from the pole shares directly with its nearest neighbors (along the same meridian), and only a 3-point rebalance is performed. Another argument is that such a slight offset should be distributed, in an appropriate manner, with all the pole's neighbors in the first moment's hemisphere. The first method does not take into account that the scattering into a facet may not be uniform. Suppose, for example, that scattering into the pole is bi-modal, such that very few neutrons scattered directly into the center of the pole, while a large number scattered to one side and the other. The resultant first moment would be very near the pole, and when rebalanced, might share with a facet perpendicular to the direction the neutrons truly scattered.

To account for this effect in a consistent manner, the polecap is itself divided into the same number of longitudinal facets as the rest of the sphere as is shown below.

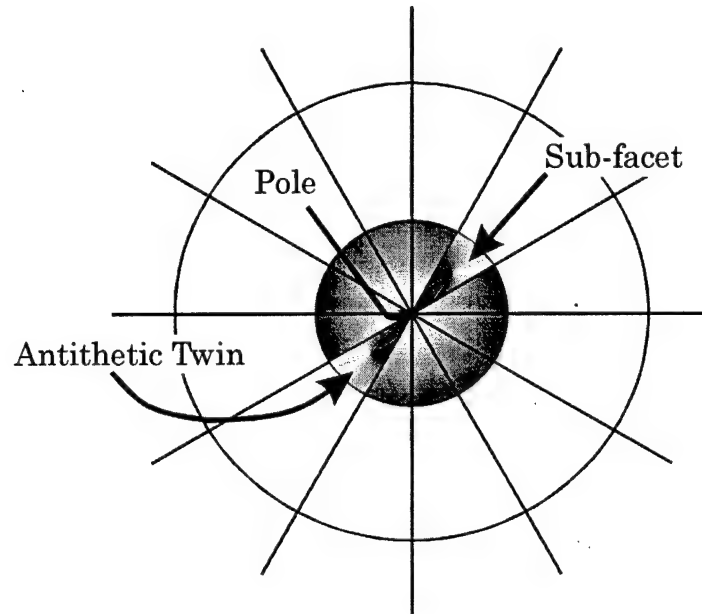


Figure 18. Division of the polecap into sub-facets.

The first moment of the scatter is tracked within each of these sub-facets. It would be nice to use these sub-facet first moments to rebalance directly with the nearest neighbors. Unfortunately, you can't directly. Neutrons scattered isotropically into the pole would result in first moments in each of the sub-facets that were offset from the pole. As such, each would share with its neighbors, when in-fact no sharing should take place at all.

Instead, our approach is to examine each sub-facet with its antithetic twin (the sub-facet directly across the pole). The two first moment vectors are summed to obtain a new first moment direction for the pair ,

$$\bar{\Omega}_{new} = \frac{(T_{g'g}^{n'n} \bar{\Omega}_{g'g}^{n'n}) + (T_{g'g}^{n'n} \bar{\Omega}_{g'g}^{n'n})_{twin}}{\|(T_{g'g}^{n'n} \bar{\Omega}_{g'g}^{n'n}) + (T_{g'g}^{n'n} \bar{\Omega}_{g'g}^{n'n})_{twin}\|}. \quad (169)$$

If the distribution of scattered neutrons into the pole is isotropic the result is a first moment that aligns with the pole. In some cases the new first moment may not point within either of the twin's facets. The facet the new first moment lands in is recorded for each facet pair. The magnitude of the contribution given as

$$T_{g'g}^{n'n(new)} = T_{g'g}^{n'n} + (T_{g'g}^{n'n})_{twin}. \quad (170)$$

The new *superfacet* is used in a 3-point rebalance with its neighbors as described above.

Results of the First Moment Rebalance.

In this section we look at the meaning of the rebalance equations for the various cases. This should shed some light on to what the equations are actually doing. In later chapters, we will see how the rebalance impacts the T-matrix in a global sense.

Expectations for cell rebalance. On a rectangular grid, as shown in Figure

19, consider the average angle of scatter, $\bar{\Omega}$, to lie in the upper right quadrant of a facet (F_1), with neighbors F_2 , F_3 , and F_4 as shown.

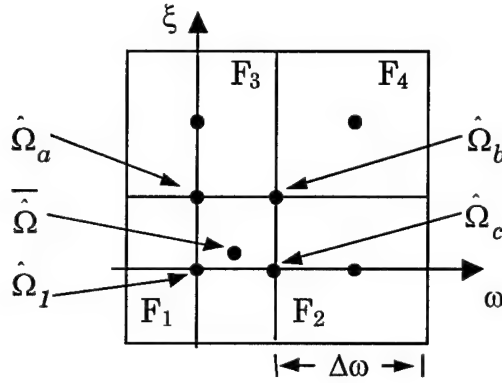


Figure 19. Rebalancing between 4-points.

If $\bar{\Omega}$ were to point in the same direction as the directional ordinate of F_1 , we would expect F_1 to receive one hundred percent of the contribution of the zeroth moment of the scatter, and the neighbors to receive nothing. If $\bar{\Omega} = \hat{\Omega}_a$ directly between F_1 and F_3 as shown in Figure 19, then these two facets should share the zeroth moment while the others receive nothing. Similarly, if $\bar{\Omega} = \hat{\Omega}_c$ directly between F_1 and F_2 as shown in Figure 19, then these two facets should share the zeroth moment while the others receive nothing. Finally, if $\bar{\Omega} = \hat{\Omega}_b$, we'd expect all four facets to share equally in the zeroth moment.

Figure 20 shows what happens as $\bar{\Omega}$ sweeps from $\bar{\Omega} = \hat{\Omega}_1$ to $\bar{\Omega} = \hat{\Omega}_c$. Here $\bar{\Omega}$ lies on the equator ($\xi_1 = \xi_c = 0$) between F_1 and F_2 with no polar component. For $\tilde{\omega}_o = 0$, $\bar{\Omega} = \hat{\Omega}_1$ and no rebalancing takes place. As $\bar{\Omega}$ moves toward $\hat{\Omega}_c$, F_2 's fraction of the zeroth moment increases. The most it

can receive is half the total contribution to the original amount found in F_1 .

In this case F_3 and F_4 receive no contribution.

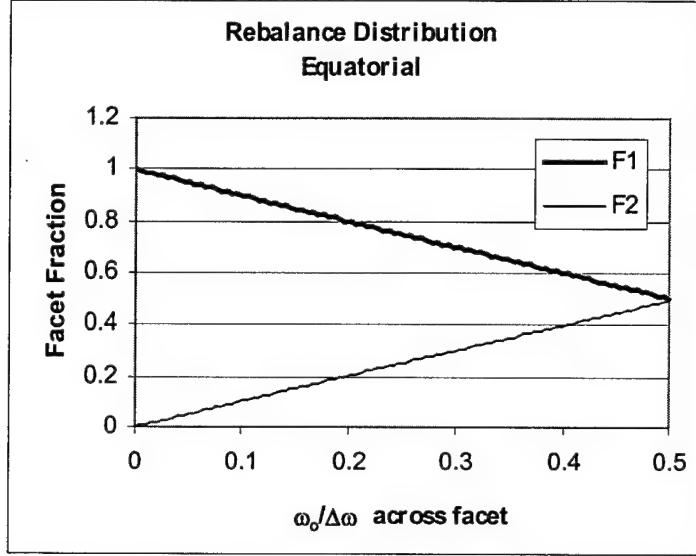


Figure 20. Rebalance fractions between F_1 & F_2 with no polar component.

Care must be exercised when applying flat surface thinking to the curved surface of a sphere. The lines tend to distort from our linear expectation of the flat surface as one moves up the pole. Consider a sphere divided with six latitudinal and twelve longitudinal facets with two polecaps (Figure 6).

That's $6 \times 12 + 2 = 74$ facets of equal solid angle on the unit sphere. Let F_1 's directional ordinate lie on the polar cosine $\xi_1 = 0.243$. The corresponding ordinate for F_3 lies on the polar cosine $\xi_3 = 0.405$. As before, let $\bar{\hat{\Omega}}$ run across the middle of F_1 from $\bar{\hat{\Omega}} = \hat{\Omega}_1$ to $\bar{\hat{\Omega}} = \hat{\Omega}_c$. Then $\bar{\hat{\Omega}}$ has a polar cosine $\xi_o = 0.243$ with $\tilde{\omega}_o \in [0, \Delta\omega / 2]$. The results are shown in Figure 21.

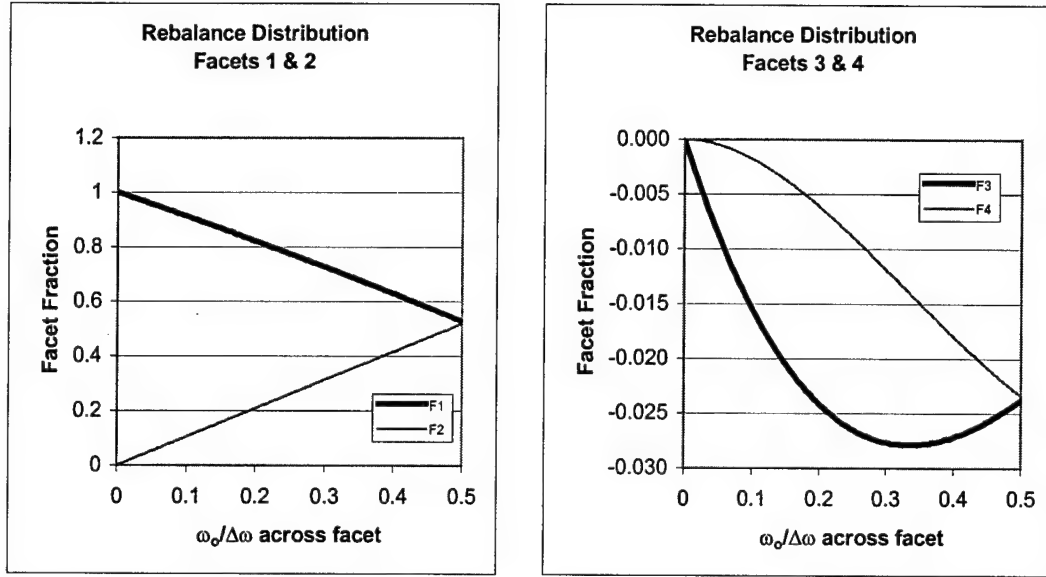


Figure 21. Applying flat thinking to curved surfaces: 4-Point Rebalance.

One can see that there are negative fractions going to F_3 and F_4 , which of course, is a mathematical artifact. We've overstepped the domain of the solution by trying to follow the latitudinal arc between F_1 and F_2 when we can't rebalance past the great circle arc on which both $\hat{\Omega}_1$ and $\hat{\Omega}_2$ lie (see Figure 22).

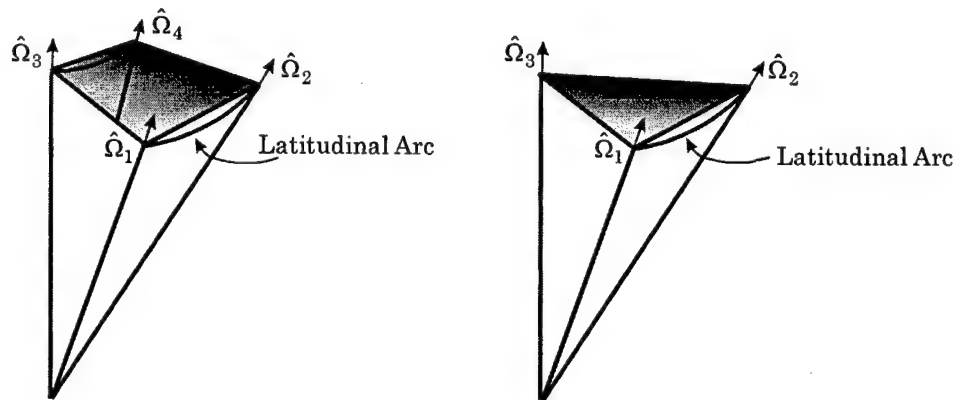


Figure 22. Great circles define the shaded area within which the directional ordinate must lie.

The problem is solved in the following way. When determining the “nearest neighbor” facets, one needs to verify if $\overline{\hat{\Omega}}$ is above or below the great circle arc on which both $\hat{\Omega}_1$ and $\hat{\Omega}_2$ lie. The answer is found from equation (158). If the polar cosine of $\hat{\Omega}_1$ is ξ_1 , and the polar cosine of $\overline{\hat{\Omega}}$ within F_1 is ξ_0 , then the nearest neighbor is determined by comparing $\xi_0 \sqrt{1 - \xi_1^2} \cos\left[\frac{\Delta\omega}{2}\right]$ with $\xi_1 \sqrt{1 - \xi_0^2} \cos\left[\frac{\Delta\omega}{2} - \tilde{\omega}_0\right]$ where, as before, $\tilde{\omega}_0 \in [0, \Delta\omega/2]$. If

$$\xi_0 \sqrt{1 - \xi_1^2} \cos\left[\frac{\Delta\omega}{2}\right] \geq \xi_1 \sqrt{1 - \xi_0^2} \cos\left[\frac{\Delta\omega}{2} - \tilde{\omega}_0\right], \quad (171)$$

then F_3 and F_4 are the neighbors directly above F_1 and F_2 (in the northern hemisphere). If not, then the neighbors lie below F_1 and F_2 .

This same requirement applies for both 3-point and 4-point rebalancing. Using the same 74 facet quadrature described above, the polar cosine of the directional ordinate of F_1 (just below the polecap) is $\xi_1 = 0.905$. Sweeping $\overline{\hat{\Omega}}$ from $\tilde{\omega}_0 = 0$ to $\Delta\omega/2$ with $\xi_0 = 0.95$ across F_1 the rebalance fractions are shown in Figure 23.

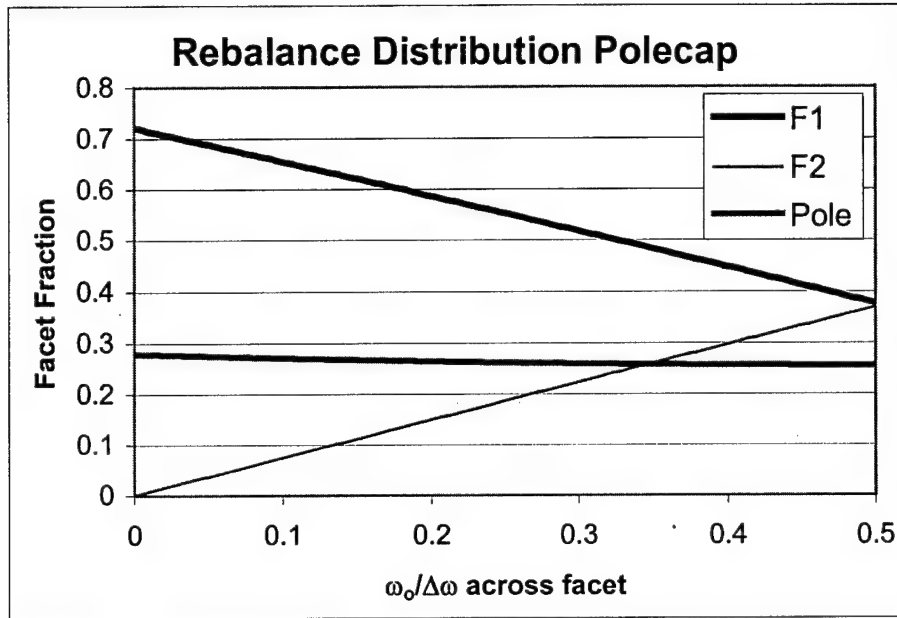


Figure 23. Rebalance at the pole. ($\xi_1 = 0.905$, $\xi_0 = 0.95$)

As expected, for this intermediate polar cosine, the fractions tend to be split 50/50 as $\widehat{\Omega}$ moves across F_1 toward F_2 . Notice that the polecap fraction tends to droop as the sweep tends to $\Delta\omega/2$. This is expected behavior because of the curved surface of the sphere.

General Summary of First Moment Conservation

The process of the rebalancing code is summarized in Algorithm 2.

Algorithm 2. First Angular Momentum Conservation

Set desired facet quadrature, total facets = N .

Set desired group structure, total groups = G .

Calculate directional ordinates, $\hat{\Omega}_n$

Do $g'=1..G$

Do $n'=1..N$

$BalancedT = 0$ Array dimension ($N \times G$)

Read unbalanced $T_{g'g}^{n'n}$ ($g=1..G; n=1..N$)

Read facet average angular scatters, $\hat{\Omega}_{g'g}^{n'n}$ ($g=1..G; n=1..N$)

For poles

Find new direction for antithetic twins:

$$\hat{\Omega}_{new} = \frac{(T_{g'g}^{n'n} \hat{\Omega}_{g'g}^{n'n}) + (T_{g'g}^{n'n} \hat{\Omega}_{g'g}^{n'n})_{twin}}{\|(T_{g'g}^{n'n} \hat{\Omega}_{g'g}^{n'n}) + (T_{g'g}^{n'n} \hat{\Omega}_{g'g}^{n'n})_{twin}\|}$$

Determine new landing facet: $n(new)$.

Calculate magnitude at this direction:

$$T_{g'g}^{n'n(new)} = (T_{g'g}^{n'n}) + (T_{g'g}^{n'n})_{twin}$$

Save values as separate contributors for later rebalance.

For each rectangular facet and *superfacet* contribution

Determine appropriate nearest neighbors

Determine 3-point or 4-point rebalance

Adjust for walks off left or right side of Cartesian map

For appropriate neighbors $i=1..M$ ($M = 3$ or 4)

Determine appropriate portion for self and each neighbor, $s(i)$

$$BalancedT_{g'g}^{n'n_i} = BalancedT_{g'g}^{n'n_i} + s(i)$$

Apply rotational symmetry to $BalancedT_{g'g}^{n'n}$:

For azimuthally symmetric facets $n1$ and $n2$

$$BalancedT_{g'g}^{n'n1} = (BalancedT_{g'g}^{n'n1} + BalancedT_{g'g}^{n'n2}) / 2$$

$$BalancedT_{g'g}^{n'n2} = BalancedT_{g'g}^{n'n1}$$

Write $BalancedT_{g'g}^{n'n}$ for ($g=1..G; n=1..N$)

EndDo: g'

EndDo: n

The algorithm includes an adjustment for azimuthal symmetry. Because the calculation of the facet contributions is performed with MC draws, calculation of scatter azimuthally to the left or right of the incident facet may differ dependent on the number of draws taken. Once facet rebalance has taken place, the azimuthally symmetric facets (now centered on their directional ordinates) are simply summed with half the total going to each facet.

To conserve the first angular moment of the scatter, we've developed a method that tracks the average angle of the scatter within the cell and then rebalances the result to the appropriate nearest neighbors. We would expect this to improve our solution to transport problems that are diffusion-like in nature. While the transport code we use, TETRAN, is unable to perform diffusion like problems, later we will see the effects of rebalancing on the T-matrix itself, and then look at how rebalancing impacts the solution of the transport equation for fast neutron problems.

8. Code Development, Capabilities and Operation

The creation and use of a T-matrix library is a multi-step process. It begins with the ENDF data and ends with results from a transport code that uses the T-matrix library. Such results are often compared among codes for validation or benchmarking. In this chapter we'll briefly look at the validation process, discuss the libraries necessary to create both the T-Scat library and the libraries used to generate the spherical harmonics cross-sections. We'll then take a close look at the steps required to get the data generated from T-Scat into a form that the transport code can read.

From Continuous to Discrete: The Path for Benchmarking.

To determine the validity, and often accuracy of a discrete ordinates, S_N , code, programmers will typically compare results of test problems with Monte Carlo transport techniques like MCNP^{7, 24}. Often, the argument is that MC methods do not suffer from the unknown effects of angular, group and spatial discretization found in S_N methods.

There are, inevitably, artifacts from the discretization schemes employed in S_N methods, just as there are artifacts resultant from variance reduction techniques employed by Monte Carlo methods. Because the two methods are so very different at their core, it is unreasonable to assume that an S_N method would converge exactly to a Monte Carlo solution. The S_N solution

may approach the MC solution, giving the user a sense of well being, but was the convergence primarily because of a reduction in the spatial grid, angular quadrature, group structure or particular combination of the three?

We propose a methodology to examine such questions, and in so doing introduce a new type of transport code, developed at AFIT, that takes advantage of strictly positive T-matrix data.

The Triad of Discretization

One path from a purely continuous method, like MCNP, to a discrete ordinates method, like TETRAN⁷ (used in this research), is represented in Table 2.

Table 2. Discretization path from MCNP to Discrete Ordinates.

Transport Code	Space	Angle	Energy
MCNP	C	C	C
MCNP-MG	C	C	D
MCSN	C	D	D
Discrete Ordinates	D	D	D
C = Continuous; D = Discretized			

As discussed earlier, MCNP is a Monte Carlo Transport code developed by LANL. It has an option to use standard Legendre polynomial based multi-

group libraries, and calls this option MCNP-MG. MCSN is a new transport code developed at AFIT²⁵.

The MCSN method uses a continuous Monte Carlo approach to transport the particles in space. The transport, however, is discretized in energy by group, g , and in angle by facet, n , represented by the directional ordinate, $\hat{\Omega}_n$. For each material, incident facet, n' , and group, g' , MCSN uses the T-matrix to create a cumulative distribution function of scattered facet and group, $F(n, g; mat, n', g')$. Given the material and an incident facet and group, MCSN inverts $F(n, g; mat, n', g')$ to find the scattered facet and group. It then transports the scattered particle again in direction $\hat{\Omega}_n$ with a MC sampling continuous in space.

This research employs Tetran as the discrete ordinates method of choice. This discrete ordinates code runs on geometries that are spatially discretized with unstructured tetrahedral meshes. It can use either standard Legendre polynomial based, multigroup libraries to generate T-matrices internally (potentially negative) or it can read T-matrices directly calculated from T-Scat (guaranteed non-negative).

We emphasize here that the creation of the non-negative T-matrix has made MCSN possible. When sampling groups and ordinates, the scattering cross sections constitute a discrete distribution, $f(n, g)$. It is meaningless to have negative values as would be created from a spherical harmonic approximation. If they are included, the cumulative distribution, $F(n, g)$, is

not monotonic and cannot be inverted to find g and n . We can now see directly the effects of spatial discretization by comparing TETTRAN results to MCSN. We can see directly the effects of angular discretization by comparing results between MCSN and MCNP-MG. Finally, group discretization effects can be examined by comparing MCNP-MG with MCNP. While the exploration of discretization effects in various transport codes is not the thrust of this study, this research has now made such exploration possible. In subsequent chapters, we present some early results comparing such methods. It is certainly an area for greater research.

Cross Section Libraries: Getting ENDF data into the transport code.

A number of libraries have combined experimental observations with theoretical models to achieve a reasonable database of the collision process. Many of these libraries are available on the web^{26,27}. The data prepared for MCNP comes from the Evaluated Nuclear Data Files or ENDF. The latest release of this library is ENDF/B-VI²⁸. All our calculations begin with this cross-section library. It should be noted that the accuracy of these cross sections can vary considerably. It is important therefore, that for comparisons between transport methods, such methods use or originate from, whenever possible, the same cross section library.

NJOY: Creating Continuous and Multi-Group Data.

There are also a number of codes that may be used to convert ENDF data to a form used by different transport methods. Again, because we will later compare with MCNP, we use a code called NJOY, developed by LANL, to get us one step closer to the libraries we need. NJOY contains a number of subprograms that read in the ENDF data and convert it to either continuous energy cross section libraries (as used by MCNP) or to create the Legendre coefficients used to calculate the multi-group spherical harmonics. The continuous energy format is known as an ACE file. The ACE format is read by MCNP to perform transport and also by T-Scat to create the T-matrices. The output form of the multi-group data is known as a MATXS library. Another code developed by LANL, TRANSX²⁹, reads the MATXS library and

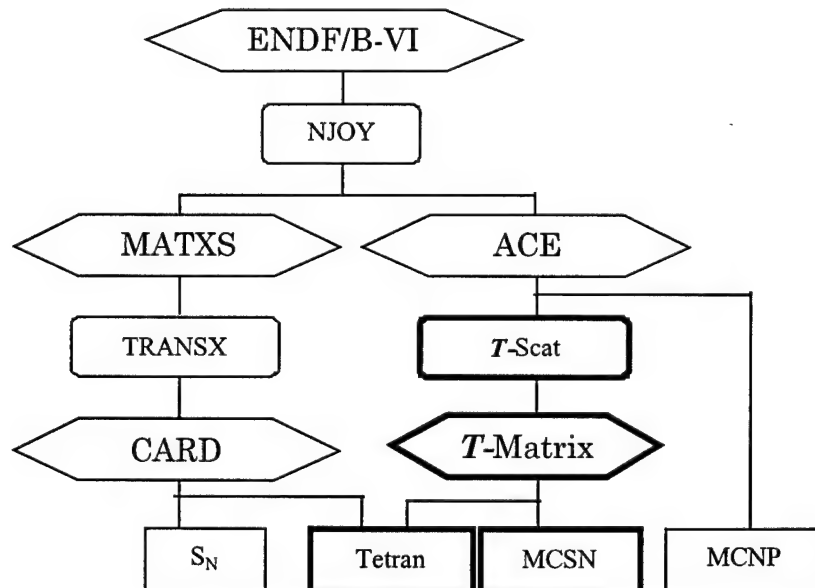


Figure 24. Flow of the Cross-Section Data to the Transport Codes

creates a new library (CARD) that can be used by standard S_N transport codes (using spherical harmonics to approximate the scattering source).

Figure 24 depicts the flow of cross-section data through the various processes. The codes that perform the processing are shown in the rounded boxes. The darkened boxes represent those codes and libraries created at AFIT.

Group Structures

The NJOY processing system allows the user to select a number of predetermined group structures. In this research we use two, LANL-30 and VITAMIN-J. Both structures can be found in the appendix. The LANL-30 ranges from 1.39E-04 eV to 17.0 MeV and contains 30 groups. The group size is defined using the quantity called lethargy, u , where

$$u(E) = \ln \frac{E_0}{E}. \quad (172)$$

When using lethargy to describe the size of the group, we define the group lethargy as

$$\Delta u_g \equiv \ln \frac{E_0}{E_g} - \ln \frac{E_0}{E_{g-1}} = \ln \frac{E_{g-1}}{E_g}. \quad (173)$$

A group size of *one lethargy* implies that

$$\Delta u_g = \ln \frac{E_{g-1}}{E_g} = 1, \quad (174)$$

or

$$E_g = \frac{1}{e} E_{g-1}. \quad (175)$$

For the LANL-30 group structure (Figure 25), the group size at low energy is one lethargy and at higher energies $\frac{1}{2}$ and $\frac{1}{4}$ lethargy groups are used. It is essentially a survey group structure, allowing the researcher to get a rough idea of the problem at hand. This group was selected because it is the group structure of MATXS-10, a standard MATXS library used to develop the Legendre coefficients for transport comparisons.

The Vitamin-J structure is an evolution of an older library used for shielding applications. The energy bounds range from 1.0E-05 eV to 19.64 MeV with a total of 175 energy groups.

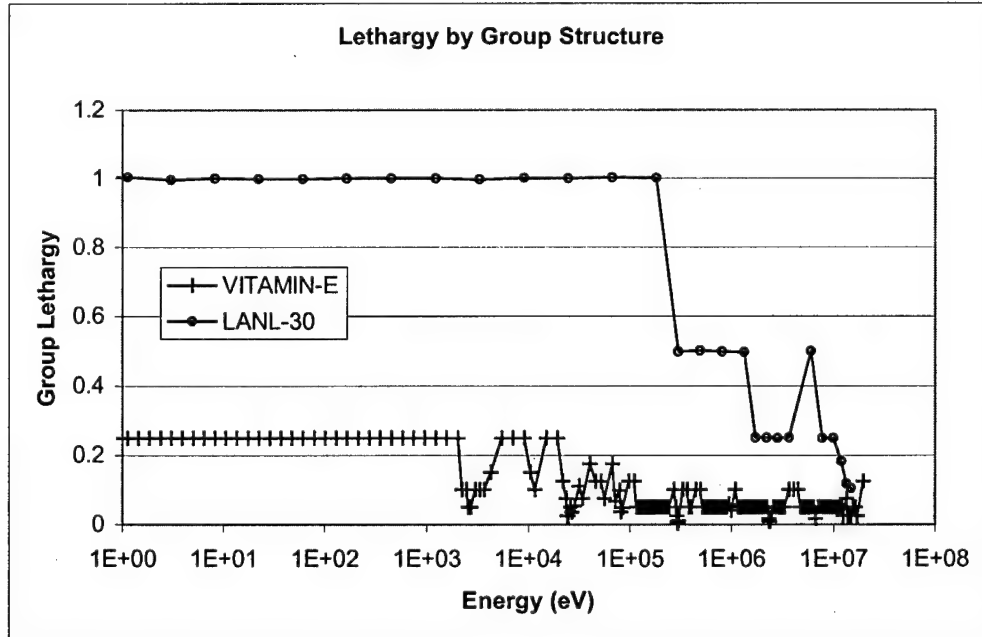


Figure 25 Group size in lethargy for selected group structures

This group was selected to help test the anisotropy that a finer group structure can create. Further, Tetran was developed to employ the EC method, ideal for shielding applications. Taking advantage of this synergy, some deep penetration problems are examined as part of this research. Of course, any group structure can be used with any of the codes, including T-Scat.

T-Scat's Current Capabilities

Here we outline the steps required to get from the ACE format to a library that is used by the transport code TETRAN. There are three basic steps, each representing separate codes developed for this research.

1. T-Scat: Performs MC integration to calculate the T-matrix.
Calculates total cross-section and determines first angular moments for each scattered facet and group.
2. T-Balancer: Rebalances the uncompressed T-matrix to conserve the first angular moments of the scatter.
3. T-Mixer: Decompresses and combines the libraries for the problem at hand (group material and mix specific). Converts microscopic data to macroscopic data.

Calculating the T-matrix with T-Scat.

As discussed earlier, T-Scat evaluates the T-matrix

$$T_{g'g}^{n'n} \approx \frac{M_{g,n}}{M} \frac{\sum_{i=1}^M \left[\sigma^s(E'_i) W(E'_i) \chi_g^E(\tilde{E}_i) \chi_n^{\hat{\Omega}}(\tilde{\Omega}_i) \right]}{\sum_{i=1}^{M_{g,n}} W(E'_i)}, \quad (176)$$

by reading microscopic cross-section data directly from an ACE file and computing the T-matrix for the given group and facet structure.

Scattering Laws. The currently supported scattering laws (following the MCNP formalism) are:

1. Elastic.
2. Discrete level inelastic.
3. Continuum: evaporation spectrum.

It would be straightforward to incorporate the other scattering laws including multiplying (n,2n) and fission reactions. T-Scat is both downscatter and upscatter capable. For a complete list of such laws see Appendix B.

Symmetries Applied. Because of the quadrature used, one can take advantage of the available symmetry in the scattering and reduce the number of calculations that need to be performed¹³. For each incident group, only the incident facets in the northern hemisphere along the same meridian need be calculated. For each incident facet we tally to the appropriate scattered groups and facets on the entire sphere. The other incident facet calculations are either reflections, rotations, or both of this same calculation.

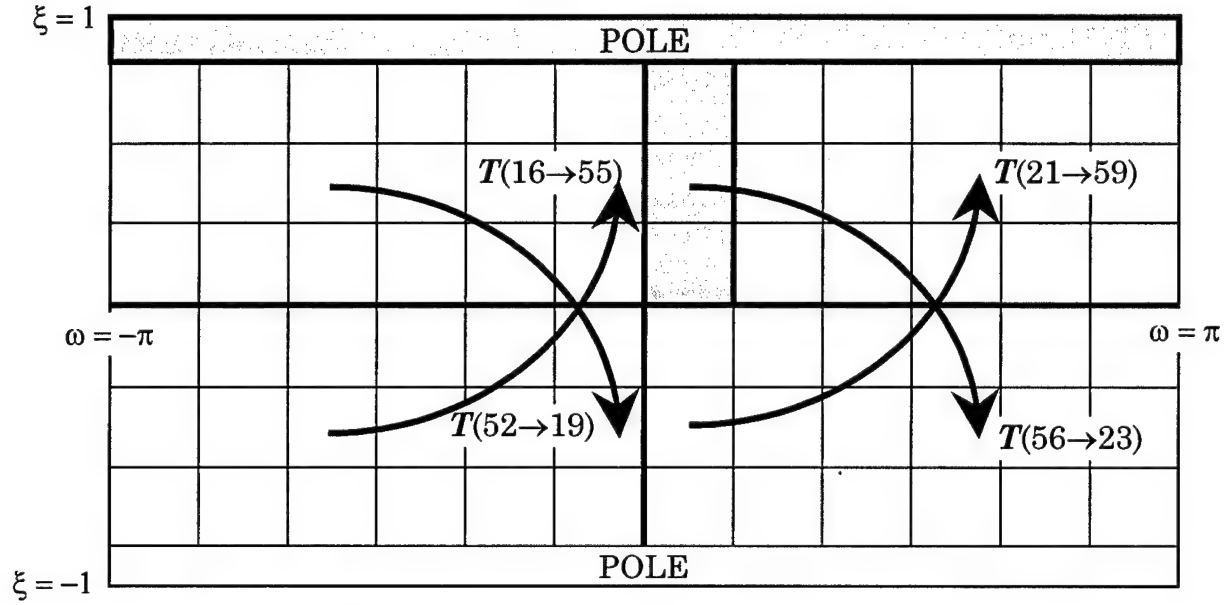


Figure 26. 74 Facet Structure. All incident facets are rotations or reflections of the shaded regions.

Figure 26 shows the incident facets for which T-Scat calculates. The arrow illustrates a $T(56 \rightarrow 23)$ transfer for a given $g' \rightarrow g$ (counting facets left to right from bottom to top). This same scatter is shown on the unit sphere in Figure 27. Such a scatter is the same as $T(21 \rightarrow 59)$ by reflection, $T(52 \rightarrow 19)$ by rotation, and $T(16 \rightarrow 55)$ by reflection and rotation (as shown). The data is stored in this compressed form. It is the job of another code, T-Mixer, to decompress the data and prepare it for transport.

Other Outputs. Also output during this step are the total group cross-section and the first moment of scatter for each facet. The total cross section is integrated directly from the continuous energy ACE file using the same energy weight structure as the T -matrix. The Monte Carlo integration of the total cross section takes the form

$$\sigma_g = \frac{\sum_{i=1}^N \sigma(E_i) W_g(E_i)}{\sum_{i=1}^N W_g(E_i)}, \quad (177)$$

Because the average scatter data is a set of three values

$(\bar{\Omega}_n = (\mu_n, \eta_n, \xi_n))$ for each $T_{g'g}^{n'n}$, the data file is somewhat larger than the

T-matrix file for $T_{g'g}^{n'n}$ alone, but once the rebalance is performed, the average scatter data is no longer required.

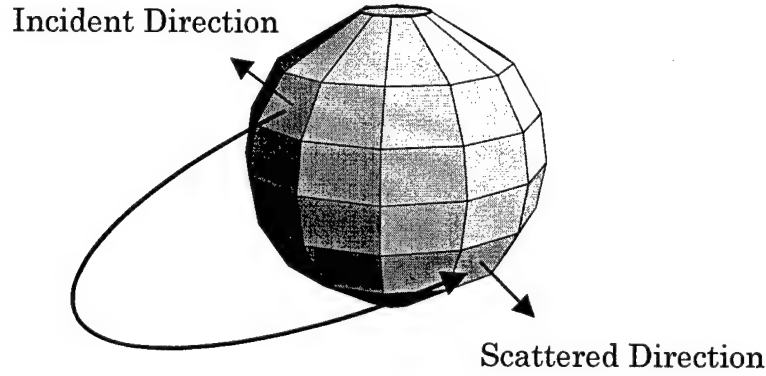


Figure 27. $T(56 \rightarrow 23)$ facet transfer on the sphere.

Rebalance to Conserve the First Angular Momentum

The next step is to rebalance the T-matrix. For each $T_{g'g}^{n'n}$, the rebalance program determines the appropriate nearest neighbors and distributes the

zeroth moment appropriately conserving the first moment input. The output is still in compressed form (only for the specific incident facets calculated).

T-Balancer performs the following tasks:

1. Given the group and quadrature structure determine facet directional ordinates.
2. Verify that all input first moments are found within the appropriate facet. This is done as an error check on the input.
3. Determine facet nearest neighbors (as discussed earlier).
4. Apply 4-point or 3-point rebalance as appropriate.
5. Assign rotational symmetry. A facet transfer azimuthally to the right should be identical to the transfer to the left. Statistically these numbers converge with increasing draws.
6. Write the balanced T-matrix.

The rebalance code run time is orders of magnitude shorter than the T-Scat code run time to calculate the T-matrix. The entire program could be implemented as a sub-routine of the main program, T-Scat.

Prepare Library for the Transport Code Tetran

T-Mixer prepares the T-matrix data for use by Tetran. The way Tetran reads in the T-matrix dictates the data structure produced by the mixer. It should be noted that other transport codes may have other requirements. Hence, the T-matrix libraries are only dependent on the angular quadrature

and group structure used. It is the mixer's job to prepare the data for the problem specific transport run.

Tetran reads in the T-matrix data in the following way. First, $T_{1,1}^{n'n}$ is read for all facets and all materials in the problem. The code is run until the group 1 angular flux, $\psi_{1,n}$ is found for all incident angles. Once known, this flux is used to calculate its contribution to the scattered source for all down scattered energy groups by reading $T_{1,g}^{n'n}$ for all materials and groups, $g > 1$. TETRAN then proceeds to the next group and performs the same calculation sequence, summing up the contributions from all previous calculations to get the total scattered source for the present group. The code sweeps down the group structure in this way, until the final group is calculated.

TETRAN does not require the T-matrix to be positive. It is the spatial quadrature techniques used by TETRAN that dictate requirements for source positivity. TETRAN employs two types of spatial quadrature--linear characteristic (LC)³⁰, and exponential characteristic (EC)⁷. The LC method does not require that the calculated sources be positive. The EC method, however, does require non-negative sources. Good for deep penetration problems, the EC method will fail if a negative source is calculated.

The T-matrix, built by spherical harmonics, is given as

$$T_{g'g}^{n'n} = w(\hat{\Omega}_n) \sum_{l=0}^L \sigma_{l,g'g}^s \sum_{m=-l}^l Y_{lm}^*(\hat{\Omega}_n) Y_{lm}(\hat{\Omega}_{n'}), \quad (178)$$

which, in TETRAN, is calculated as required during the code run. The chapters that follow will give a direct comparison between the T-matrix as built by T-Scat with those built from spherical harmonics. We will also present comparisons of transport code runs using both the LC and EC spatial quadratures.

The next step is performed by the code T-Mixer. T-Mixer prepares the T-matrix for transport use. If the transport problem looks at multiple materials (e.g., water-iron-water) then the T-Scat matrix for water has to be shuffled with the T-Scat matrix for iron as required by the transport problem. Further, as was described by the section "Select the Collision Nuclide" on page 49, the T-matrix for water (H₂O) may have already been generated by T-Scat directly or must be mixed from the separate matrices of hydrogen and oxygen. Finally the ordinate structure of the T-matrix must be decompressed to allow for direct reading of the ordinate to ordinate transfers by the transport code

The mixing code, T-Mixer, first combines T-matrix data for mixed materials such as H₂O (as required). When there are M different nuclides forming the material then the microscopic cross sections, \tilde{T}_i , are combined as

$$\tilde{T}_{tot} = \sum_{i=1}^M \tilde{T}_i f_i, \quad (179)$$

where f_i is the atom fraction of nuclide i . For H₂O this is

$$\tilde{T}_{H_2O} = 2\tilde{T}_H + \tilde{T}_O. \quad (180)$$

The \tilde{T} -matrices are then converted from microscopic data (barns) to macroscopic (cm^{-1}) data based on the density and isotopes of the material. If \tilde{T}_{tot} is the microscopic T-matrix calculated from equation (179), then the total macroscopic T-matrix, T_{tot} is found as

$$T_{tot} = \tilde{T}_{tot} \frac{N_{Av}\rho}{\sum_{i=1}^M A_i f_i} = N_{Av}\rho \frac{\sum_{i=1}^M T_i f_i}{\sum_{i=1}^M A_i f_i}, \quad (181)$$

where, N_{Av} is Avagadro's number ($0.60221367 \text{ cm}^2/\text{barn-mol}$), ρ is the density (g/cm^3) of the material, and A_i the atomic weight (g/mol) of nuclide i in the material. For water, this is

$$T_{H_2O} = N_{Av}\rho \frac{\sum_{i=1}^M \tilde{T}_i f_i}{\sum_{i=1}^M A_i f_i} = (0.6022)(1.0) \frac{2\tilde{T}_H + \tilde{T}_O}{2(0.999170) + 15.85316}. \quad (182)$$

The T-Mixer then selects, reflects and rotates the T-matrix, as appropriate, for each incident facet. The data is then written to file to be read in by TETRAN. The transport code developed at AFIT, MCSN, reads the data in the same way, so no separate calculation is required for that code.

We are now in a position to evaluate the new non-negative scattering matrix on two fronts. First, how does the T-matrix, generated with the MC

facet method compare to what we expect from the physics and to its well-established spherical harmonic counterpart? Second, how do transport codes perform using this new T-matrix particularly in the presence of anisotropic scattering? The following chapters answer these questions.

9. Calculations: Investigations of the *T*-Matrix

There are two primary results of this effort. The first is the creation of the T-matrix for various materials and compounds using the Monte Carlo facet method and subsequent rebalance. The second is the performance improvement of transport codes using this T-matrix data. This chapter examines the first of these results.

In this chapter, we'll develop an understanding of how to read the T-matrix data. As was the case when we examined $\sigma(\mu)$ in one dimension, we'll see that the structure of the scattering matrix affords insight to the physics of the scatter. We'll show that the Monte Carlo facet method creates a non-negative T-matrix that directly represents the physics of the scatter. Next, the convergence and run time of the T-Scat integrator is presented. Following this is a comparison between strictly positive T-matrix data created by T-Scat, and data created by the spherical harmonic method. This will demonstrate the superior performance of the MC facet method, particularly for anisotropic scattering. The next section investigates the specific angular support failings of ordinate-to-ordinate methods, and discusses how the MC facet method has no such failings. Finally, we'll demonstrate the effects of angular rebalancing on the T-matrix data.

Visualizing the Scattering Physics—An Introduction to the Graphics

This section gives a quick sketch of the various types of graphics used in this research to analyze the T -matrix data. The goal is to see what the physics is telling us and verify that what we're seeing makes sense.

As discussed earlier, a monoenergetic particle travels with energy E' , in direction $\hat{\Omega}'$ and strikes a nuclide. After the collision the particle has a scattered energy, E , and direction $\hat{\Omega}$. Here we assume azimuthal symmetry in the scatter so that the new direction, $\hat{\Omega}$, is found in some cone around the incident direction, $\hat{\Omega}'$ (see Figure 28)

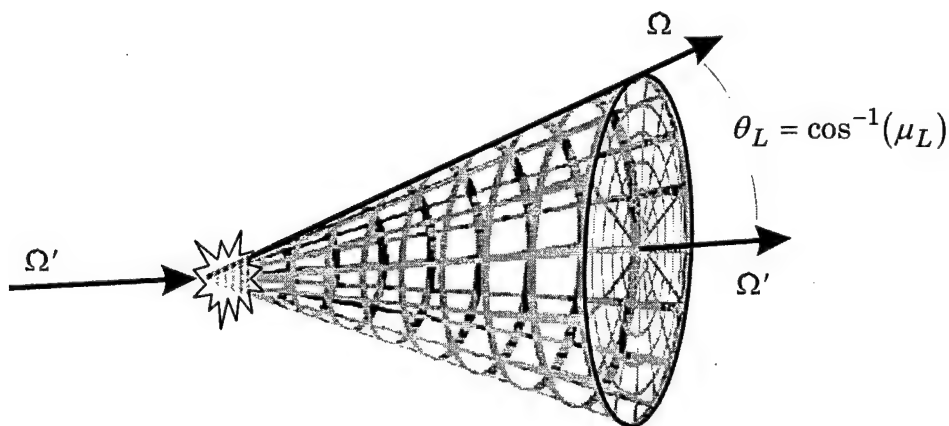


Figure 28. Scattering Cone After Collision.

Placing this geometry on the sphere, the cone is represented by a circle on the surface of the sphere indicating the possible new direction of the scattered particle (Figure 29). Folding the sphere out like a map of the earth, the circle, as expected, becomes distorted.

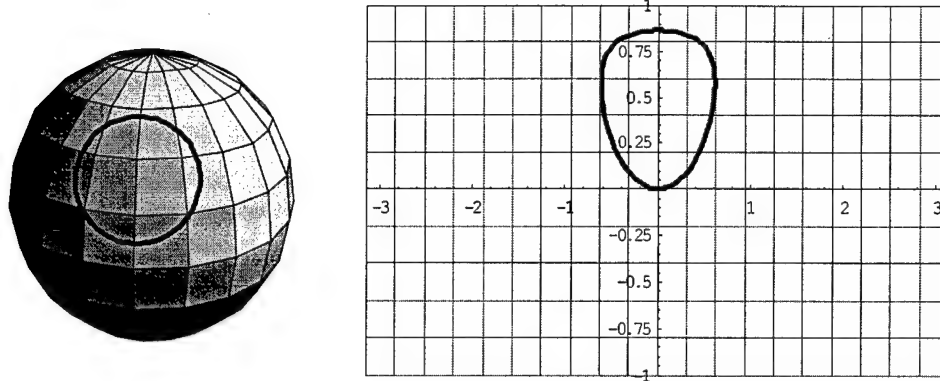


Figure 29. Scattering circle of the sphere on a Cartesian map.

For elastic scatter, the greater the loss in energy the greater the scattering angle, θ_L , where $\mu_L = \cos(\theta_L)$. Figure 30 shows the curves on the Cartesian map corresponding to a progressive increase in θ_L and greater energy loss. The scattering to the lower energies becomes almost square-like in outline.

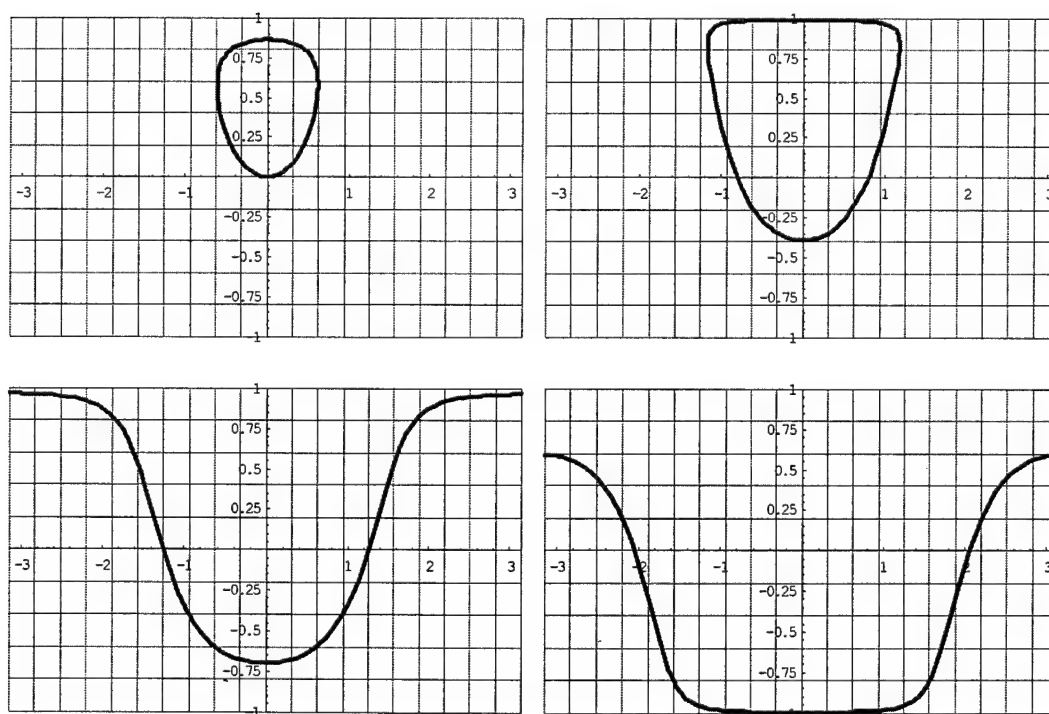


Figure 30. Progressive increases in scattering angle on the Cartesian grid.

This is important to recognize when examining scatter to lower groups on Cartesian maps, as discussed below.

Of course, the scatter is not at a set angle, but has a probability distribution $f(\mu_c, E')$. So the line above is really the peak of a distribution that falls off to either side. Further, we're not considering particles traveling within a single direction, $\hat{\Omega}'$, but rather isotropically across an incident facet, $\Delta\Omega_n$. Finally, the real transfer being considered is not mono-energetic but multigroup. This, *en masse*, tends to spread the curves above. By accounting for the probability distribution with a third axis *perpendicular* to the Cartesian map, a terrain is created that illustrates the probability of scatter. If this is done on a group-to-group basis, the data of the third axis is found directly from the T-matrix as $T_{g'g}^{n'n}$.

As an example, we examine the scattering cross section of hydrogen.

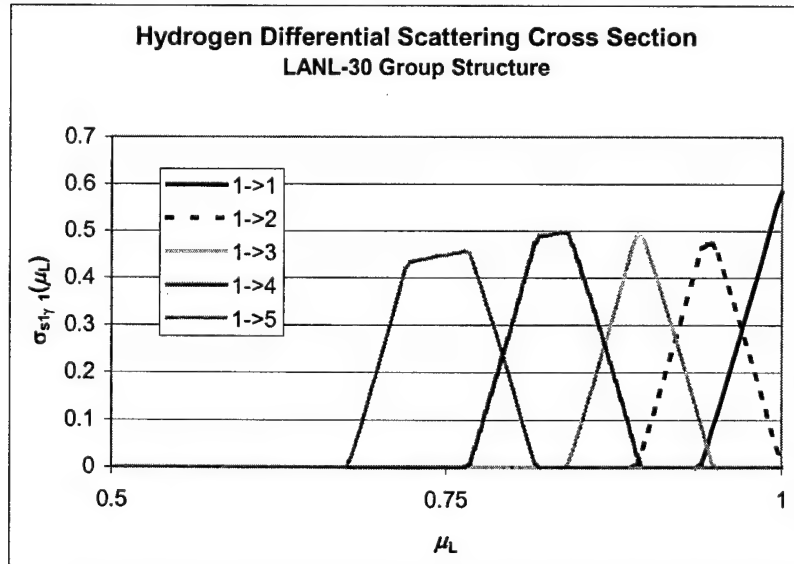


Figure 31. Group-to-group differential scattering cross section of hydrogen as a function of the lab frame scattering angle.

In Figure 31, the differential scattering cross section as a function of lab angle is shown. These were generated with T-Scat where the incident neutron is traveling in group 1 of the LANL-30 group structure. The sphere was divided into 500 latitudinal facets. Only a handful of the facets are ever reached in the first five groups (note scale).

Looking at the within group scatter ($1 \rightarrow 1$; 15-17 MeV), it is highly forward peaked. That is for within group scatter at high energy, neutrons tend to continue in their original direction of travel. Placing this distribution on a scatter plot like the Cartesian map of Figure 29 and plotting in three dimensions, we would expect a cone to appear peaked at the center of the grid and falling off to the sides. The same is true of a facet transfer. In the facet quadrature, particles traveling isotropically within the facet tend to stay within the facet after a ($1 \rightarrow 1$) collision. The scattered distribution is also a cone in the center of the Cartesian grid.

Hydrogen Within Group Scatter

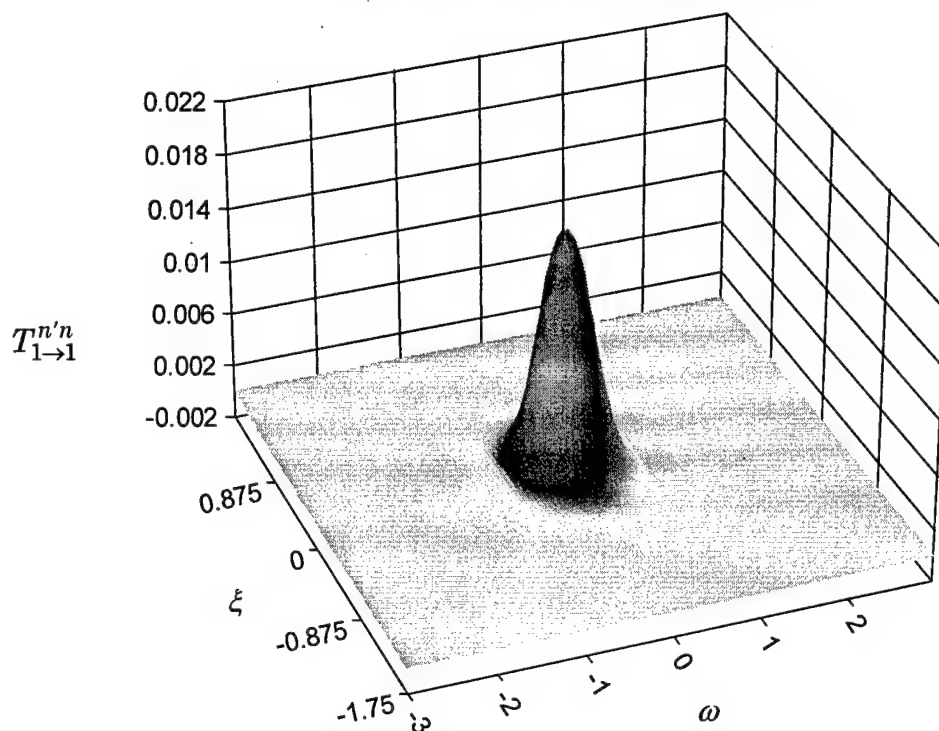


Figure 32. Three dimensional look at within group scatter of ^1H on the Cartesian grid for a 74 facet quadrature.

Figure 32 was created from T-matrix data where the T values are centered within each facet, $\Delta\Omega_n$ at $\hat{\Omega}_n$. The T-matrix facet structure is the 74 facet Cartesian grid described earlier. The graphing routine, TableCurve 3D³¹, performed a bi-quadratic order 2/2 spline interpolation of the T-matrix data. While the interpolation may swing slightly negative, the data is strictly non-negative. The raw facet values can be seen by looking at a bar chart of the data given above (Figure 33).

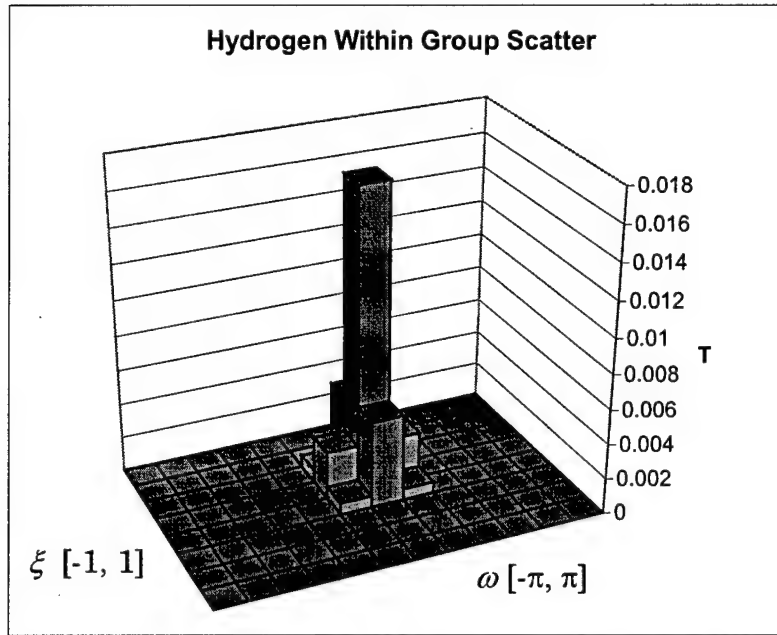


Figure 33. Hydrogen within group scatter showing the explicit facet values of the T-matrix (8 x 12: 74 facets).

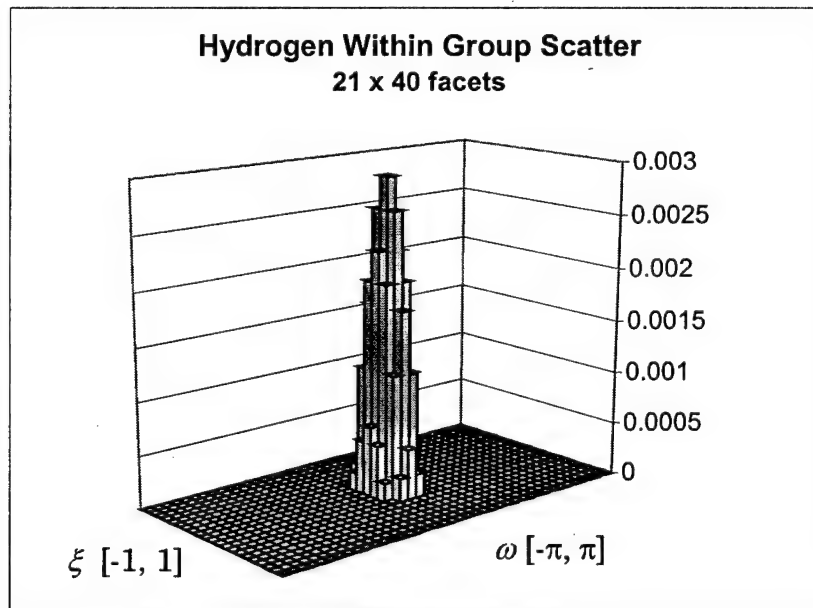


Figure 34. Hydrogen within group scatter showing the explicit facet values of the T-matrix (21 x 40: 762 facets).

It is also possible to look at the data explicitly in three dimensions using spherical coordinates $[r, \omega, \cos^{-1}(\xi)]$. The angular coordinates are the facet

ordinates and the T-matrix value provides the r value. The result is a sharply forward peaked pattern. The most probable direction of scatter is forward peaked with no chance of back scatter. Of course, for a stationary nuclide, elastic back scatter of hydrogen in the lab frame is not possible.

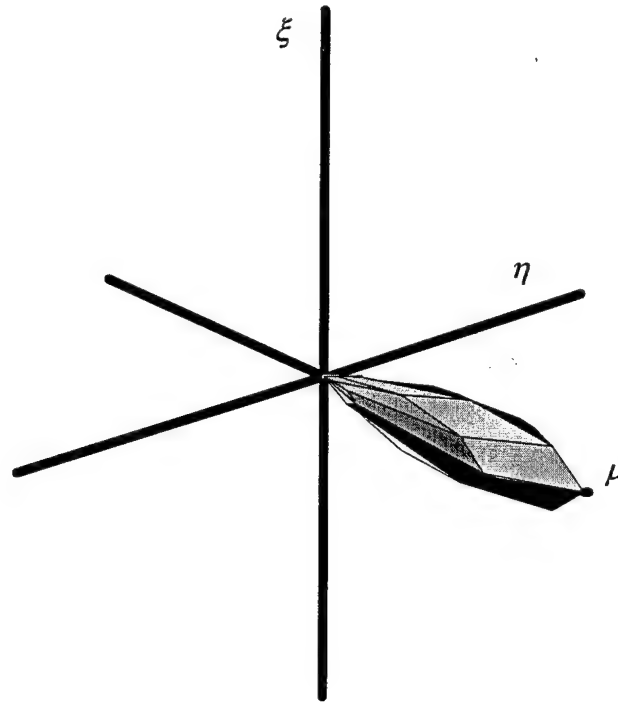


Figure 35. 3-Dimensional representation of within group scatter for hydrogen using the first group of the LANL-30 structure).

The Cartesian grid quadrature allows the data above to be plotted directly using Mathematica. The directional ordinates of the standard level symmetric quadrature (used with spherical harmonic expansion), however, makes such plotting more difficult. To facilitate comparison between the two methods, we draw the data points directly with rays extending from the origin. In this way, the individual data values of Figure 35 are now plotted

three dimensionally in Figure 36. When using illustrations like Figure 36 to present spherical harmonic data negative values are set to zero.

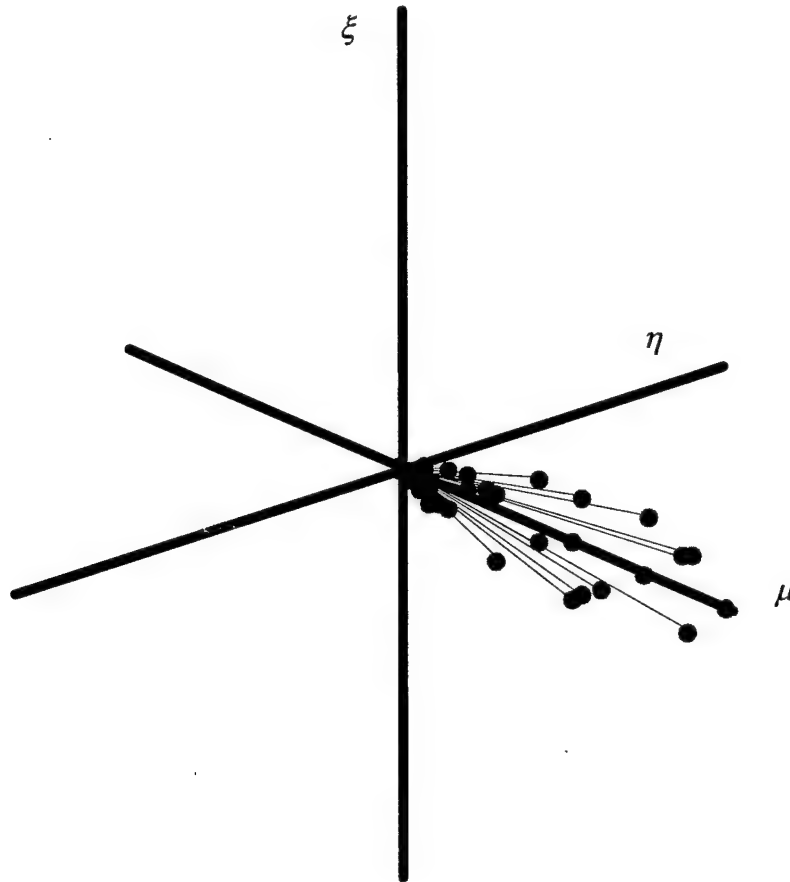


Figure 36. Explicit representation of T-matrix data as scatter points

The graphics shown above will be used extensively in the rest of this dissertation. These plots will be used to help illustrate a number of the advantages of the MC facet method T-matrix. In the sections below, we will answer the following questions:

- Is the physics of the scatter being maintained?
- Does the code converge as expected in a reasonable amount of time?
- How does the MC facet method compare to spherical harmonics?

- Is within group scatter and next group scatter guaranteed?
- Are groups skipped?
- What are the effects of angular rebalance?

In answering these questions we'll find the MC facet method superior to its counterparts in a number of important ways.

Visualizing the physics of group-to-group scatter.

Figure 31 shows the group-to-group scatter of hydrogen in 1-D. Such plots are common in the literature^{5,32}. In this section, we expand the standard analysis to examine the group-to-group T-matrix transfers created by the MC facet method.

As shown in Figure 30, the group structure directly determines the allowed angle of scatter. Combining this type of contour plot with the group-to-group scattering distribution of Figure 31, the MC facet method demonstrates the same behavior. Such a contour plot is shown in Figure 37. As the scattered neutrons lose more and more energy they scatter further and further away from the incident direction.

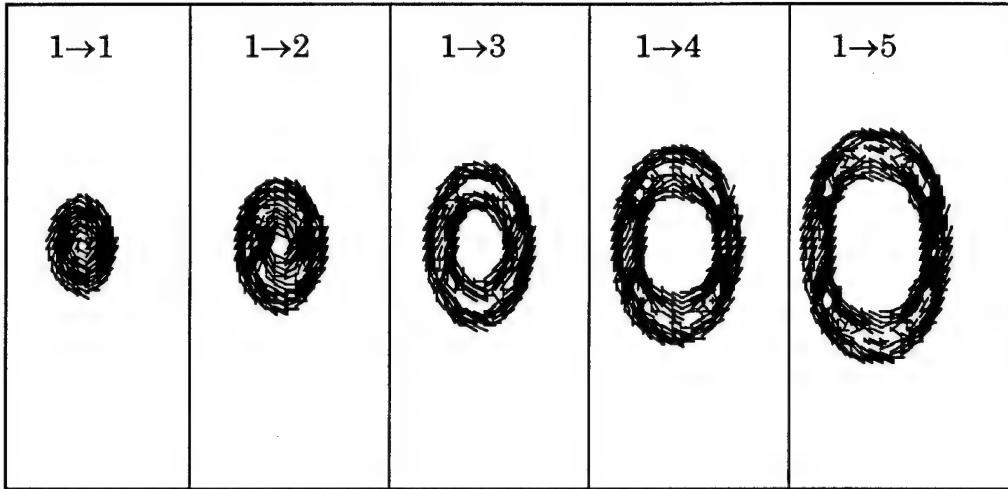


Figure 37. Cartesian contour of the first five scatter groups of hydrogen.

The plots we've shown to this point have been for hydrogen. Hydrogen is perhaps the easiest nuclide to model because its scattering is strictly elastic (for the collisions of interest). It is perhaps the most difficult nuclide to model *correctly* because of its sharply anisotropic behavior. In the center-of-mass (CM) frame, hydrogen's scattering distribution as a function of incident energy, $f(E', \mu_{cm})$, is essentially isotropic. Hydrogen's anisotropy comes from converting the CM scatter, μ_{cm} , to lab frame scatter, μ_L ³². For heavier nuclei, isotropic scattering in the CM frame corresponds to isotropic scatter in the lab frame. Anisotropy in the lab frame, for heavier nuclei results from anisotropic scattering distribution functions, $f(E', \mu_{cm})$, which tend to be forward peaked at high energies. Inelastic scattering levels and the group structure used introduce other anisotropic behavior.

As an example of heavier nuclei, consider oxygen (¹⁶O). This nuclide has 38 different inelastic levels that must be included in the physics model. Each

level has a corresponding Q -value, for ^{16}O ranging between 6.05 and 18.55 MeV. Because of the kinematics involved, neutrons striking oxygen at these energies may have two different scattered energies for a given scatter angle, μ_L . The scattered energies are

$$E(E', \mu_L)_{\pm} = \frac{E'}{(A+1)^2} \left\{ \mu_L \pm \left[\gamma^2(E') - 1 + \mu_L^2 \right]^{1/2} \right\}^2, \quad (183)$$

where

$$\gamma(E') = A \left(1 + \frac{A+1}{A} \frac{Q_i}{E'} \right)^{1/2}, \quad (184)$$

and Q_i is the excitation energy for the considered inelastic level. A similar relation for the incident energy is

$$E'(E, \mu_L) = \frac{E}{(A-1)^2} \left\{ \frac{A^2 - 1 - A(A-1)Q_i / E}{\left[A^2 - 1 - A(A-1)Q_i / E + \mu_L^2 \right]^{1/2} + \mu_L} \right\}^2. \quad (185)$$

To illustrate these scattering kinematics, the relation between incident and scattered energy at given μ_L values is plotted in Figure 38. Clearly, the finer the group structure used, the more confined the allowed range of μ_L and the more anisotropic the behavior of the group-to-group scatter.

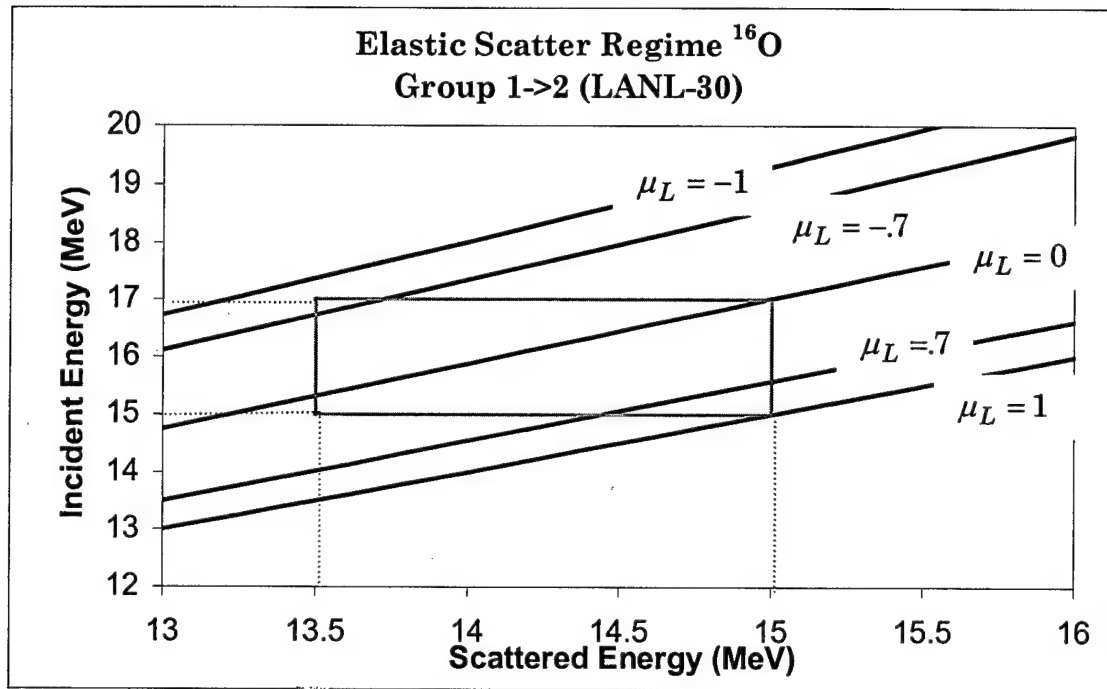


Figure 38. Kinematics for the group 1→2 scatter of ^{16}O .

The interplay between the scattering probability distribution function, $f(E', \mu_c)$, the atomic weight of the target nuclide, and the group structure used, must be considered when examining anisotropic behavior. Figure 39 shows the group-to-group T-matrices for the scatter from the first group (15-17 MeV) to the first four groups of the LANL-30 group structure.

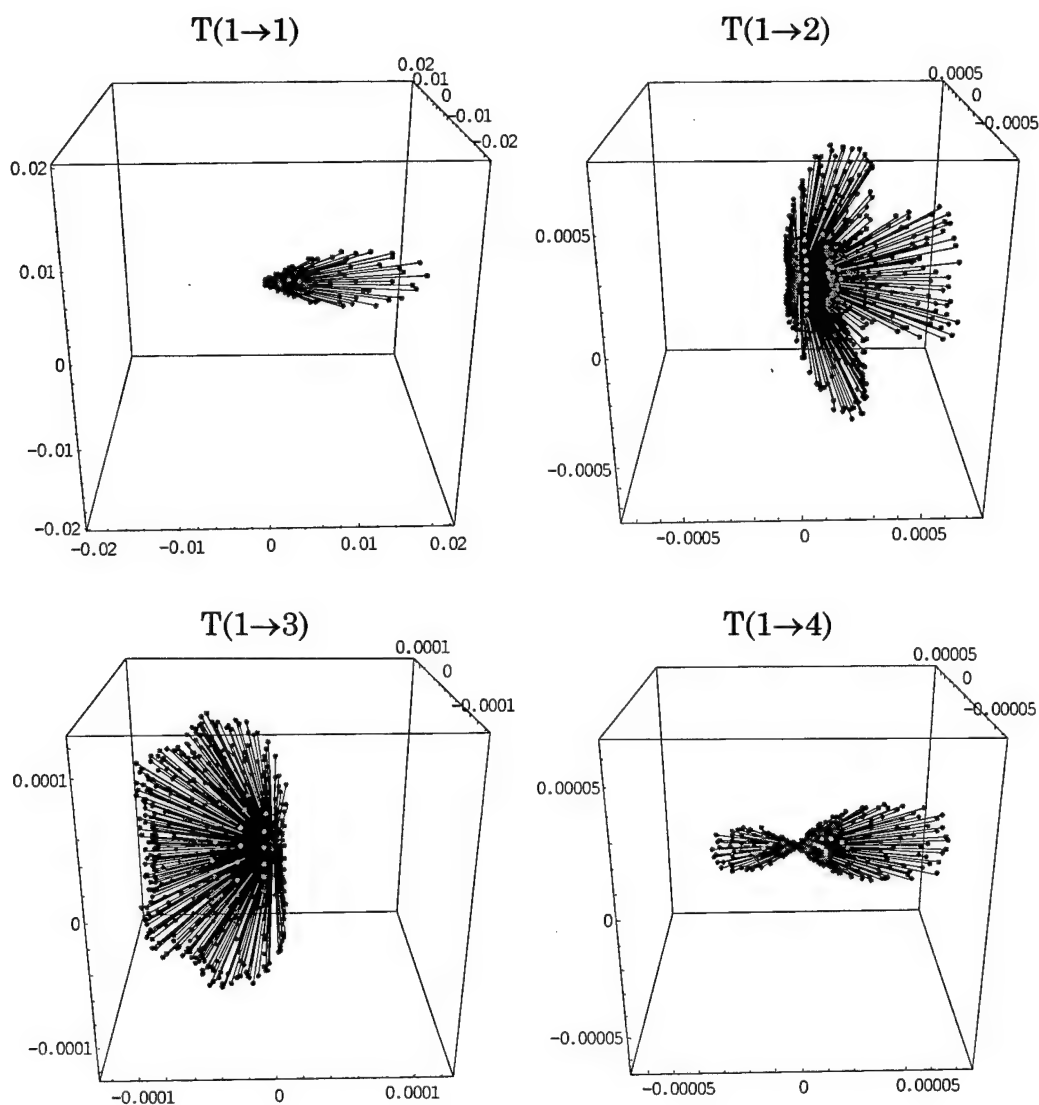


Figure 39 The scattering of ^{16}O . Group one to the first four groups of the LANL-30 group structure.

Note that the four illustrations have different scales. Relative to the group 1→1 transfer, the 1→2 and 1→3 and 1→4 are progressively smaller. This is consistent with the physics of the scattering process.

The collision of a neutron with oxygen is far less efficient in slowing down the neutron than hydrogen. Of course, it is the hydrogen in H_2O that makes

water such a good moderator. Hydrogen has a fairly uniform scattering distribution in the first five groups (Figure 31). A plot of the T-matrix for oxygen (using the same group structure and a $21 \times 40 \rightarrow 762$ facet quadrature) shows that the group-to-group probability distribution falls off rapidly as a function of energy lost.

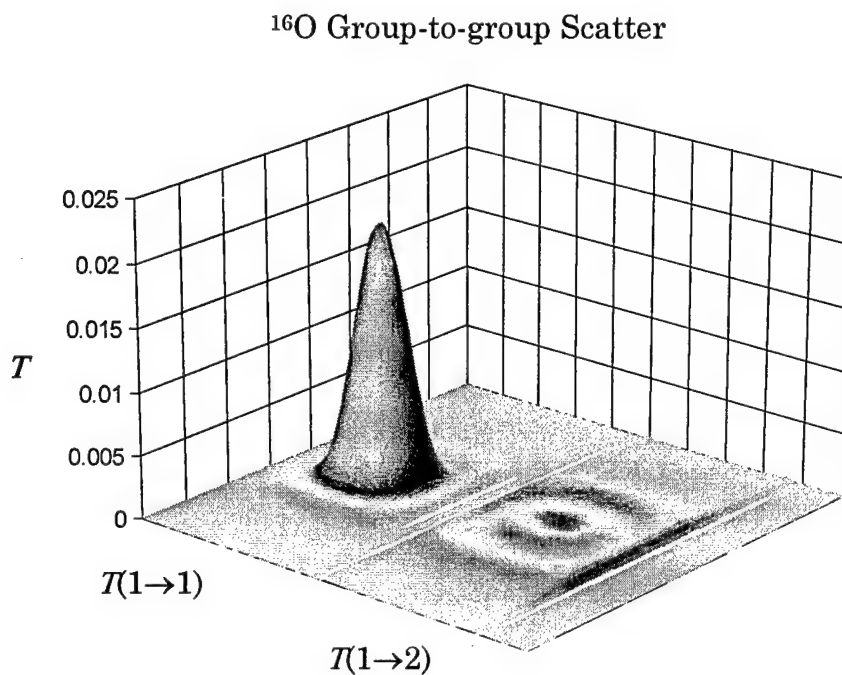


Figure 40. Group-to-group T-matrix of ^{16}O on the Cartesian map (LANL-30 Group).

While the $(1 \rightarrow 2)$ scatter of Figure 40 seems smooth, examination of the scatter in Figure 39 shows that it is highly anisotropic. A close-up of the scatter on the Cartesian plane demonstrates that there is a significant amount of structure to the scatter, which can not be matched with a strictly positive spherical harmonic expansion.

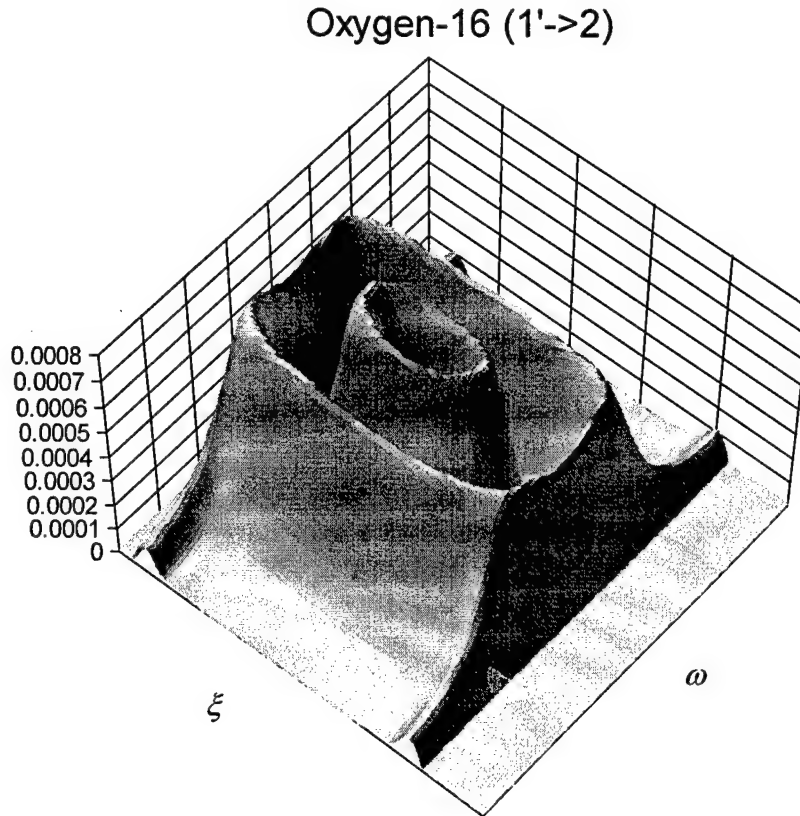


Figure 41 Detail of (1→2) T-matrix scatter of ^{16}O on the Cartesian map.

All the scattering data presented so far was created with T-Scat. The data is strictly non-negative and tends to behave in a manner consistent with what is known of the scattering physics. Taken together, the data provides some confidence that what T-Scat is doing is appropriate. The next step is to see how well the facet integrator, T-Scat, is working. Particularly we want to ensure such error tracks with standard MC integration. It is also important to know if the integration is practicable. We'll show that a reasonable error can be achieved in a reasonable amount of time, and provide some ideas for reducing such error even further. Finally, a comparison of the results of the MC facet method with that of the spherical harmonics method is presented.

Convergence, Error Tracking and Calculation Time

T-Scat outputs a number of files that can be used to study the processes at hand. First, is a data file that describes the group and quadrature structure used. It includes the materials being investigated, the scattering laws applied and tracks the convergence for the $T_{1,1}^{1,1}$ transfer. For each group, the total cross section, σ_g^t , is calculated and output. For each facet the directional ordinate, $\hat{\Omega}_n$, is output. For each $g' \rightarrow g$ and $n' \rightarrow n$ transfer T-Scat outputs the integral value: $T_{g'g}^{n'n}$, the angular first moment, $\bar{\Omega}_{g'g}^{n'n}$, the counts in each facet, $M_{g'g}^{n'n}$, and the error for each facet, $\varepsilon_{g'g}^{n'n}$.

In performing the integration, T-Scat doubles the number of scattering draws for each iteration. The code terminates when the maximum number of draws is reached, or the error for *one* of the facet values is less than the selected tolerance.

After M draws, the error for each facet is calculated as

$$\varepsilon_{g'g}^{n'n} \approx 1.96 \frac{\left[\left(\frac{1}{M} \sum_i \zeta_{i g'g}^{n'n} \right) - \left(\frac{1}{M} \sum_i T_{i g'g}^{n'n} \right)^2 \right]^{1/2}}{M^{1/2}} \quad (186)$$

where ζ was defined in equation (70), and corresponding to a 95% confidence that the value for that transfer lies within ε of the estimated value³³.

Figure 42 shows the value of the 1→1 group and facet transfer for oxygen dependent on the number of draws (LANL-30 group, 21 x 40 facets).

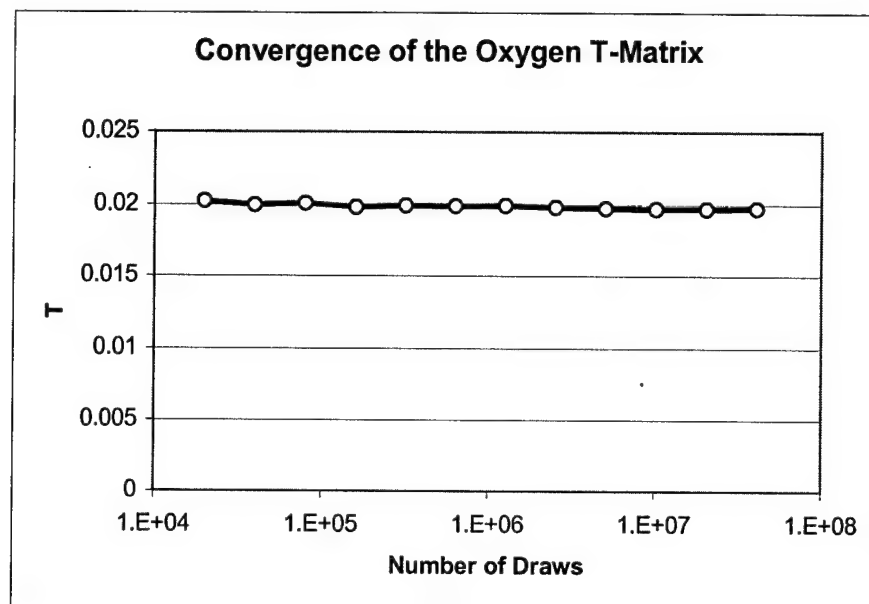


Figure 42. T value of the oxygen 1→1 group and facet transfer.

Expanding the ordinate axis and placing the error bars on the data using equation (186) above, Figure 43 shows that as the number of draws increases the newly calculated T value is within the 95% confidence level of the previous estimate. Figure 44 plots the fractional error and shows that it agrees well with the expected $1/\sqrt{N}$ convergence.

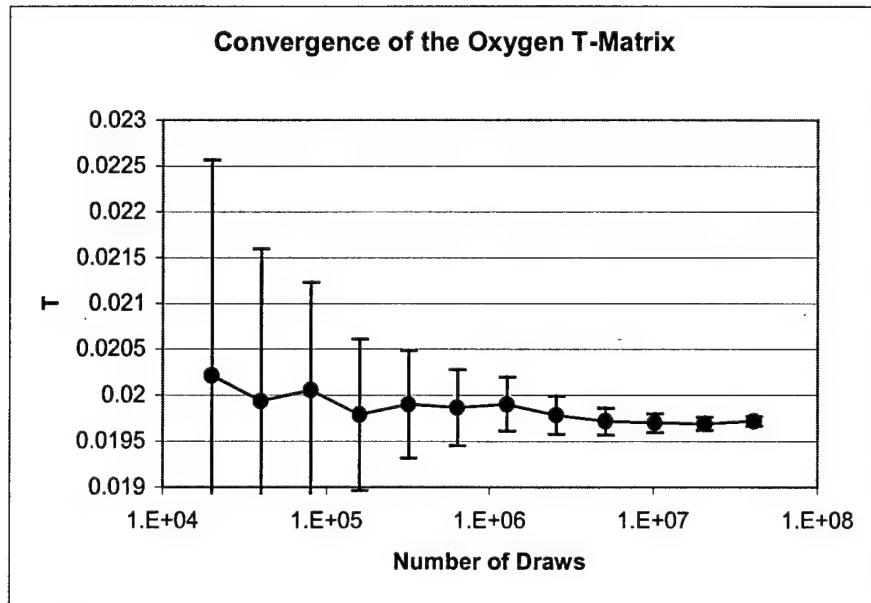


Figure 43. T value of the oxygen transfer with error bars.

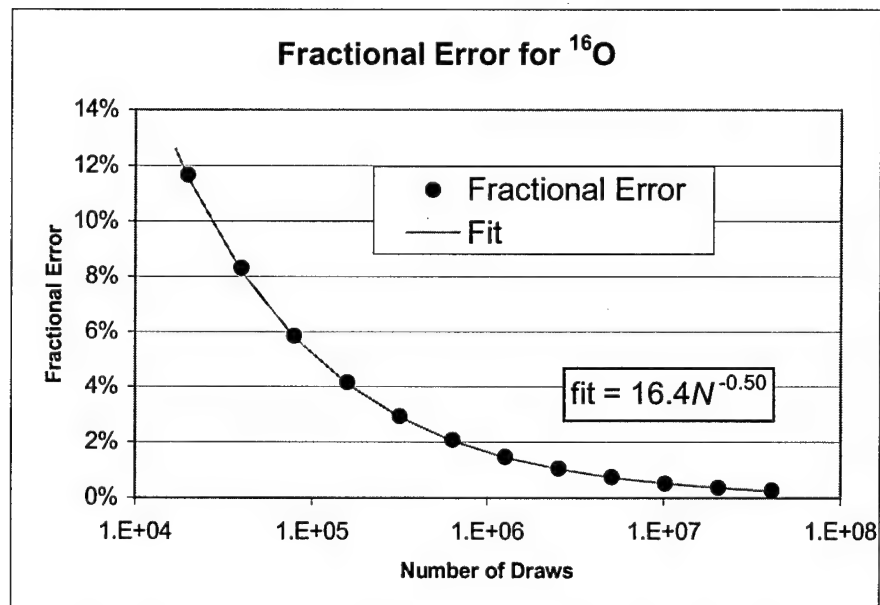


Figure 44. Fractional Error matches $N^{-1/2}$ convergence.

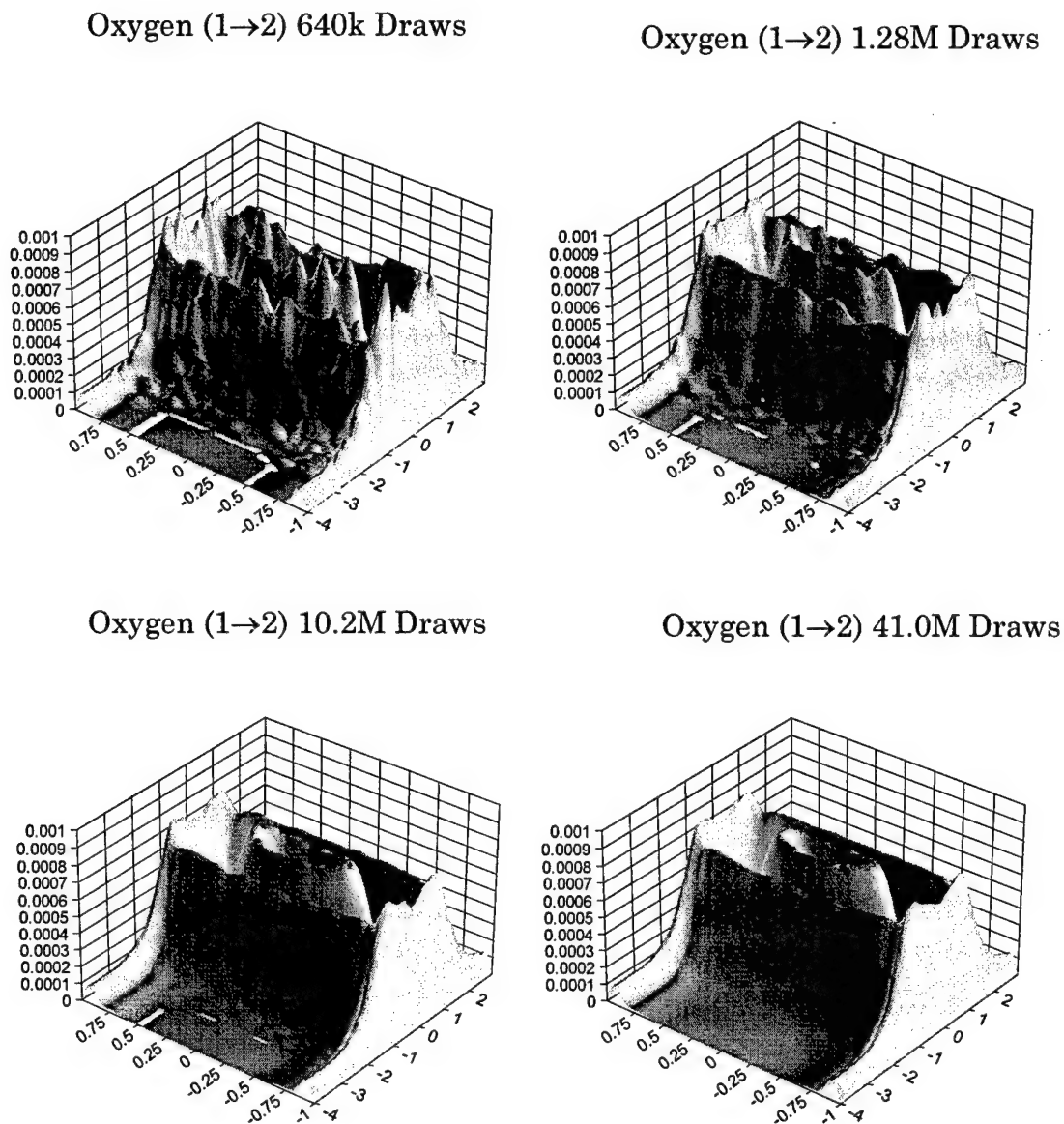


Figure 45. Increasing the number of draws on the $^{16}\text{O}(1 \rightarrow 2)$ transfer using a $21 \times 40 \rightarrow 762$ facet quadrature.

While 20 million draws provide better than half a percent error in the most likely transfer for oxygen, this is certainly not the case for the least probable scatters in the transfer matrix. Recall that the peak of the $^{16}\text{O}(1 \rightarrow 2)$ transfer was about 50 times smaller than $^{16}\text{O}(1 \rightarrow 1)$ transfer. A look at the Cartesian map of the T-matrix for this scatter reveals the effect of increasing

the number of draws (Figure 45). For a small number of draws the shape of the scatter transfer is discernable but not distinct. At about 10 million draws the essential shape of the scatter is preserved. Of course this is for a $21 \times 40 \rightarrow 722$ facet quadrature coupled with the LANL-30 group structure. Different quadratures will produce different results dependent on the group structure used.

Still, by its nature T-Scat samples the T -matrix in those most probable scatter regions. More particles land in the areas they're supposed to. Thus the code performs well for anisotropic scattering where the scattered neutrons are confined to a small portion of solid angle. The error changes across the T -matrix. Figure 46 shows the $^{16}\text{O}(1 \rightarrow 1)$ transfer while Figure 47 shows the absolute error of that transfer for 5 million and then 20 million draws. The absolute error is greatest where the integral is greatest. Of course, by sampling more the error is reduced. While the absolute error appears worse in the peak regions, the fractional error is much less. Figure 48 shows a log plot of the error for the within-group scatter.

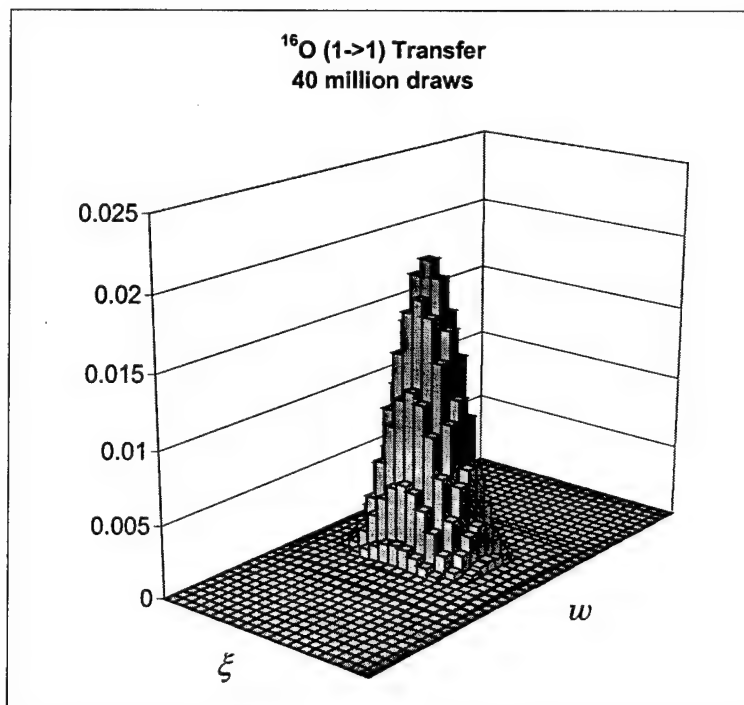


Figure 46. Within group scatter $^{16}\text{O}(1\rightarrow 1)$ at 40 million draws

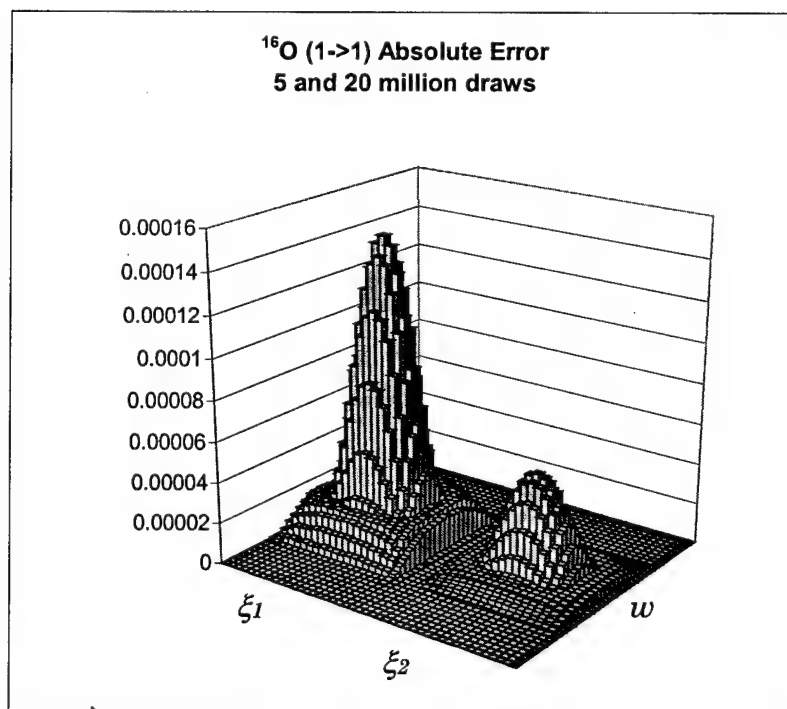


Figure 47. Absolute error for $^{16}\text{O}(1\rightarrow 1)$ transfer at 5 and 20 million draws.

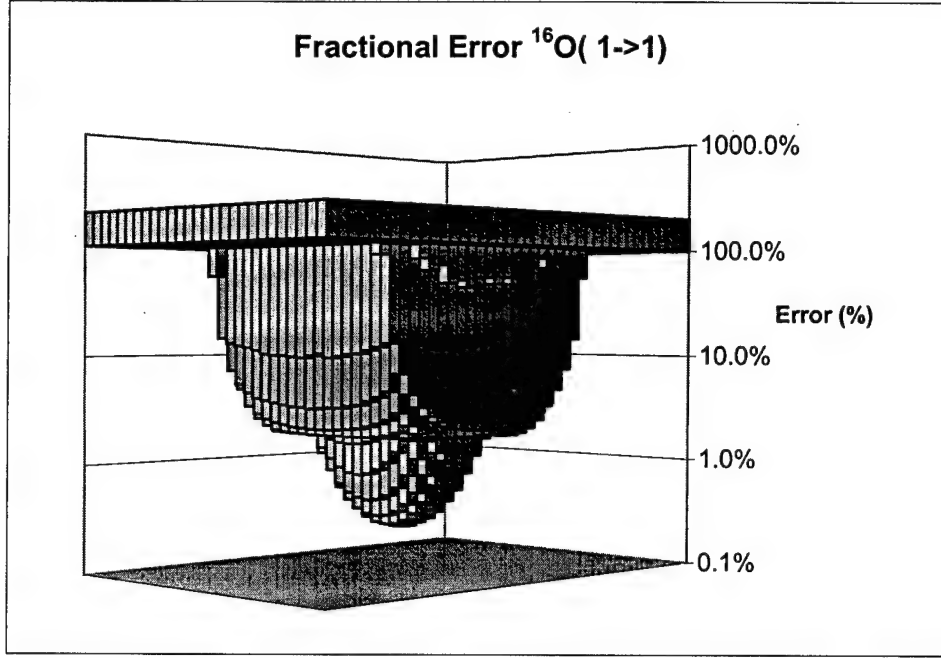


Figure 48. Fractional error of $^{16}\text{O}(1 \rightarrow 1)$ transfer (20 million draws).

A wholly different look at error is to examine what happens when the scattering is forced to be one group, isotropic. In this case all the facets should have the same value. For a $10 \times 16 \rightarrow 130$ facet structure, we plot the fractional error, ε_f , where

$$\varepsilon_{f \frac{n'n}{g'g}} = \frac{\varepsilon_{g'g}^{n'n}}{T_{g'g}^{n'n}}, \quad (187)$$

as a function of the number of draws in Figure 49. The fractional also tracks with the expected $1/\sqrt{N}$ convergence.

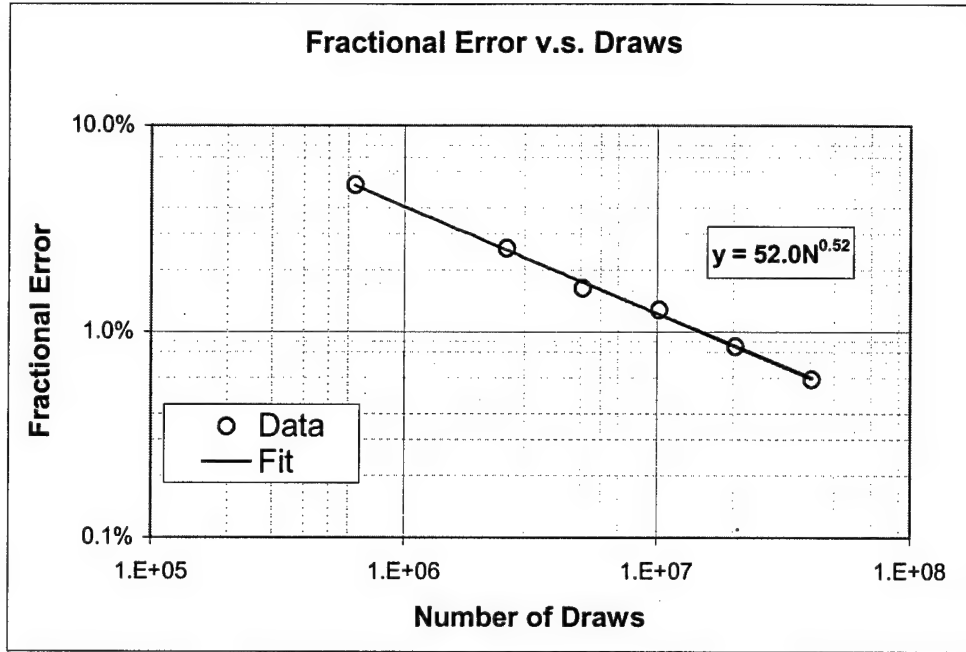


Figure 49. Fractional error of one group, 160 facet isotropic scatter.

One variance reduction technique conceived but not implemented in the code is the splitting of the scattered azimuthal (ω_L) draw. Because the scatter is azimuthally symmetric about the scattered angle, a split of 100 or 360 neutrons could be made at this point and then tracked to the appropriate facets. Because it is the calculation of the scatter type and process that is the most time consuming in the code, this would lead to considerable savings.

Another variance reduction scheme could be considered when the integration is being performed in a resonance region. Right now, the draw is uniform over the incident energy, although we know that the integral depends on $\sigma_s(E')$. In a group with a large number of resonances, the MC method might have difficulty in converging to the correct answer. Drawing

the incident energy based on $\sigma_s(E')$ might improve the results of the integration.

As it stands the code runs fairly fast. On an IBM 300MHz Pentium II processor with 64Mbyte RAM, timing runs were performed for a single incident group and facet. For the 21 x 40 facet structure (comparable to an enormous S_{26} level symmetric quadrature) the first group scatter to all scattered groups and facets was calculated. The code wall clock time as a function of draws for this physics model is plotted in Figure 50. After about one hour, 80 million T-matrix samples have been calculated.

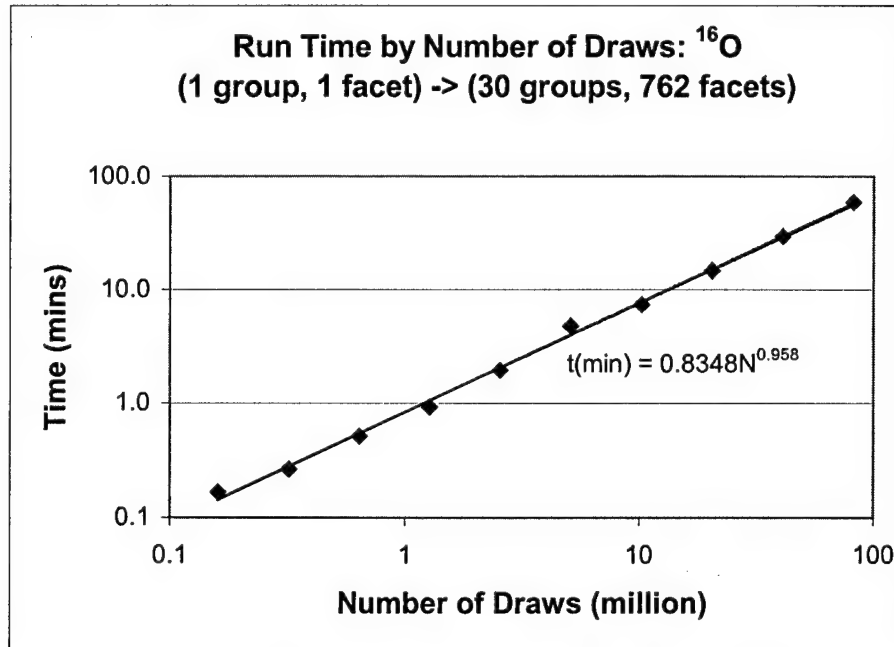


Figure 50. Run time for a single incident group and facet.

The S_{10} quadrature consists of 120 ordinates. The Cartesian counterpart is a 10 x 15 \rightarrow 122-facet quadrature. As will be shown in the following chapter, 80 million draws are not required for accurate transport results.

Instead, a typical number of draws for a full set of data is about five million lasting about five minutes. That's 5 incident facets by 30 groups by 5 minutes each or a complete runtime on the set of about 12.5 hours. The other advantage is that this calculation is only performed once for the quadrature and group selected. Stored in its compacted form (say on a CD), rebalancing and mixing take only a few minutes to prepare the files for a desired transport problem.

One way to significantly reduce the run time of building such a library is to run each incident facet and group calculation on a separate processor. Because the calculation of one integration is completely independent of the others, the data can be combined after the processors have completed their calculations. With 150 processors, the entire 122 facet quadrature library could be obtained in under 10 minutes for each isotope.

Finally it should be noted that the real test of how well these libraries work is in how they perform in the transport code. Such information is presented in the next chapter. The following section, however, continues to look at the scattering T-matrix. It examines how the MC facet method compares with its spherical harmonic counterpart. Particularly, we demonstrate the non-negativity of the MC facet method.

The MC Facet Approach vs. the Spherical Harmonic Method

Up to this point we've established that the results of the T-matrix created with the MC facet method are consistent with our expectation of the physics. It is also been shown that the MC facet method can be implemented to create a reasonably accurate T-matrix in a modest amount of time. Such a scattering matrix can also be created directly from the spherical harmonic expansion of the scatter. In fact, Tetran performs this calculation during the transport process. We can, to some extent, use the same visualization tools to examine the behavior of the spherical harmonic expansion of the scattering cross section.

First, examine the within group scatter of hydrogen as shown in Figure 31. The P3, P5 and P7 Legendre expansions of this distribution are shown in Figure 51.

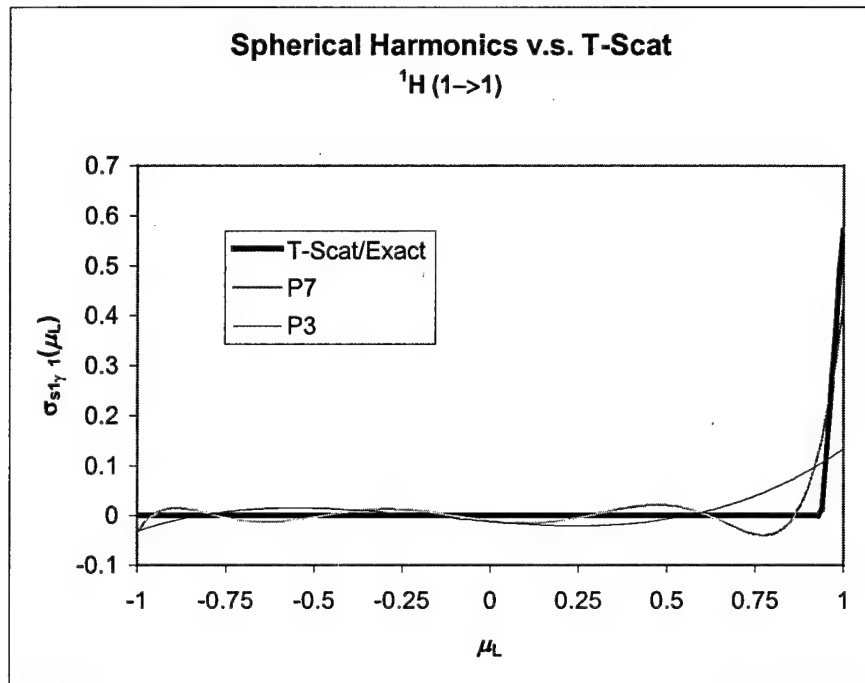


Figure 51 Legendre Expansion of the hydrogen differential scattering cross section.

The effect such an expansion has on the scattering distribution is even more dramatic when one examines the spherical harmonic. Figure 52 shows the P3 and P7 spherical harmonic expansions of the within group scatter ($1 \rightarrow 1$) of hydrogen using the LANL-30 group structure (Preusser interpolation of the scattered data with TableCurve-3D). The chart is cut off at zero to show exactly where the truncated expansion goes negative.

Hydrogen P3 (1→1)

Hydrogen P7 (1→1)

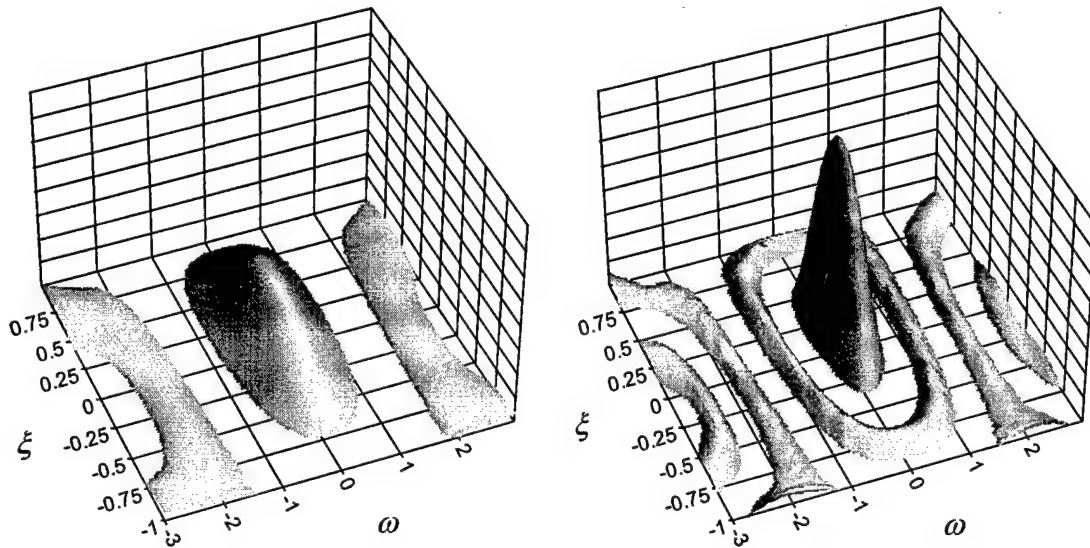


Figure 52. Cartesian map of the P3 and P7 spherical harmonic expansions of ^1H . Within group scatter (1→1) LANL-30. The data is cut off at zero to demonstrate the *sea* of negativity.

It is in these regions that the potential for creating negative sources exists. Increasing the order of the polynomial may better approximate the forward scattered peak, but the depth of its negative regions becomes more severe as was shown in Figure 51.

As the atomic weight of the target nuclide becomes larger, the scattering probability distribution function, $f(E', \mu_{cm})$, may have more structure.

When the scatter is discrete level inelastic, there are other problems. The third order polynomial is unable to match the structure and so diffuses the neutrons in all directions. Further, as expected, this approximation has negative components. The seventh order approximation better matches the shape, but also fails to maintain non-negativity (Figure 53).

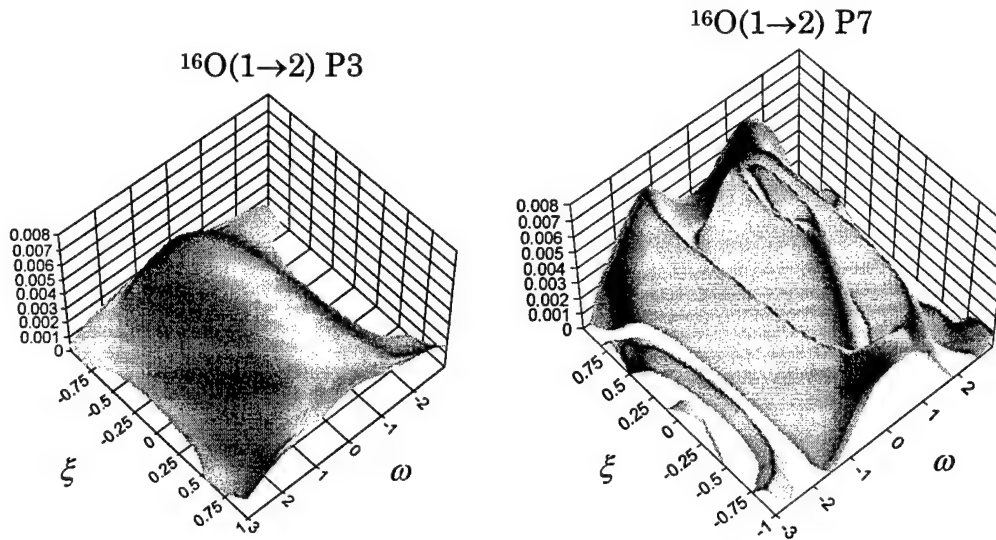


Figure 53. Group 1→2 transfer for ^{16}O using spherical harmonics.

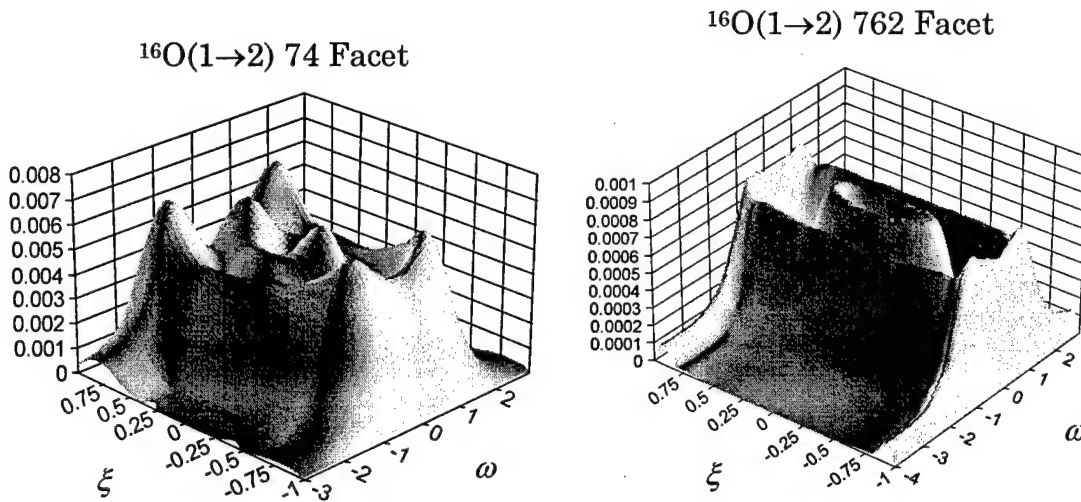


Figure 54. Group 1→2 transfer for ^{16}O using T-Scat (some interpolation error in 74 facet case).

The 74 and 762 facet cases are shown for comparison in Figure 54. The 762 facet case demonstrates what the scattering should look like. The 74 facet case (comparable to an S_8 quadrature) is strictly non-negative. The source facet is off the equator at $\xi = 0.16$ accounting for the polar asymmetry.

The peaks at $\xi \approx 0.75$ are a bit larger than the actual data, and are artifacts of the interpolation routine.

Figure 55 shows where the spherical harmonic approximations go negative, both for the P3 and P7 truncations. The bi-modal behavior of the scatter results from two competing mechanisms. The scatter distribution, $f(E'_1, \mu_c)$, is highly forward peaked $\mu_L = 1$, but the optimal scattering angle for the group-to-group transfer is about $\mu_L \approx 0$ (see Figure 38).

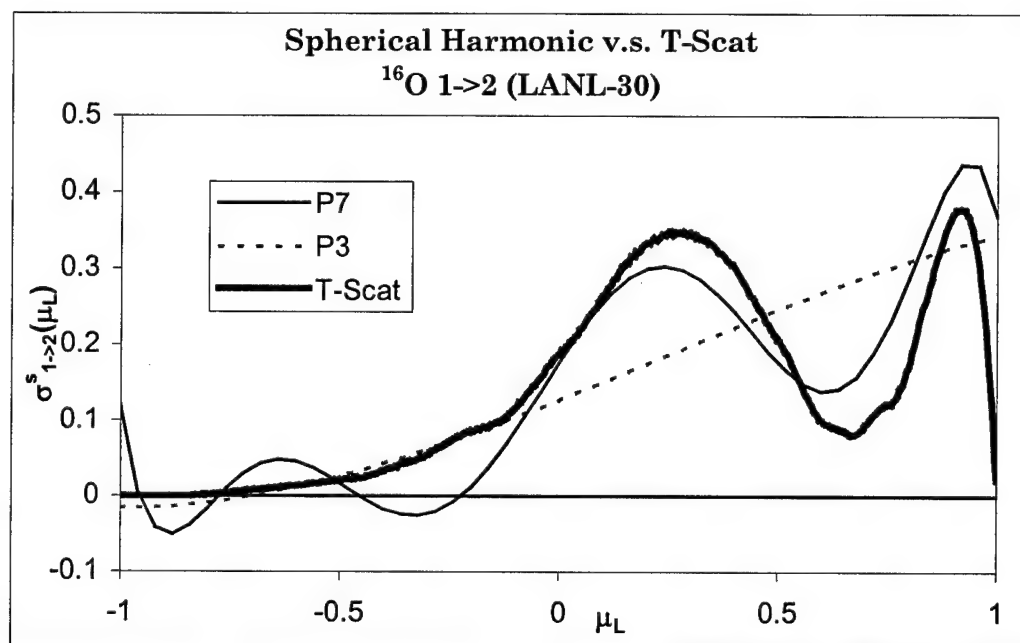


Figure 55. Spherical harmonic comparison with T-Scat for elastic and inelastic scatter of ^{16}O . (Group 1 \rightarrow 2, LANL-30 Group structure)

Graphically, it is easy to see the difficulties with using Legendre polynomials to match data that sometimes is only C^0 continuous. It is a more subtle study to see if such polynomials adversely effect transport codes. The

abundance of attempts to fix the problem with source negativity suggests that such adverse effects exist.

Researchers at AFIT have developed a new spatial characteristic method that allows for the study of deep penetration problems with very optically thick cells^{34,35}. The exponential characteristic method (EC) requires that the source be non-negative or the code will fail⁷. Other transport codes incorporating exponential methods have also failed when dealing with anisotropic scattering⁸.

Source negativity also impacts convergence of the transport codes. A common fix is to set the source to zero wherever it becomes negative. This also impacts the convergence of the code, but in a non-linear, and often unpredictable way. The result may be to arrive at an answer that is incorrect, or to severely impact how long convergence takes⁹. The effect is more dramatic if finer group structures are used. In the examples above, a fairly coarse *survey* structure was used (LANL-30 Group).

In the following chapter we directly compare the performance of the T-Scat generated T-matrix with its spherical harmonic counterpart. In the next section, however, we continue looking at the scattering matrix generated by T-Scat. In particular, we examine the problems of angular support for ordinate-to-ordinate methods, and the problems of numerical diffusion for the facet method.

The Impact of the Angular Quadrature

Earlier we mentioned the failure of ordinate-to-ordinate methods to scatter to the next group if the nearest scattering angle wasn't close enough. We quantify that here, and then look at comparable facet quadratures. We'll find that the MC facet method guarantees within group scatter and next group scatter. Further, no group-to-group scatter can be missed if it is physically allowed to happen.

Recall from chapter 4 (Angular Support) that the scattering angle in the laboratory frame is given by

$$\mu_L = S(E, E') \equiv \frac{1}{2} \left[(A+1) \sqrt{\frac{E}{E'}} - (A-1) \sqrt{\frac{E'}{E}} - \frac{QA}{\sqrt{EE'}} \right] \quad (188)$$

For elastic scattering, $Q = 0$, equation (188) can be re-written as

$$\mu_L = \frac{1}{2} \left[(A+1) \sqrt{\frac{E' - \Delta E}{E'}} - (A-1) \sqrt{\frac{E'}{E' - \Delta E}} \right], \quad (189)$$

where ΔE is the energy lost in the collision. Expanding equation (189) in a power series about $\Delta E = 0$, the scattering angle for small energy loss is

$$\mu_L = 1 - \frac{A}{2} \frac{\Delta E}{E'} + O(\Delta E^2). \quad (190)$$

Because of this relation, ordinate-to-ordinate methods lack angular support when fine energy groups are used with modest angular quadratures.

Scattering Within Group

We first examine the within group (1→1) transfer. Is it possible to scatter (change directions) while remaining in the same group? From a physical standpoint the answer is yes. Neutrons at 17 MeV may scatter to 15.01 MeV and still remain in the same group (group 1 of the LANL-30 group structure). Even for very fine energy group structures a loss in energy involves a change in direction. But, as was shown earlier, in ordinate-to-ordinate methods, if there is no directional ordinate within the scattering range (a lack of angular support), such a transfer can not take place.

Using equation (31) for the within group scatter of hydrogen, $\mu_L (1 \rightarrow 1) = 0.939$. To guarantee within group scatter for all groups, the most stringent requirement is for group 2, namely $\mu_L (2 \rightarrow 2) = 0.949$. The next question is what kind of angular support is required to guarantee within group scatter?

For comparison, we use a level-symmetric quadrature to represent the ordinates of the ordinate-to-ordinate method. Mikols demonstrated that Lobato quadratures are even more stringent¹¹. The nearest neighbor for such a quadrature is shown in Table 3 where the order of the quadrature and number of ordinates in the quadrature set is shown next to the nearest neighbor.

Table 3. Nearest Neighbor μ_L for Level Symmetric Quadratures.

Level-Symmetric S_N	# of Ordinates	Nearest μ_L
S_2	4	0.333
S_4	24	0.755
S_6	48	0.884
S_8	80	0.922
S_{10}	120	0.941
S_{12}	168	0.952
S_{16}	288	0.965

To achieve within group scatter for all groups of hydrogen (using the LANL-30 group *survey* structure) the S_N order must be at least 12. If we perform the same analysis using a fine group structure often used in transport calculations (e.g., Vitamin-J), the minimum scattering angle is greater than 0.9654 for 104 of the 175 groups! Because increasing the quadrature order indefinitely becomes untenable, the choice must be made to sacrifice within group scatter, ignoring the physics of the calculation. The MC facet method has no such restriction. Because the minimum angle between adjacent facets is 0 ($\mu_L=1$), within group scatter is guaranteed for any quadrature set.

Angular Support for Downscatter

The next least restrictive case is to examine scatter to the next lower group. How close must the angles be to guarantee scatter to the next lower group? Again we examine hydrogen. The maximum energy that can be lost in the group-to-group transfer is from the top of the incident group to the bottom of the scattered group. For the LANL-30 group structure, (1→2) corresponds to 17 MeV → 13.5 MeV. The result is a scattering cosine of $\mu_L = 0.8912$.

Using Table 3 again we see that an S_8 quadrature (80 ordinates) is required. For the Vitamin-J structure, 15 of the 175 angles require S_{16} or higher. Table 4 shows the number of groups failing as the quadrature order is reduced.

Table 4. Number of groups Failing Nearest Neighbor Downscatter for Vitamin-J group structure (175 total groups).

Level-Symmetric S_N	# of Ordinates	# Failing of 175
S_4	24	172
S_6	48	124
S_8	80	109
S_{10}	120	96
S_{12}	168	28
S_{16}	288	15

Of course, if the quadrature fails to allow downscattering to the next group when the physics dictates it should, that group is simply skipped. The result is a depressed or perhaps non-existent flux in the lower group.

Again the MC facet method guarantees that all groups are scattered to and that no group is missed because the scattering is continuous in angle within the calculation of the T-matrix.

As an illustration of this type of facet scatter, consider an equal area quadrature as previously discussed. Here, the scattering is strictly from the pole to the facets below. We first examine group 1→1 scatter for the LANL-30 group structure. The coarsest structure for T-Scat is to scatter from one hemisphere to the next. We next increase the number of total latitudinal facets to 2, 4, 10 and 100. The results are shown in Figure 56. While for the fine mesh a number of facets are reached, even the coarsest meshes, as is shown by equation (35), have some portion of the scatter going to the adjacent facet.

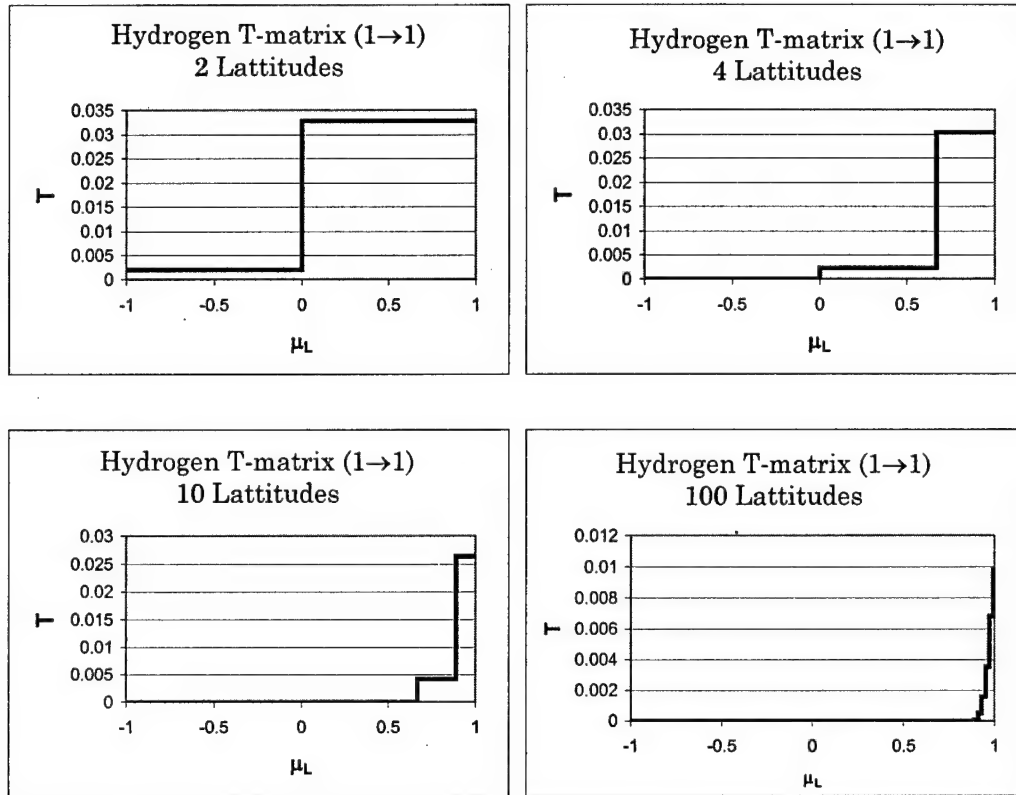


Figure 56. Guaranteed within group scatter [$^1\text{H}(1 \rightarrow 1)$] for the MC Facet Method. Note scale change in 100 latitude chart.

As expected the MC facet guarantees scatter to groups where the physics says they should. Again, this is because at the heart of the MC facet method the scattering is taken as continuous in both energy and angle.

Skipping Groups

Finally, it should be noted that ordinate-to-ordinate methods may also skip groups if there is insufficient angular support. Because the MC facet method guarantees scatter to all $\mu_L \in [-1, 1]$, no groups will be skipped if the physics dictates they're to be scattered to.

Angular Dispersion

The price paid for guaranteeing within group, next group and non-skipped group scatter is in angular dispersion. Figure 57 shows such dispersion by comparing facet structures (the effect is also noticeable in Figure 56). Both are for hydrogen within group scatter. The coarsest structure tends to redistribute a small portion of the scatter into a direction that by kinematics cannot be reached (recall that for the polecap quadrature there are ordinates at 1 and -1, while the other ordinates are centered on the facet).

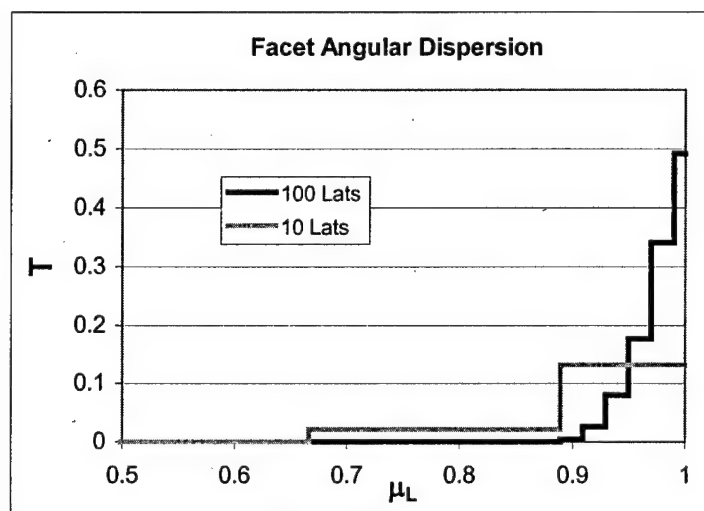


Figure 57. Facet angular dispersion for $^1\text{H}(1 \rightarrow 1)$ scatter (expanded axis).

Of course, Legendre polynomials suffer from the same type of dispersion by assuming scatter is possible in regions where it is not. This is evident by comparing the P3 and P7 approximations in Figure 51. Further, such approximations must have negative regions where the actual matrix is zero. Just as the facet method is dependent on the quadrature used, the spherical harmonic expansion is also dependent on the order of the S_N method used.

The best way to determine if such dispersion is problematic is to try the cross-section data libraries in a transport code. This is done in the following chapter which evaluates the transport code results. In particular we'll examine comparable quadratures to determine if there's a significant problem or not.

One way to reduce the angular dispersion in the facet method is to perform an angular rebalance to conserve the first angular moment of the scatter. This is discussed in the next section.

The Effects of Angular Rebalance

Ideally we would examine the effects of angular rebalance on diffusion-like problems in the transport code chapter. Unfortunately, the absence of a convergence accelerator in TETRAN makes such an examination impossible at the present time. In this section we'll continue to examine the T-matrix using the tools developed earlier. In particular, we want to see that the rebalance doesn't turn the matrix into something unrealistic. And, better, we hope that the effects of the rebalance are consistent with our expectations.

Perhaps the best benefit of rebalance is the reduction of angular dispersion as illustrated in Figure 57. In that figure, the T-matrix values before and after rebalancing are shown. In general, we would hope that, after the rebalance, the peaks of the scattering distributions would be more pronounced and the dispersive effects reduced.

To look at this, take a standard 74 facet quadrature set with incident neutrons through the polecap. The azimuthal angle is collapsed and the T-matrix results for before and after rebalancing are shown in Figure 58. The purpose of rebalancing, as described earlier, is to conserve the first angular moment of the scatter. This usually results in redistributing the scatter matrices towards peaks.

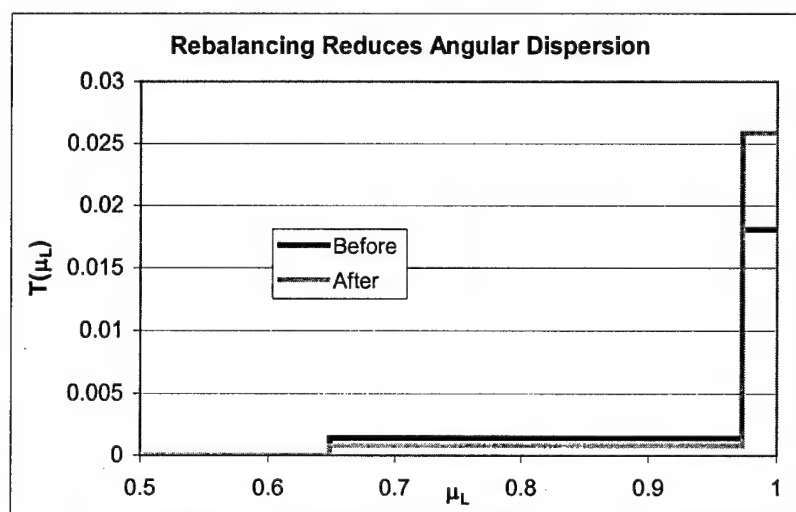


Figure 58. Reduction of dispersion using angular rebalancing. Here, 74 facet quadrature for ^1H ($1 \rightarrow 1$)

The effect can be seen more dramatically in three dimensions by examining the Cartesian grid of similar data. Here a $9 \times 12 \rightarrow 86$ facet structure is used to center the source of the scatter at $\xi = 0$ (Figure 59). Again, the T-matrix values before and after rebalancing are presented side by side for hydrogen. For the within group scatter ($1 \rightarrow 1$), we see that the peak of the rebalanced data is higher and better defined.

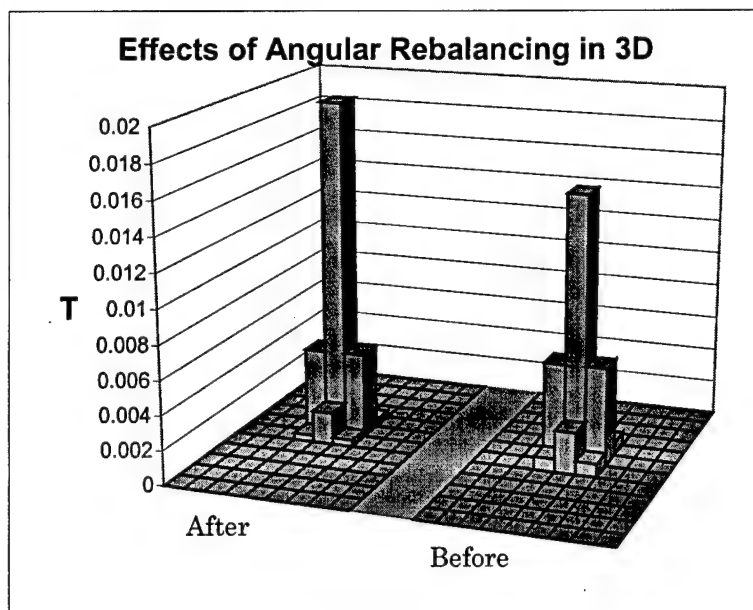


Figure 59. Effects of angular rebalance for hydrogen ($1 \rightarrow 1$).

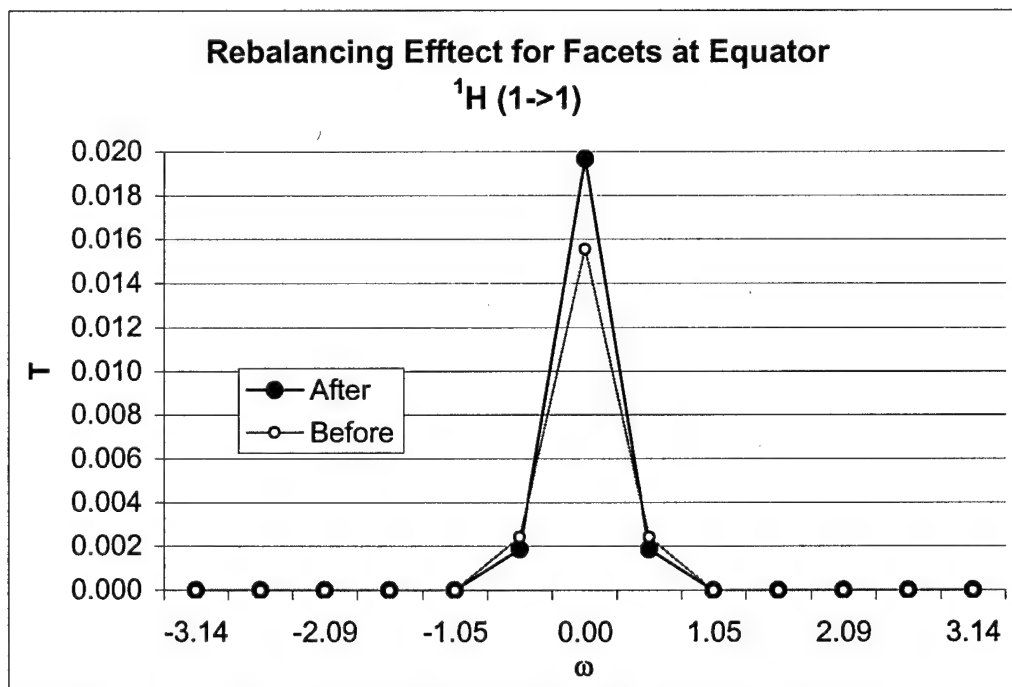


Figure 60. Effect of angular rebalance for equatorial facets, ^1H ($1 \rightarrow 1$).

Next we examine the same type of results for the oxygen ($1 \rightarrow 2$) scatter.

As for hydrogen, we look at a linear plot of the zeroth moments of the facets

along the equator before and after rebalancing. Rebalance effects are compared to a baseline of 100 equatorial facets that show the strong structure of the ^{16}O (1 \rightarrow 2) scatter. Rebalancing of the coarse mesh (9x12 \rightarrow 86 facet quadrature) and the medium mesh (9x20 \rightarrow 142 facet quadrature) are shown in Figure 61 and Figure 62 respectively.

Conservation of the first angular momentum reduced the structure in the rebalanced coarse mesh. For the medium mesh, just as it was for the within group scatter of hydrogen, the peaks are enhanced, more closely resembling the actual scatter structure.

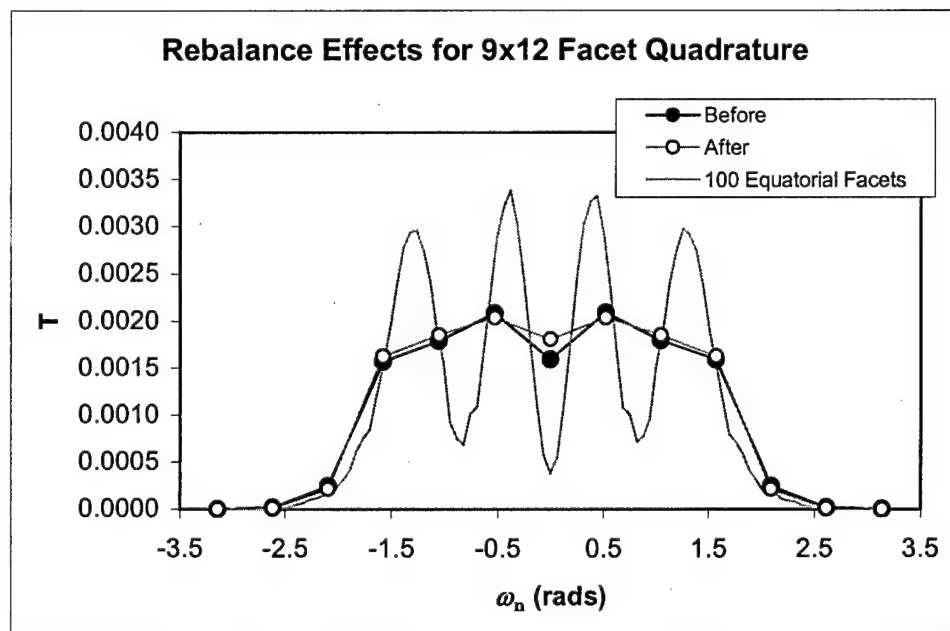


Figure 61. Rebalance of ^{16}O (1 \rightarrow 2) T-matrix for 12 equatorial facets.

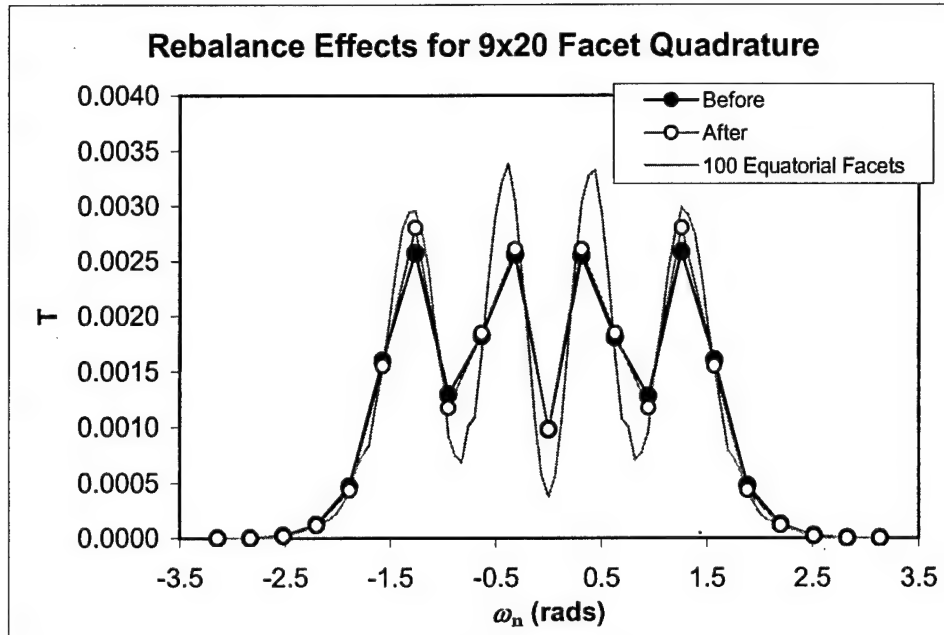


Figure 62. Rebalance of ^{16}O (1 \rightarrow 2) T-matrix for 20 equatorial facets.

Overall, the rebalance seems to reduce dispersion, particularly for modest mesh sizes. This is, however, the secondary goal of the rebalance. Its primary mission is to ensure that the scattering libraries perform well for diffusion-like problems. Our current code limitations (TETRAN's lack of a convergence accelerator) do not allow us to examine the libraries at low energies, but the results shown here suggest that rebalancing will, at the very least, not impair the accuracy and may even improve it. Even for high energy problems we'll see that rebalancing can, in fact, improve the accuracy of our transport code results.

Scattering Matrix Conclusions

After a thorough examination of the scattering matrix we've shown a number of things: The MC facet method creates a T-matrix that is

- consistent with the physics,
- guaranteed non-negative,
- combines both elastic and inelastic collisions,
- guarantees within group and next group scatter regardless of quadrature or energy group structure, and
- can be rebalanced to conserve the first angular moment of the scatter.

Further, it does so at a reasonable accuracy and in a reasonable amount of time. And, if the user is willing to spend the time, noting that the library need only be built once, *any* T-matrix accuracy can be achieved.

While significant achievements on their own, it remains to be seen how well such a T-matrix will work in a transport code. This is the subject of the following chapter. And although the Cartesian angular quadrature is not ideal, the next chapter will provide some comparison between the facet method and the spherical harmonic approach and demonstrate the viability of the MC facet method for neutral particle transport.

10. Transport Code Performance

So far, we've discussed the theory for the MC facet method and the code that implements that theory to create a T-matrix. Examination of this T-matrix data shows that it models the physics, is non-negative, guarantees within-group and next-group scatter, and conserves the first angular moment of the scatter. This chapter now looks at how well such a cross-section library performs in a transport code. We'll find that the T-matrix created with the MC facet method performs well for a number of sample problems, and in most cases is superior to a comparable spherical harmonic cross-section library.

This chapter begins to explore the capabilities of the T-matrix approach. Our goal is to demonstrate the capabilities of the T-matrices created by T-Scat in the transport code. These include

- Non-negative T-matrix libraries for single elements (e.g., ^1H , ^{16}O).
- Non-negative T-matrix libraries for compounds (e.g., H_2O , BO_2)
- Support for geometries with multiple materials (e.g., H_2O , Fe , ...).

Also investigated is the impact of various quadrature and group structures for some of the problems described and comparisons of comparable changes to the spherical harmonic counterpart.

Overview of the Transport Codes

The primary code used to investigate the new non-negative cross section libraries was TETRAN. TETRAN was developed at AFIT⁷. It is an unstructured tetrahedra mesh discrete ordinates radiation transport code. TETRAN solves the linear time-independent Boltzmann transport equation using linear or exponential characteristic spatial quadratures and is capable of working with multi-group cross sections and general anisotropic scattering.

As discussed earlier, TETRAN creates a T-matrix using spherical harmonics. We modified the code so that it could read T-matrix data directly from the cross section libraries created by T-Scat, T-Balancer and T-Mixer. In this way we can directly compare the results of the two methods using the same spatial mesh and group structure. Of course the angular quadratures are different, but effort is made to keep such quadratures as similar as possible (e.g., same number of ordinates).

Data is also compared with the results of MCNP using continuous energy and angle ACE libraries. These are the same libraries used to calculate the cross section data within T-Scat.

On occasion we also introduce comparison results from MCSN. As discussed earlier, this code performs transport continuous in space but discrete in energy and angle. It too reads the MC facet method T-matrix directly from file to create its cumulative distribution functions, for the MC

transport process. MCSN, TETTRAN, and MCNP provide an excellent set of tools to evaluate how well this new method performs.

Nuclides Investigated

T-Scat currently implements elastic, level inelastic and evaporation spectrum scattering laws. Nuclides and energy ranges were selected so that such scattering laws were the only ones required. Nuclides were also selected to demonstrate the anisotropic capabilities of the new method. Hence, lighter nuclides were of greatest interest. Nuclides and mixes tested include ^1H , ^7Li , ^{10}B , ^{16}O , ^{27}Al , ^{56}Fe , H_2O , BO_2 , Al_2O_3 , and others. The results presented in this chapter are representative of the results found for all these materials. Where possible, to demonstrate operation at high anisotropy, the highest energy groups of the LANL-30 and VITAMIN-J structures are used. In some instances lower energy groups are used to avoid unavailable types of scatter [e.g., (n, 2n)].

Definition of Terms

Units

The output data of TETTRAN is consistent with the tally output of MCNP. Such tallies are normalized to be per source particle. TETTRAN provides results for the

1. current through a surface (particles),

2. flux averaged over a surface (particles/cm²), and
3. flux averaged over a material region (particles/cm²).

If the source is given in particles per unit time, so too are the current and fluxes described above. In this research, only box geometries are used. All external surfaces are surrounded by vacuum. A cube of water represents a single material region. The water-iron-water geometry used in this research is a cube in a cube in a cube and represents three regions.

Error

MCNP reports the relative error for each of its estimates of the mean. The absolute error is based on the variance of the estimated mean calculated during the tally. The discrete ordinates code TETTRAN converges to a tolerance level of 10^{-6} . When an error is shown for MCNP, it is the relative error reported by the code, or absolute error defined as the relative error times the mean. Errors reported for TETTRAN and MCSN are based on the difference between their calculated values and those of MCNP. As mentioned earlier, it is unreasonable to expect that such codes would converge to the exact same result. What we hope to see is that MCSN lies between the results of TETTRAN and MCNP. It is also hoped that results using the MC facet approach perform somewhat closer to the MCNP result than those using spherical harmonics. It will be shown that, in most instances, this is indeed the case.

Spatial Quadratures

Of course neither MCNP nor MCSN use spatial quadratures. TETTRAN may implement one of two: linear characteristic (LC) and exponential characteristic (EC).

The linear characteristic method, as developed by Mathews³⁶, assumes a linear source and inflow flux distribution. Spatial moments are taken of the LC source distribution and a system of equations is set up to solve for the source. The LC method performs well if the spatial cells are optically not too thick. The method, however, may return negative flux values even if the cross section data is strictly positive.

The exponential characteristic method, however, creates strictly non-negative fluxes. The EC method takes zeroth and first spatial moments of the characteristic solution to the BTE and an assumed exponential distribution of the scattering source in a cell to calculate average and first moments of the angular flux²⁵. The method is excellent for deep penetration problems. The method, however, requires the source be non-negative. The availability of an anisotropic, non-negative, cross section library (the thrust of this research) makes the implementation of the EC method now feasible for multi-group, anisotropic problems. Both these methods are discussed in detail in Miller's dissertation⁷.

Because transport calculations implementing the LC method are quicker, many of the results of this chapter use LC. Use of the EC method is

demonstrated for some problems and in particular for problems with optically thick cells where the LC method fails to provide positive fluxes.

Uniform Cube Test Problems

The first test of the T-Scat data was with a uniform cube. The cube consists of a single material (10cm x 10cm x 10cm). A source emits isotropically throughout the material (1 particle/cm³-sec) and uniformly within a single energy group of the given group structure.

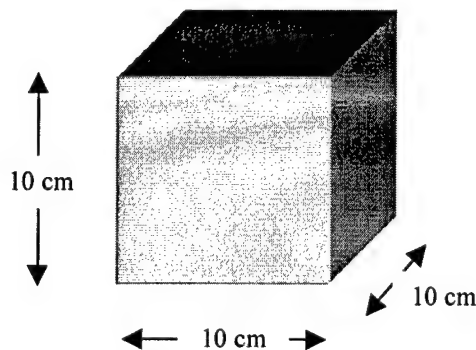


Figure 63. Dimensions of the simple cube.

Introducing Data for Single Nuclides

This section limits the cube material to a single nuclide. It introduces some of the results from TETRAN and MCNP and ends with a presentation of data from MCSN. In so doing, a number of characteristics of the MC facet method are revealed. Most comparisons are based on the region average scalar flux

$$\bar{\phi}_g = \frac{1}{1000 \text{ cm}^3} \int_0^{10 \text{ cm}} dx \int_0^{10 \text{ cm}} dy \int_0^{10 \text{ cm}} dz \phi_g(x, y, z) . \quad (191)$$

The first material tested was free hydrogen (1.0 g/cm²) at 300K. The problem was calculated using MCNP, TETTRAN with spherical harmonics (SH), and TETTRAN with the T-Scat library (five million scatter draws). This density is, of course, unrealistic. It was used for convenience, although one could use a larger cube at lower density to obtain the same results. The cube is divided into 161 spatial cells (tetrahedra). The LANL-30 group structure was used and the group scalar flux averaged over the material (equation (191)) for the first 10 groups is shown in Figure 64. The total group scalar flux spectrum is found by dividing the group scalar flux by the width of the group in MeV

$$\tilde{\phi}_g = \frac{1}{\Delta E_g} \bar{\phi}_g . \quad (192)$$

This is shown in Figure 65. The SH method employs an S8 quadrature (80 ordinates) with a P7 approximation while T-Scat uses the 8 x 12 → 74 facet structure. On this scale it is difficult to see exactly which of the TETTRAN results is closer to the MCNP solution. What can be said is that the T-Scat library is performing well. We can more closely examine the error of these data by comparing them to the MCNP result.

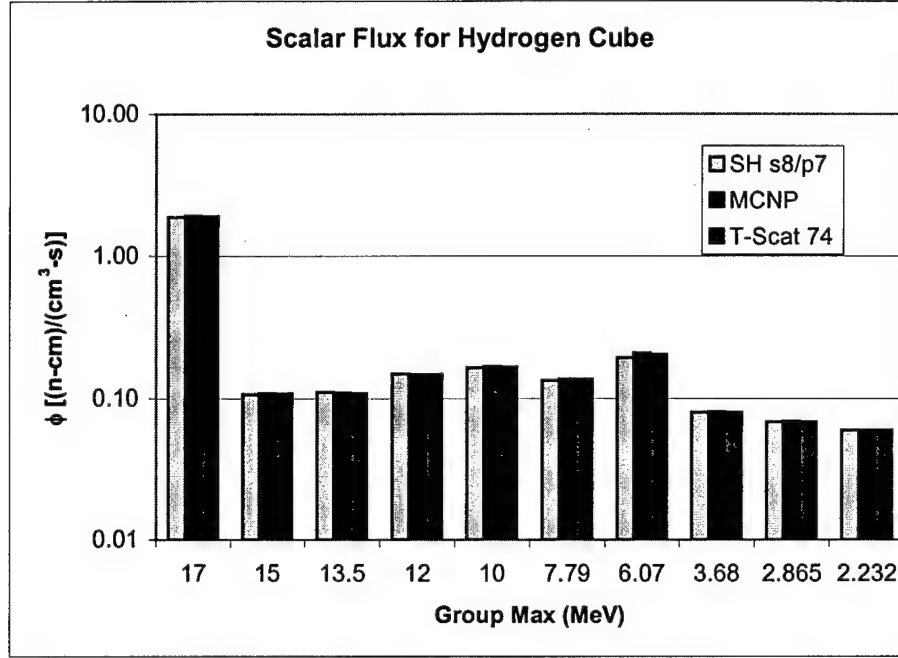


Figure 64. Hydrogen cube test problem comparing volume scalar flux.

Again, as noted above, the uncertainty reported for MCNP is its own reported relative uncertainty. We also provide the 99% confidence level of the MCNP uncertainty ($\varepsilon_{99\%} = 2.58\varepsilon$) for comparison. The differences reported for TETRAN are based on their relative differences to the MCNP value namely

$$\varepsilon_{TETRAN} = 100 \frac{|\phi_{TETRAN} - \phi_{MCNP}|}{\phi_{MCNP}} \% \quad (193)$$

The purpose of reporting these values is to give the reader confidence that the MC facet method performs reasonably well in a transport code. The method is certainly not optimized at this time (particularly in its angular quadrature). The differences should act as a guide in assessing the feasibility

of the MC facet method noting that typical cross section library uncertainties can be on the order of a few percent.

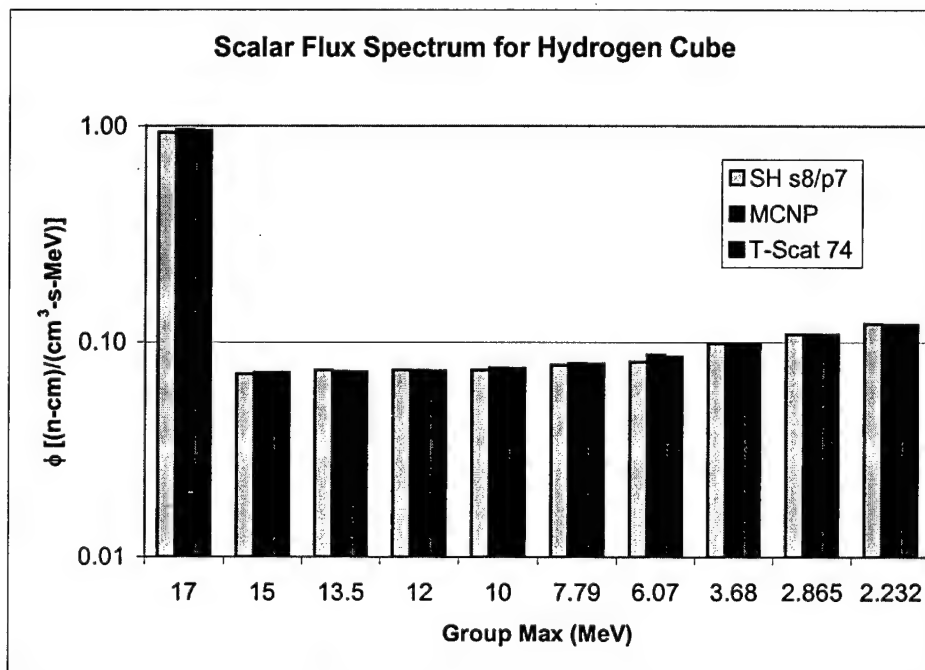


Figure 65. Hydrogen cube volume scalar flux spectrum.

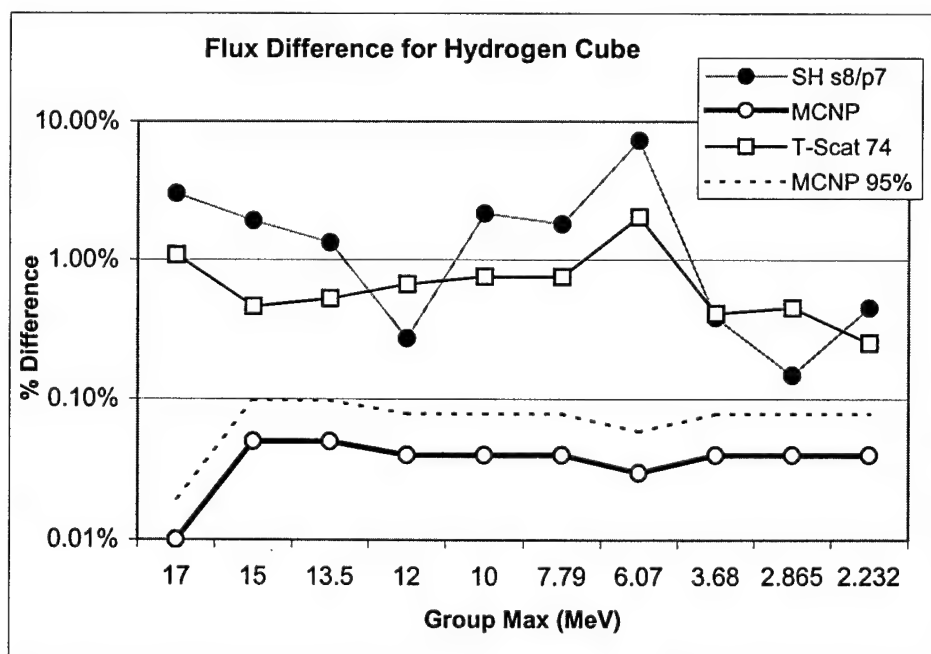


Figure 66. Relative difference between TETRAN methods and MCNP (^1H).

Changes from Angular Quadrature

Figure 66 charts the relative difference of the various methods. Even with six fewer ordinates, the T-matrix library calculated with T-Scat has a generally lower difference than its spherical harmonic counterpart. The lines in the chart are added only for clarity and do not represent any data.

The transport code performance is improved if the number of directional ordinates using T-Scat is increased from six fewer than the S8 to six more. Using a $8 \times 14 \rightarrow 86$ facet structure the new values are shown in Figure 67.

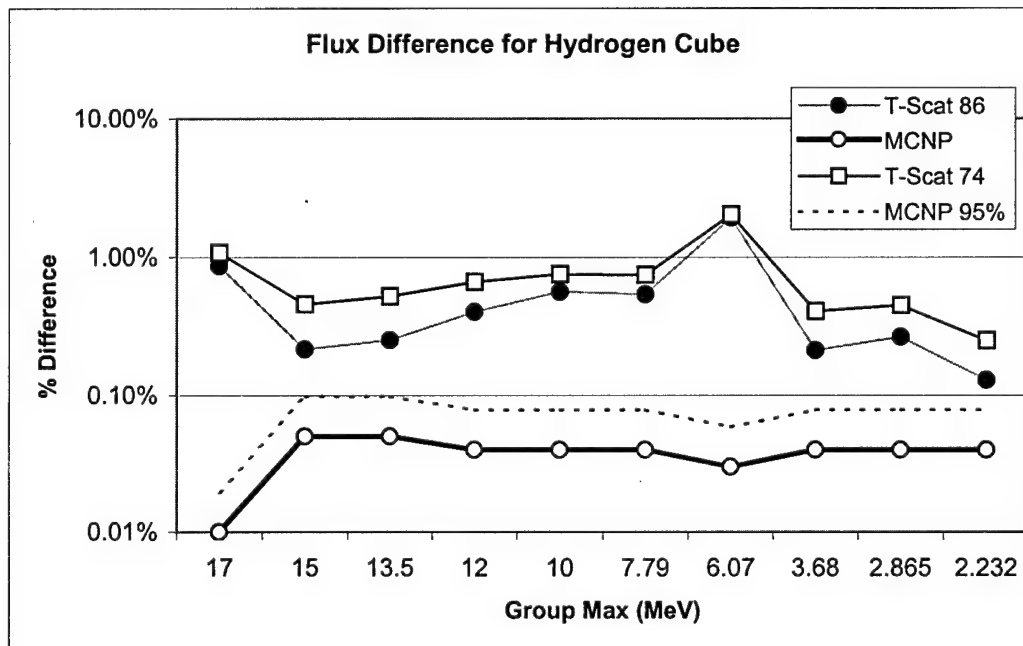


Figure 67. Reducing the T-Scat difference by increasing from 74 to 86 facets.

We continue to examine angular quadratures sets with more ordinates by performing the same type of calculation for ^{10}B . The SH was an S10/P3 and T-Scat used 114 facets. The results are shown in Figure 68 and demonstrate again that T-Scat is providing quality results.

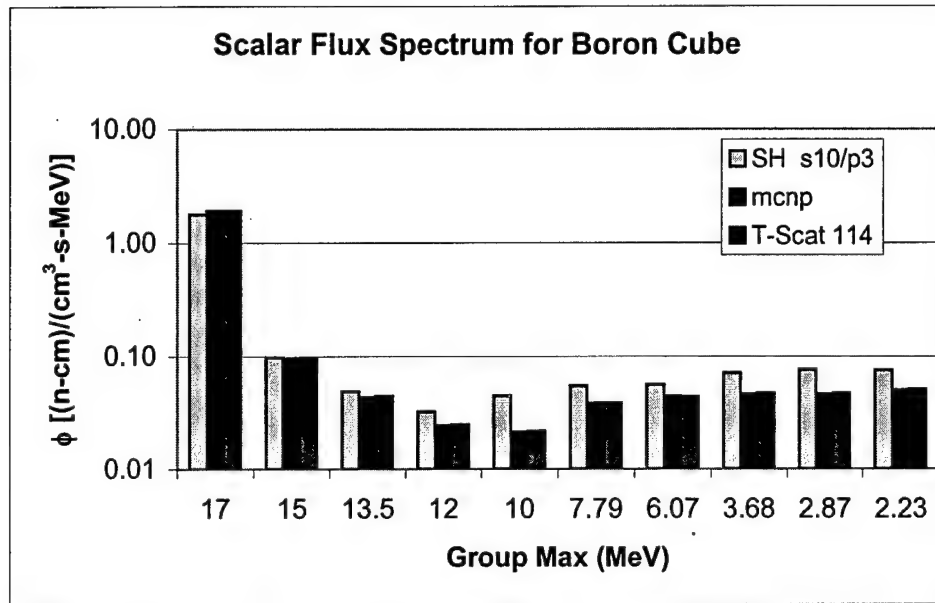


Figure 68. Simple cube for ^{10}B shows marked improvement for T-Scat.

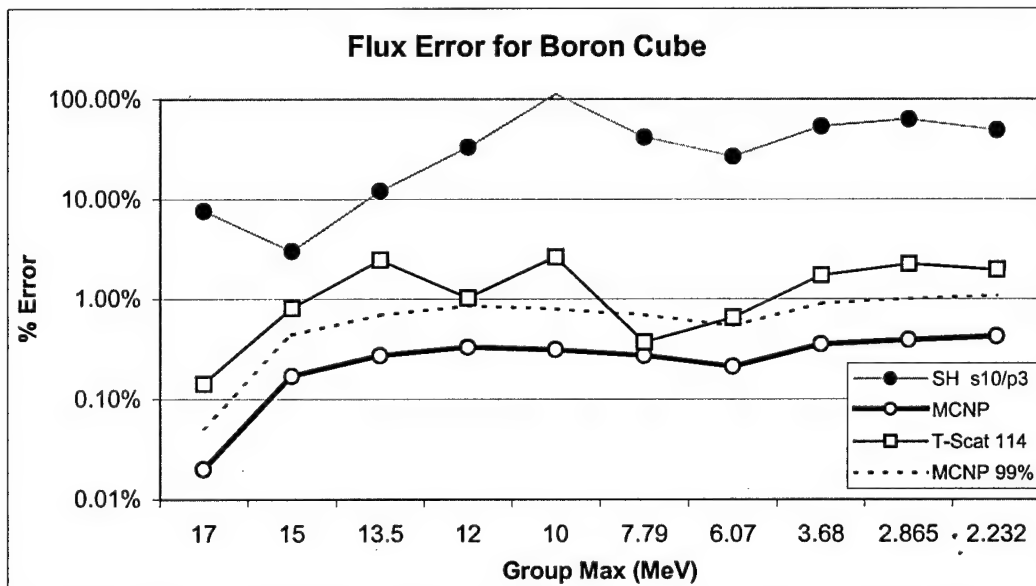


Figure 69. Simple cube for ^{10}B shows marked improvement for T-Scat.

Group Structure Effects

We next examined the hydrogen cube using the finer group structure VITAMIN-J. While both methods under predict the scatter to the next group,

the error for the T-Scat library is again lower than for the spherical harmonic method.

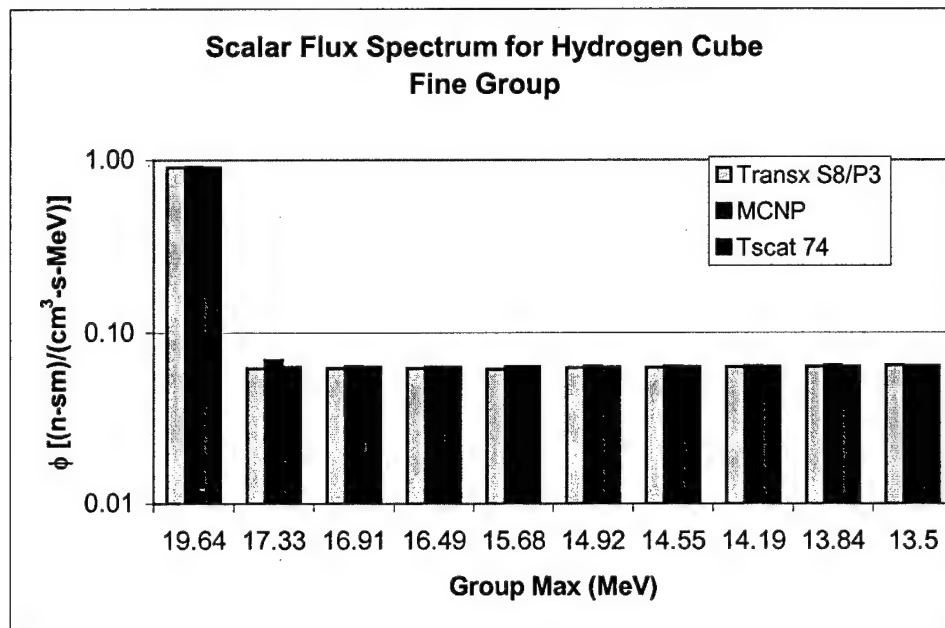


Figure 70. Hydrogen using VITAMIN-J structure.

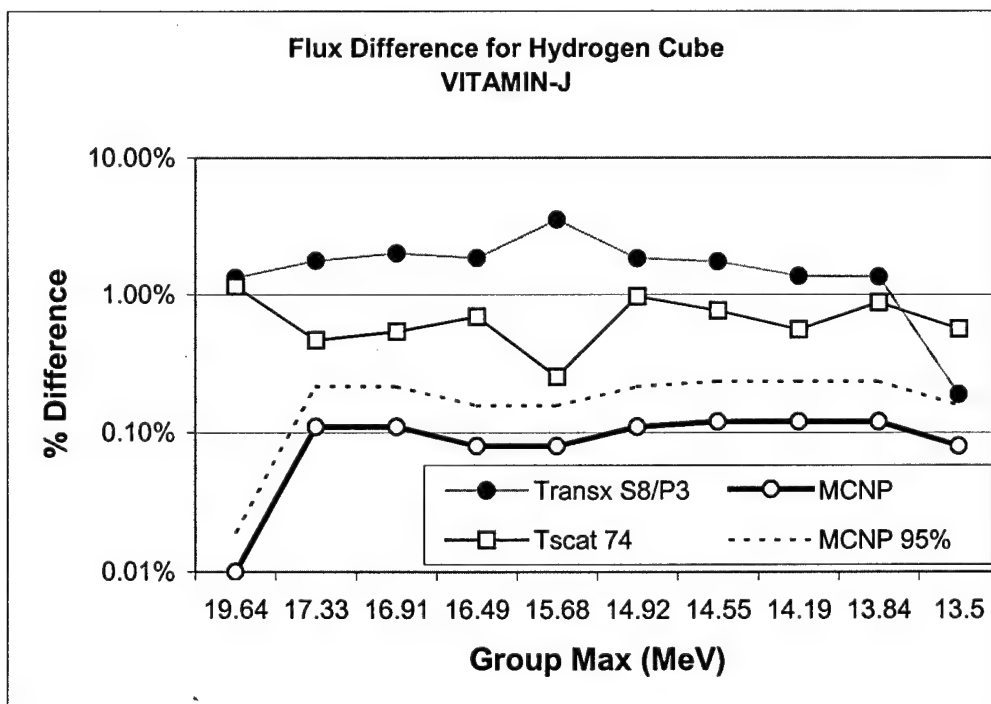


Figure 71. Error of hydrogen 161 cell cube using fine group structure.

Of course reducing the angular quadrature can also impact the error. We next compare an SH S4/P7 with a $6 \times 6 \rightarrow 26$ facet quadrature.

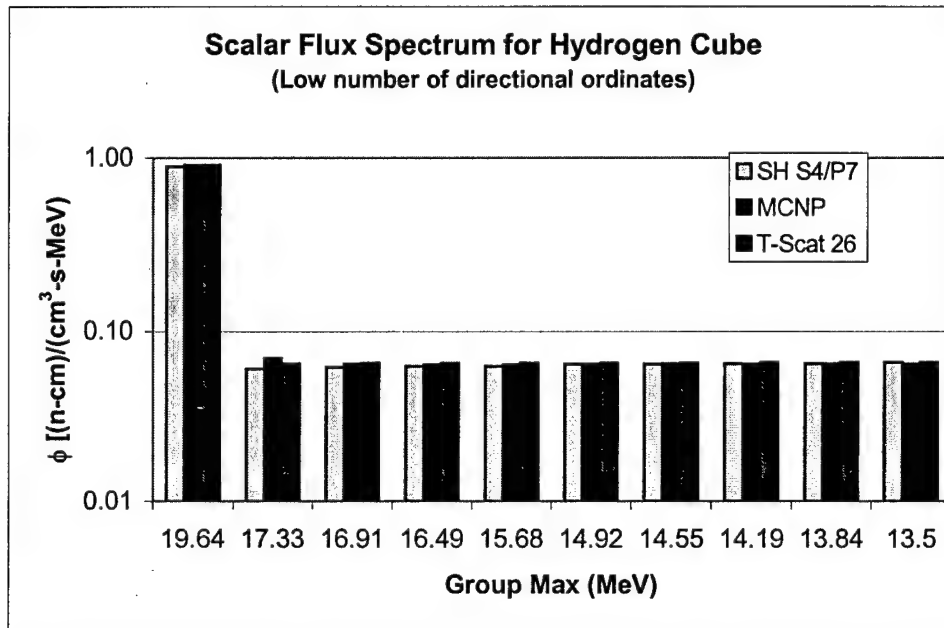


Figure 72. Scalar flux for a small number of directional ordinates.

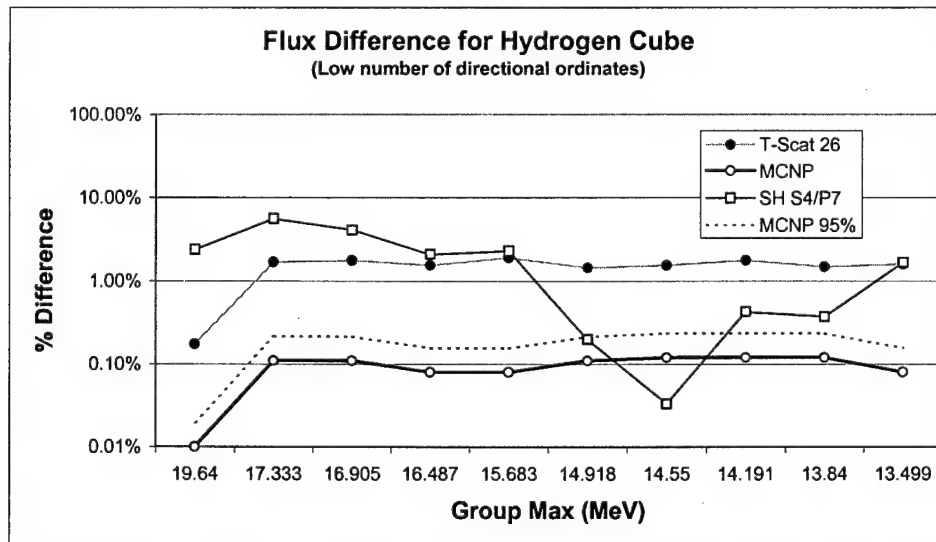


Figure 73. Flux differences for a small number of directional ordinates.

Figure 72 shows the average scalar flux in the cube while Figure 73 shows the differences. Of particular interest is the improved performance of the

facet method in the group below the source group. While both methods under predict the value of the flux in the second group, the facet method does provide about a factor of two improvement.

Spatial Mesh Variations

Next, we look at what happens when the spatial mesh is reduced. As for the angular quadrature reduction, this is done simply to verify appropriate operation of the scattering library. Increasing the number of tetrahedra reduces the relative differences with respect to the MCNP calculation. Such reductions, however, are negligible suggesting that the coarse mesh (161 cells) used previously was sufficiently fine).

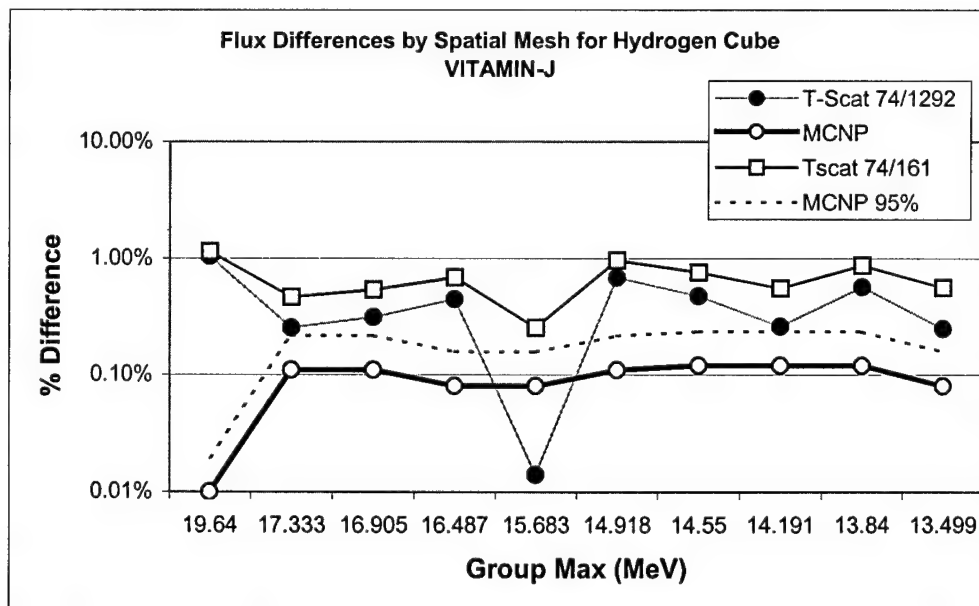


Figure 74. Error reduction using finer spatial mesh.

Introducing the MCSN Method

We next introduce the results from MCSN. This is a new code developed at AFIT²⁵. It is spatially continuous but discrete in angle and energy. As mentioned earlier, it requires a positive scattering matrix to build the cumulative distributions used to sample the scattered energy and facet. Because it uses the exact same T-matrix library as TETRAN (that created by the MC facet method), it is expected that the commonality of being continuous in space would place its answers closer to those of MCNP than TETRAN. In fact, MCSN should give the converged result that TETRAN would approach as the spatial mesh is refined. Like MCNP, MCSN reports its own relative uncertainty. For the calculations presented here, such uncertainty is about an order of magnitude less than the comparable uncertainty of MCNP. Figure 75 shows that the differences between TETRAN and MCSN are slight. A look at the relative differences reveals that our predictions were correct. The MCSN calculation lies somewhat closer to the MCNP result than the TETRAN calculation.

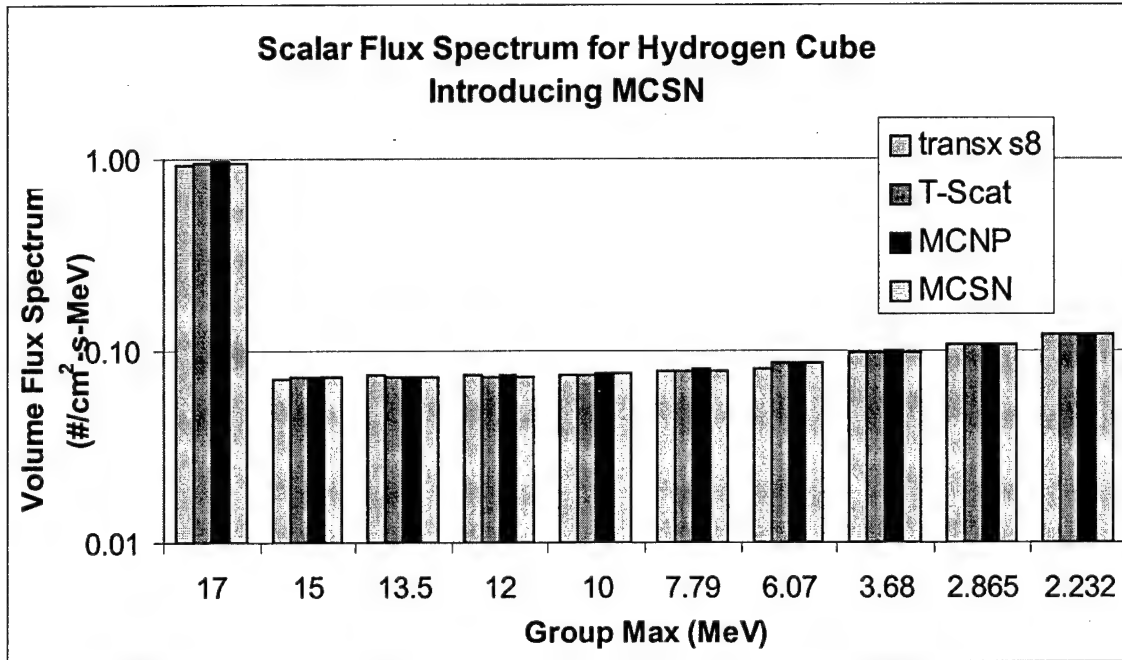


Figure 75. MCSN applied to the 161 cell hydrogen cube.

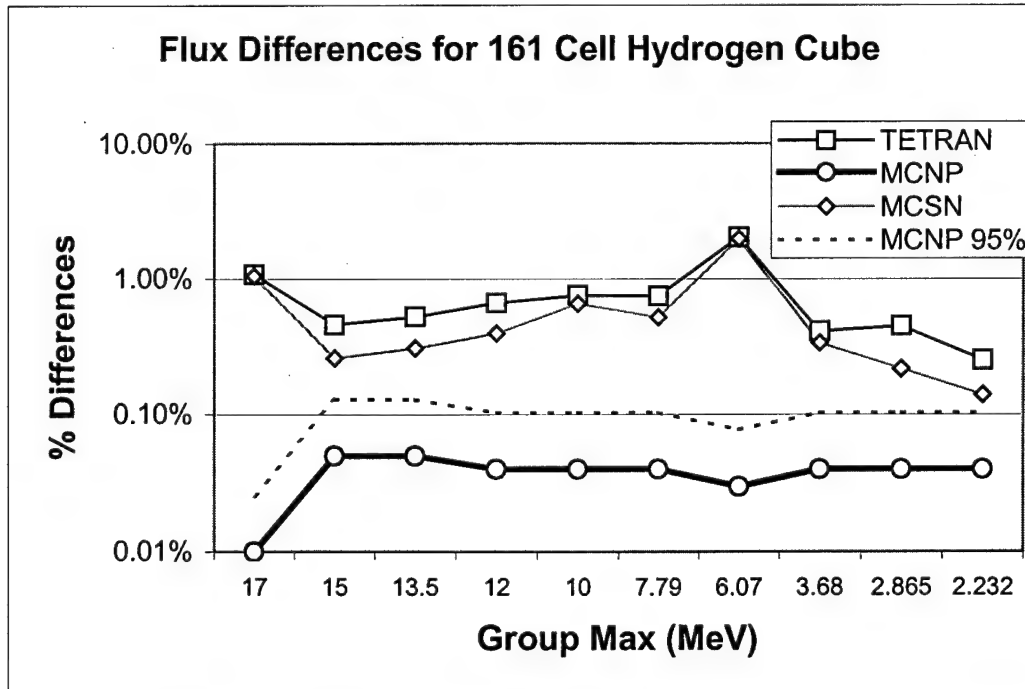


Figure 76. Error of TETTRAN and MCSN methods using T-Scat library.

We can also examine the spatial mesh in a plot similar to Figure 74.

Here, the relative difference between MCSN and TETTRAN is given where

both methods use the same angular quadrature (74 facet) but TETRAN is run using two different spatial meshes as before (161 and 1292 cells). The data is plotted along with the MCNP result in Figure 77.

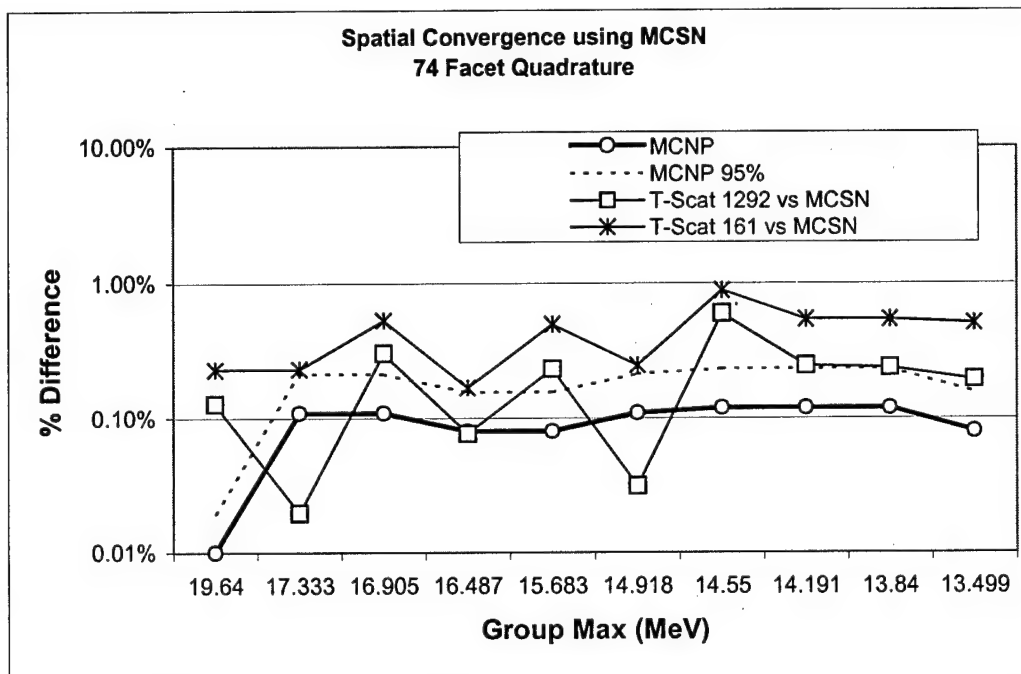


Figure 77. Difference between MCSN and TETRAN for two spatial meshes.

It is not the purpose of this research to demonstrate the capabilities of the MCSN method. Rather, it is to show that the MC facet method has made it possible for such a code to be implemented, and that its results are consistent with expectations. Even with the quadrature limitations imposed on the T-matrix library, results are excellent for the average scalar flux calculations. Similar cube calculations were performed using other nuclides, (^7Li , ^{27}Al , ^{16}O) with similar results. We examine a number of mixed materials next, while exploring other aspects of the T-Scat libraries.

Mixed Nuclides in a Single Material

Does the number of draws taken to calculate the T-matrix impact the results of the transport code? The answer is yes. The same cube geometry above was used. This time the material was Li_2O (1 g/cm^3). Again the material contained an isotropic source of $1 \text{ neutron/cm}^3\text{-s}$. The T-matrix quadrature was 74 facets, and the LANL-30 group structure was used. The matrices were built with 320 thousand, 1.28 million and 5.12 million draws and then run in TETRAN. The draws were independent, each started with different seeds for the random number generator. The error data is compared in Figure 78.

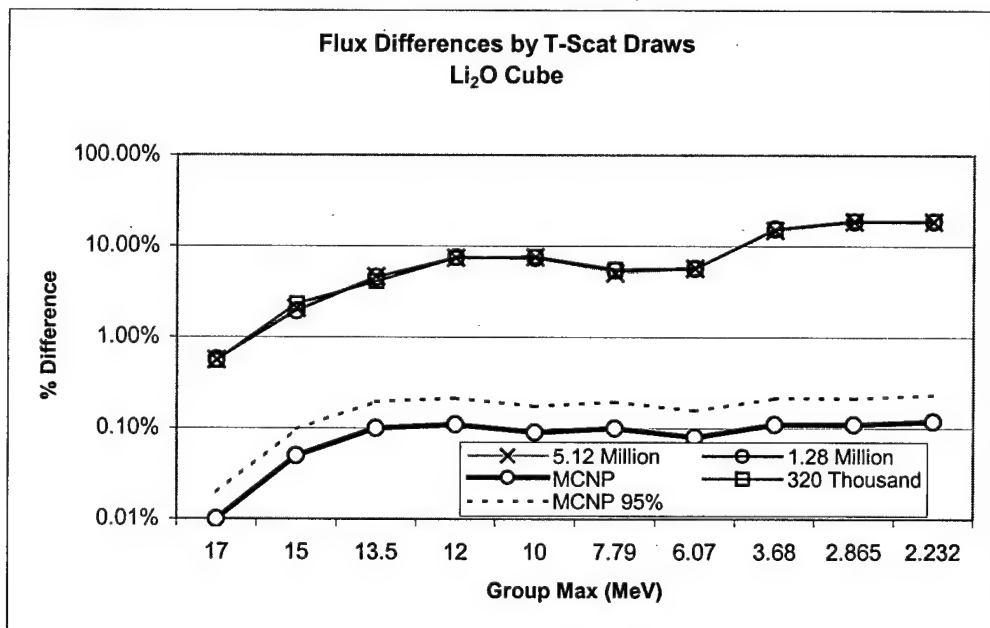


Figure 78. Transport error may depend on the number of draws to calculate the T-matrix library.

For the simple cube, the flux differences are inconsequential. A closer look at the second group's relation to the MCNP solution is shown in Figure 79.

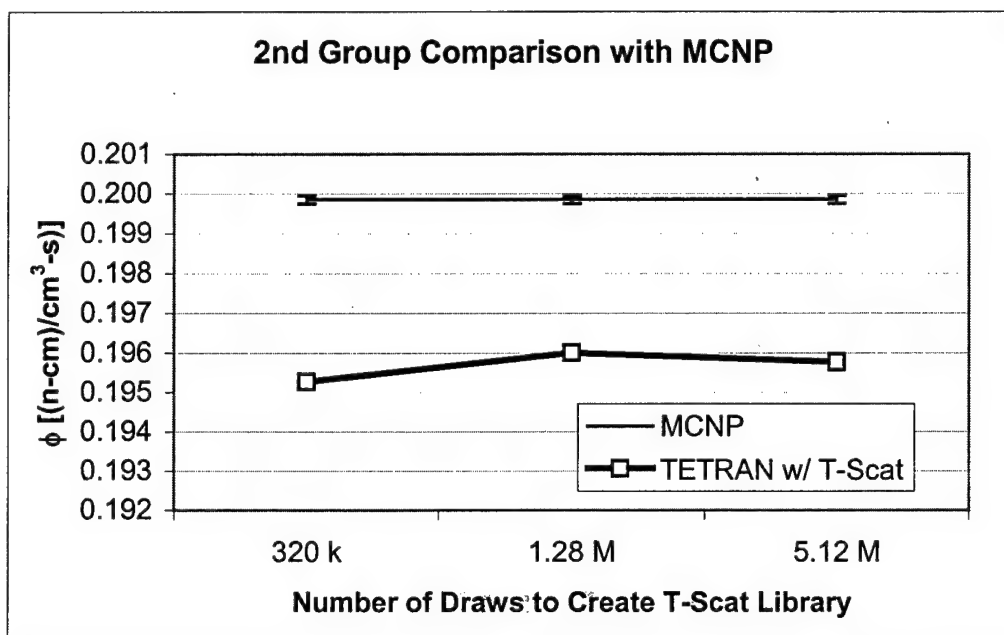


Figure 79. Close look at group two relation to MCNP as the number of draws is increased in creating the scattering library.

The relative error of the MCNP solution was 0.05% and is shown by the error bars in the figure. Typically, we have observed little practical improvement beyond 5 million draws for each incident facet in each incident group. This is true for the scattering matrices used in all of the geometries and mixes tested. Unless otherwise stated, it is the default number of draws taken to calculate the T-Matrix as described earlier.

The next mixture of nuclides examined is the most common -- water. Figure 80 shows the flux calculation for water using the four transport methods discussed earlier. The error calculation reveals results consistent

with what was shown earlier. The MCSN results have a little less error than TETRAN results using T-Scat, which in-turn is less than the errors from the SH S8/P3 calculation.

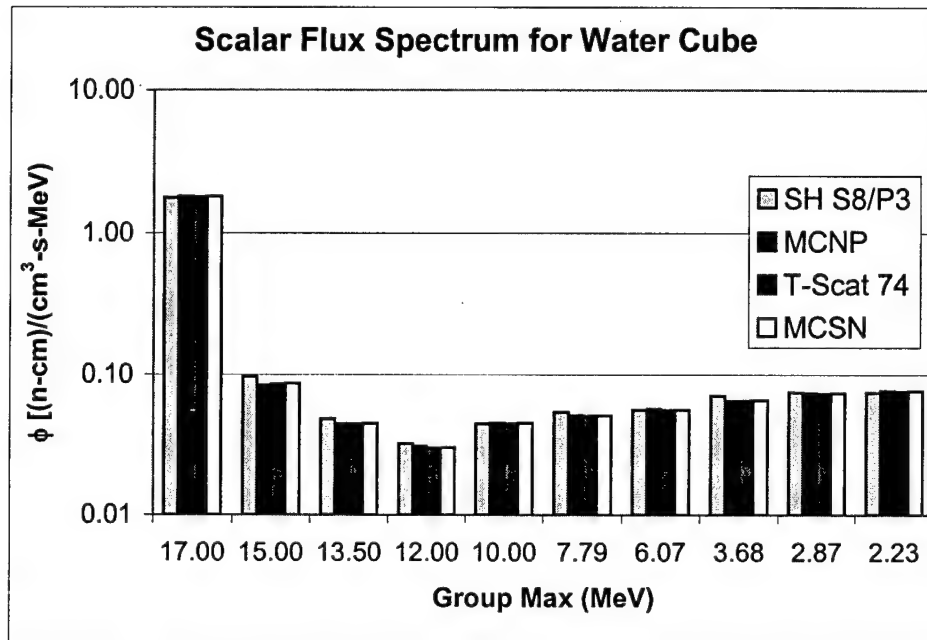


Figure 80. Flux comparisons for the water cube.

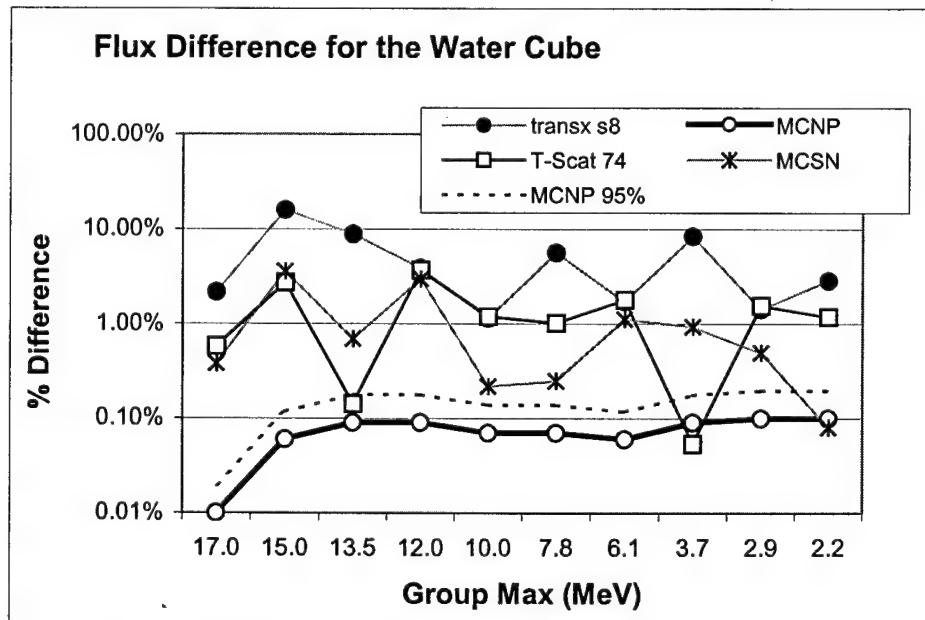


Figure 81. Error of the methods in the water cube.

As mentioned earlier, MCSN, like MCNP, reports its own relative uncertainty. Figure 82 shows how the two compare for the previous example.

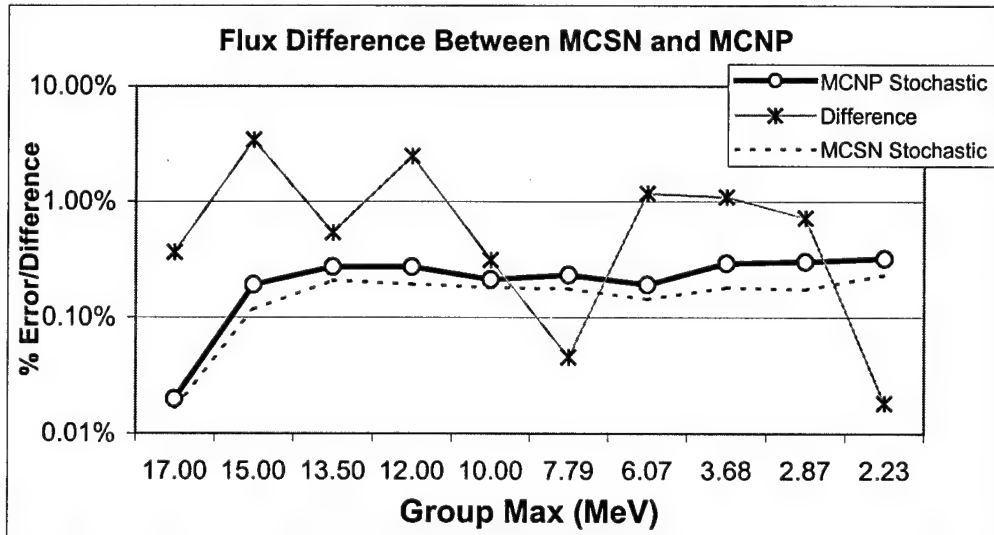


Figure 82. Stochastic errors of MCSN and MCNP in the H₂O cube.

Rebalance Effects in the Transport Process

As previously discussed, it is expected that rebalancing the first angular moment of the scatter would have little impact on high energy problems. The rebalance is meant primarily for diffusion like problems. Figure 83 shows that this is indeed the case. Angular rebalance for this problem made essentially no substantive changes to the scalar flux calculations of the transport code.

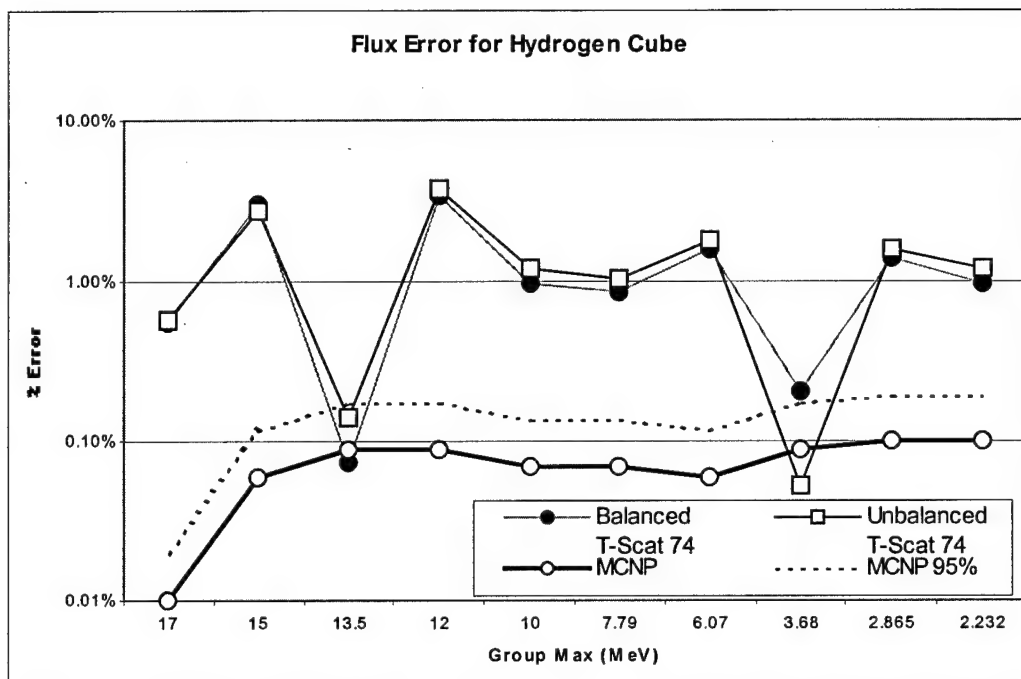


Figure 83. Effects of rebalancing 74 facets for the hydrogen cube.

Currents and Quadratures

The level symmetric quadrature used here for the spherical harmonic expansions provides no preferential treatment for any axis. The ordinate directions are invariant to 90° rotations about any axis. Current measurements on cube faces should, therefore, have essentially the same values. Unfortunately, the spatial mesh used for the TETRAN code does not have this same property. There does exist some variation of currents on the cube faces because of the variation in the spatial mesh. The Cartesian quadrature (with pole caps) used for the facet quadratures also has no such symmetry. It is invariant to rotations about the z -axis only, and to reflections across the x - y plane. Hence, for a cube with no spatial mesh asymmetries,

currents should be the same for the x^+ , x^- , y^+ , and y^- faces of a cube, but may be different from the z^+ and z^- faces. The partial current in the $+x$ direction is

$$J_x^+ = \sum_{[\hat{e}_x \cdot \hat{\Omega}_n > 0]} w_n (\hat{e}_x \cdot \hat{\Omega}_n) \psi_n \quad (194)$$

with \hat{e}_x the unit normal in the positive x direction. The same equation holds for the other directions. For an isotropic source near the center of the cube and equal quadrature weights (w_n) the only variability is in the magnitude of $(\hat{e}_x \cdot \hat{\Omega}_n)$. For the 74 facet quadrature,

$$\sum_{[\hat{e}_x \cdot \hat{\Omega}_n > 0]} (\hat{e}_x \cdot \hat{\Omega}_n) = \sum_{[\hat{e}_y \cdot \hat{\Omega}_n > 0]} (\hat{e}_y \cdot \hat{\Omega}_n) = 18.7, \quad (195)$$

and
$$\sum_{[\hat{e}_z \cdot \hat{\Omega}_n > 0]} (\hat{e}_z \cdot \hat{\Omega}_n) = 18.8. \quad (196)$$

This suggests a bias in the quadrature that will increase the z currents such that, for the cube geometry

$$J_z^+ = J_z^- > J_x^+ = J_x^- = J_y^+ = J_y^- . \quad (197)$$

With such a bias, we expect the integral current out the $\pm z$ faces of the cube to be larger than the integral current out the $\pm x$ and $\pm y$ faces of the cube. These integral values are reported in TETRAN's summary file. The results

for the 161 tetrahedron water cube are presented in Figure 84 and Figure 85.

Here, the 1st and 2nd group currents are shown.

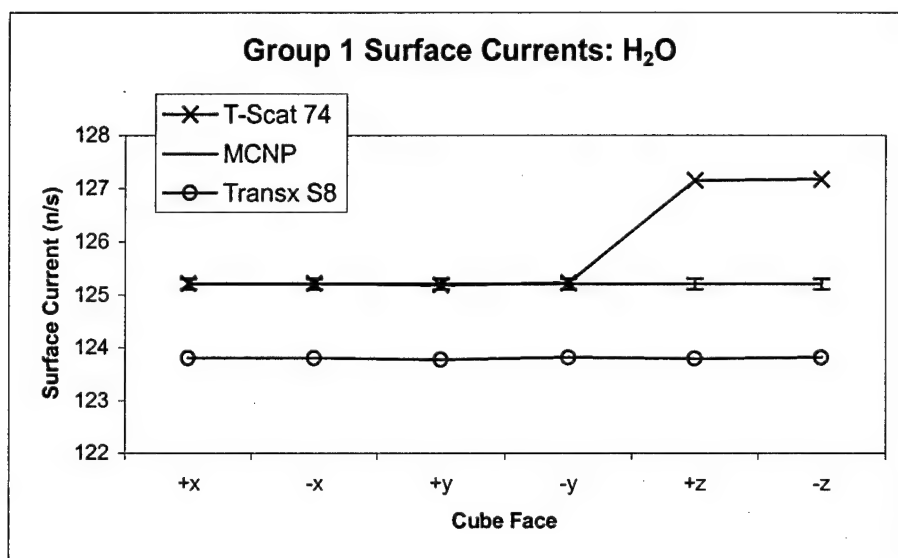


Figure 84. Total group 1 cube surface currents of H₂O cube show asymmetry in facet quadrature.

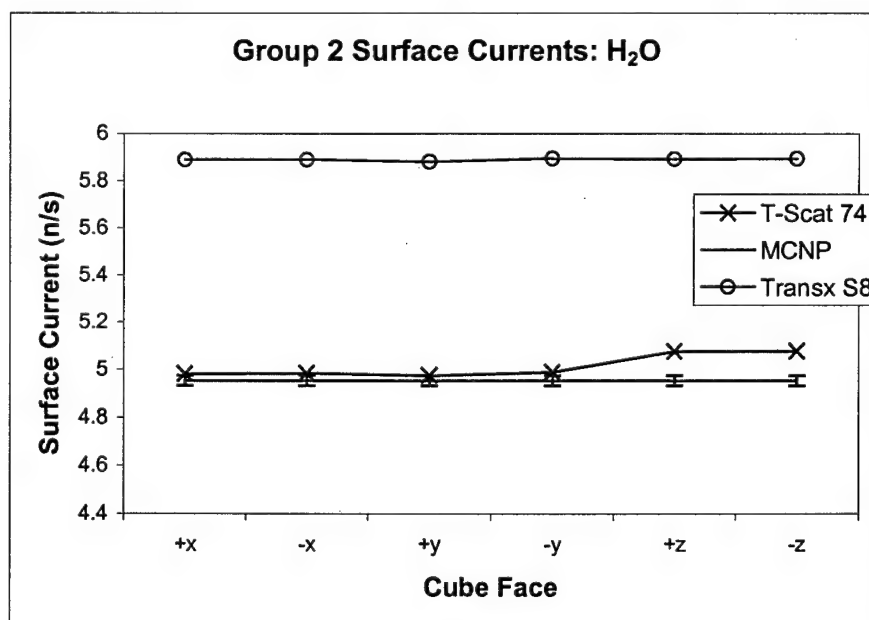


Figure 85. Total group 2 cube surface currents of H₂O cube show asymmetry in facet quadrature.

The figures show that level symmetric quadrature does produce relatively uniform currents through the six faces suggesting the primary variation of the T-Scat method is due to the angular quadrature. The facet quadrature, however, results in a predictable difference between the azimuthal faces (x and y) and polar (z) faces. For the most part the T-Scat data gives better agreement to the MCNP calculation.

To investigate other aspects of the MC facet method for anisotropic scatter and its implications for use in sample transport problems, a more complicated geometry is needed. Beyond demonstrating the efficacy of the method, we'll also demonstrate, for the first time, the use of the EC transport using multi-group anisotropic scattering matrices.

Nested Cube Test Problems

These problems are based on a test problem used by Miller⁷. The geometry is three cubes, nested centrally as shown in Figure 86. There are three regions:

- A. Source region--within innermost cube (material 1).
- B. Middle region--annulus between innermost and middle cube (material 2).
- C. Outer region--annulus between middle and outer cubes (material 1).

In this section we present results for two material combinations: Water-Iron-Water and Water-Boron-Water. In so doing, we will demonstrate the

use of multiple materials, developed by T-Scat, for use in the same transport problem. We include the use of a library consisting of mixed nuclides for water using 1_1H and $^{16}_8O$ data. Finally, we also examine the effects of deep penetration and have the opportunity to demonstrate (for the first time) the EC method using anisotropic scatter.

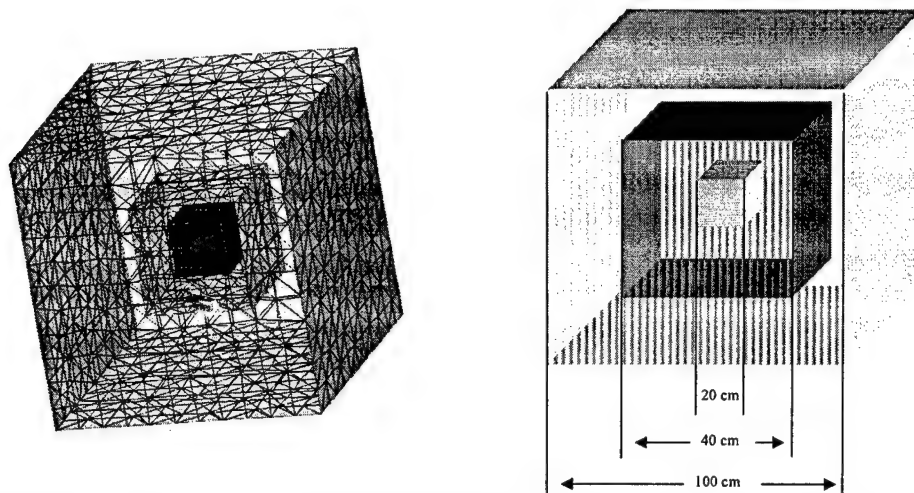


Figure 86. Mesh and dimensions of the cube-cube-cube geometry.

We first examine the water-iron-water problem. For simplicity, H_2O (as described above) and the single nuclide ^{56}Fe are the materials used.

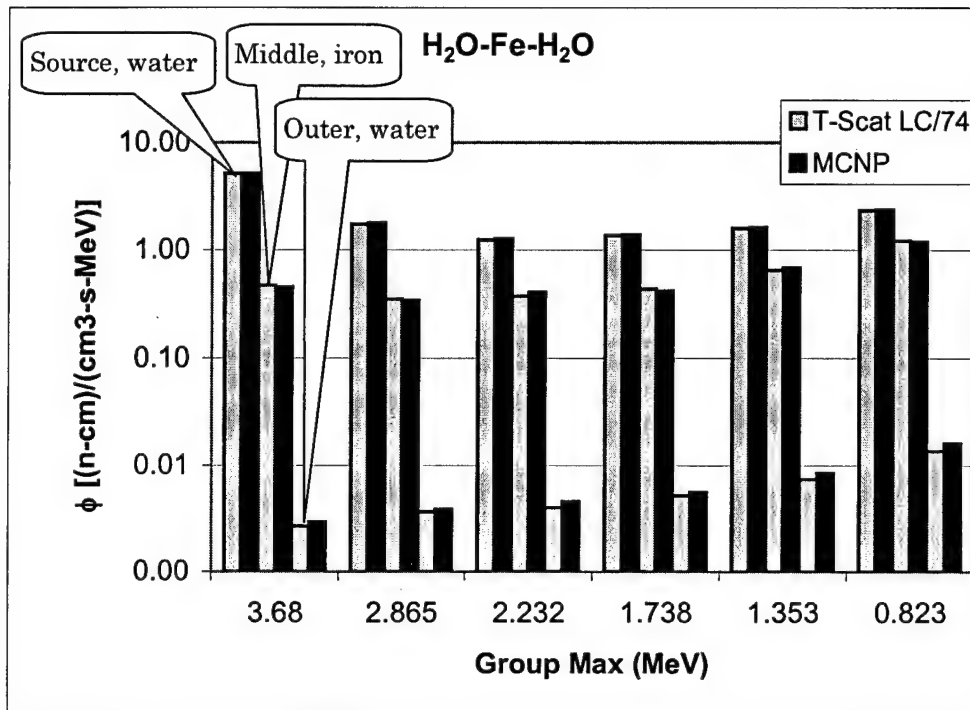


Figure 87. Water-iron-water fluxes for six groups.

The effects of the penetration through the shield are shown for each group in sequence. To avoid unsupported scatters, the source emits uniformly in group 8 of the LANL-30 group structure (2.865-3.68 MeV). The various methods (MCNP, TETTRAN, etc.) are placed side by side for direct comparison. Differences with MCNP, as before, are shown as line charts. Figure 88 gives a quick look at the differences for this problem using the T-Scat library, and TETTRAN's LC spatial quadrature on 528 spatial cells and 74 facets (or S_8). Detailed comparisons with MCNP for each region are shown later.

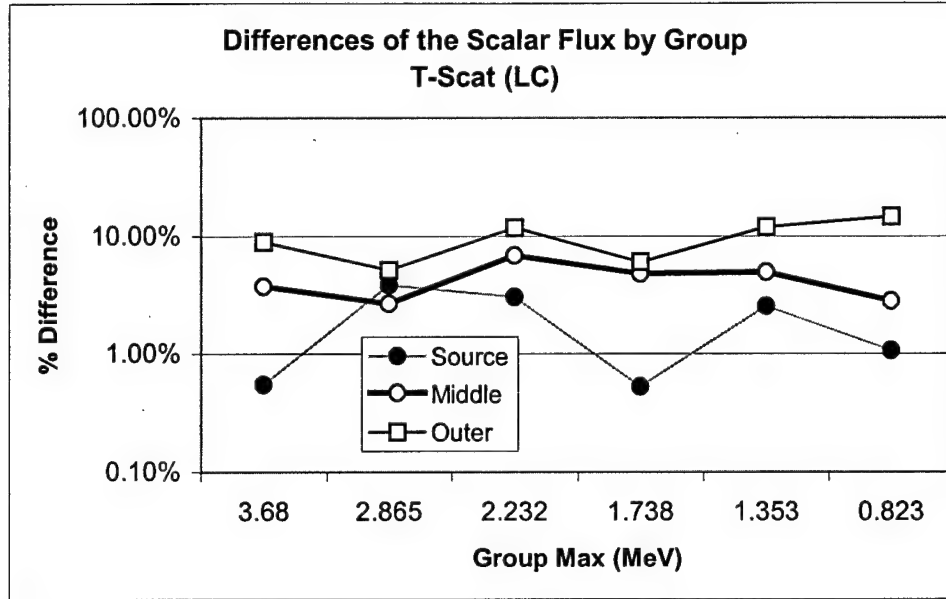


Figure 88 Presentation of H₂O-Fe-H₂O differences with MCNP by region.

The optical thickness of the cells plays an important role for this problem.

The optical thickness of a cell is

$$\varepsilon = \sigma(\text{cm}^{-1})l(\text{cm}) \quad (198)$$

where σ is the macroscopic total cross-section, and l is the distance a neutron travels to cross the tetrahedron. The exponential characteristic method was designed to handle optically thick cells. The average optical thicknesses for the tetrahedra in this problem are shown in Table 5.

Table 5. Average cell optical thickness for H₂O-⁵⁶Fe-H₂O system.

Group (MeV)	Water/Source	⁵⁶ Fe (7.86g/cm ³)	Water/Outer
3.68 - 2.865	1.96	3.233	5.016
2.865 - 2.232	1.75	3.173	4.482
2.232 - 1.738	2.238	2.935	5.723
1.738 - 1.353	2.619	2.743	6.699
1.353 - 0.823	3.664	2.462	9.372

The iron region has cells on the order of a few mean free paths thick, with the exterior water tetrahedra even thicker. The errors shown in Figure 88 were for the TETRAN linear characteristic spatial quadrature for each region. In Figure 89 to Figure 91, three different methods are compared in each region.

All the methods were run on TETRAN and are compared to the MCNP solution with a relative uncertainty as shown. A spherical harmonic (SH) method with an S8 quadrature using a P3 expansion was run using the LC method. Note that SH methods can create negative fluxes independent of the spatial quadrature used. When this happens, the EC method fails to run. The other two methods used the same T-Scat library employing the LC and then the EC method for direct comparison of the multigroup anisotropic behavior.

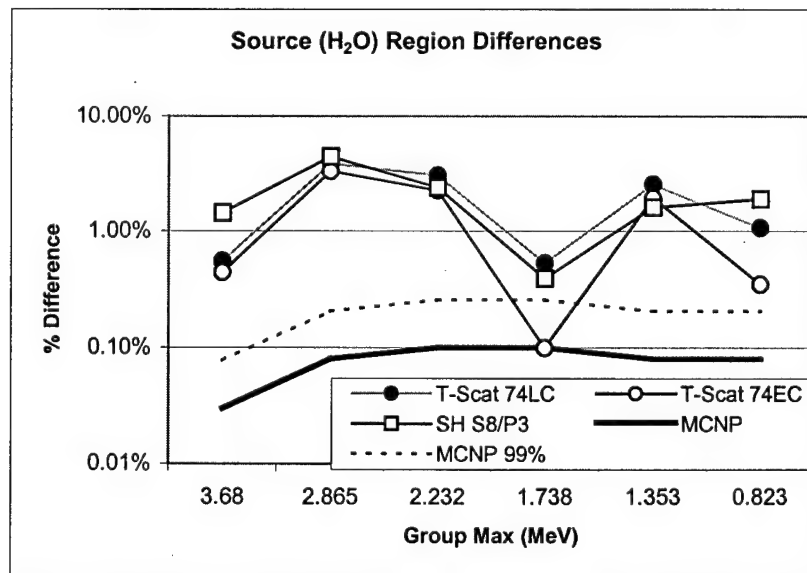


Figure 89. Relative difference in source region of H₂O-Fe-H₂O problem to MCNP solution.

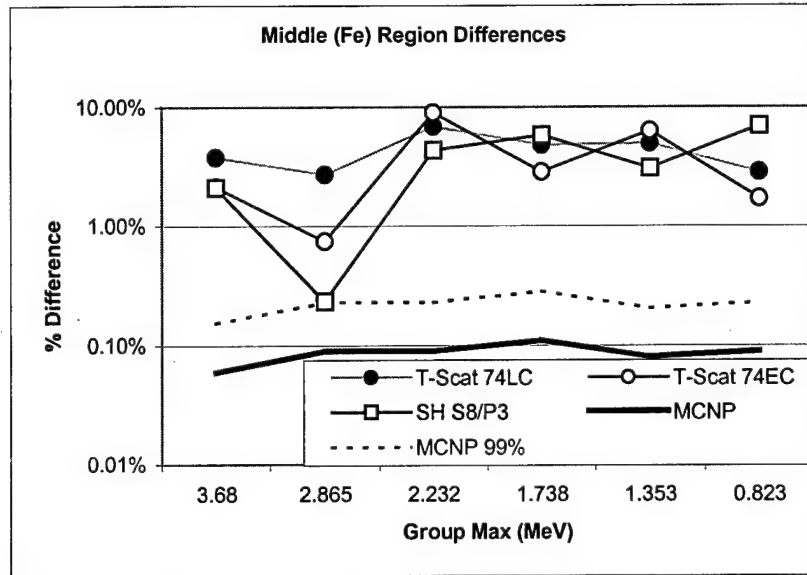


Figure 90. Relative difference in middle region of H₂O-Fe-H₂O problem to MCNP solution.

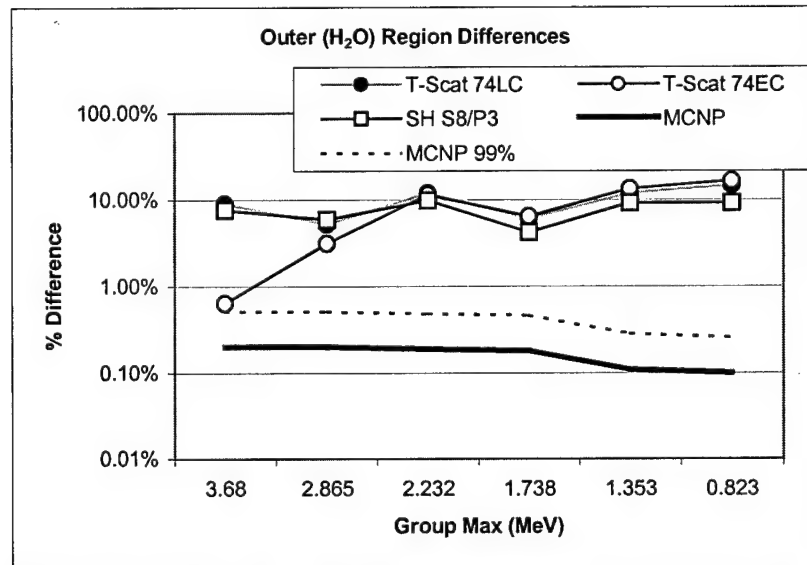


Figure 91. Relative difference in outer region of H₂O-Fe-H₂O problem to MCNP solution.

This is the first time that the exponential characteristic method has been used with multi-group anisotropic scattering. In the source region, the T-Scat libraries perform well in the first group, and then all the methods are comparable. In the iron region the SH method is markedly better in the second group than T-Scat using LC or EC. Finally, in the region with the thickest tetrahedra, both LC methods are comparable while the EC method is about ten times better in the source group and half the error in the second group.

It is expected that the EC method would perform best in those regions where the cells are thickest. And again the EC method can't be used with spherical harmonics because of the creation of negative sources. The result for the flux in group 1 (which is the group in which the source emits) is most like a deep penetration problem, because the source is in the inner box. Lower groups have downscatter sources distributed spatially throughout the problem. Looking at Figure 91, we see that indeed the EC method performs much better than the other methods in the source group. Still, one might be tempted to use the LC method and tolerate the differences in error. While the EC method will fail if a negative source is encountered, the LC method will include it in its and continue on. The end result can be a negative flux calculation, which is nonsense. This is demonstrated with the next problem.

Again the triple cube geometry is employed. This time the materials are water, boron (^{10}B) and water, with the boron density being 10 g/cm^3 . This

density is used to enhance the cell optical thickness for the same mesh as used earlier. The average cell optical thicknesses are again shown in Table 6.

Table 6. Average cell optical thickness for H₂O-¹⁰B-H₂O system.

Group (MeV)	Water/Source	10B (10g/cm ³)	Water
17.0 - 15.0	.828	9.852	2.118
15.0 - 13.5	.882	9.910	2.255
13.5 - 12.0	.903	10.00	2.310
12.0 - 10.0	.946	10.02	2.421
10.0 - 7.79	.970	10.07	2.480

Compared to the thicknesses of the previous problem, the water tetrahedra are thinner. This is because of the higher energy groups used. This increase in energy also increases the anisotropy of the problem. Figure 92 shows the scalar flux for the problem regions found with T-Scat LC and EC methods.

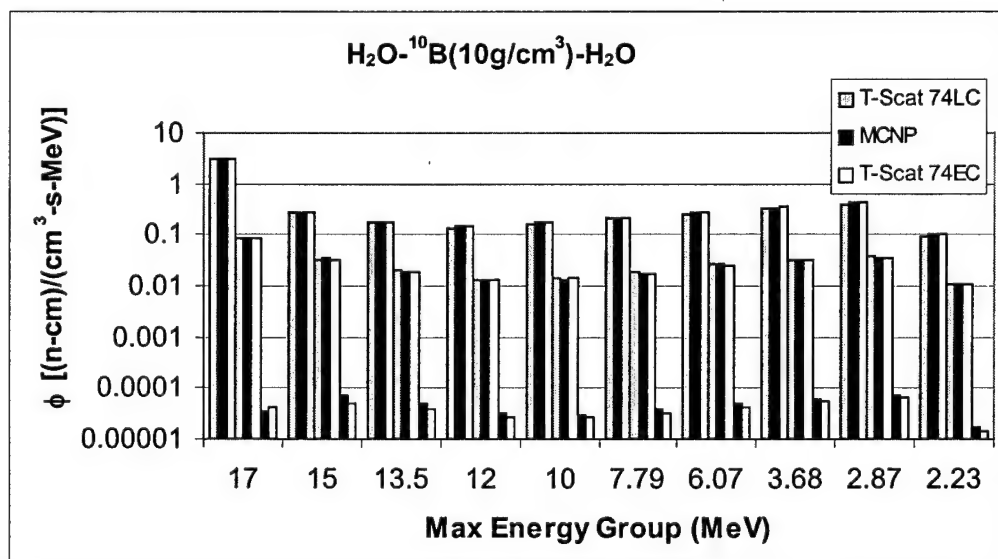


Figure 92. H₂O-B-H₂O: LC produces negative fluxes in the outer region.

For the water-iron-water problem the scalar flux was reduced by about three orders of magnitude through the shield region. Here, the reduction is

five orders of magnitude. For this problem, the LC method produced negative scalar fluxes in the outer water region using both the SH and T-Scat libraries. Hence, only the EC method provided positive results for the external region. And, of course, EC requires a strictly non-negative scattering matrix provided by the MC facet method (SH fails in this regard).

As for the water-iron-water problem the errors are shown in the figures below. Here, the LC and EC methods are compared except in the outside water region where the LC methods failed to provide positive results. Instead, a finer spatial mesh was used (1068 tetrahedra). Again the LC methods produced negative results, but the overall errors in the outer region were reduced.

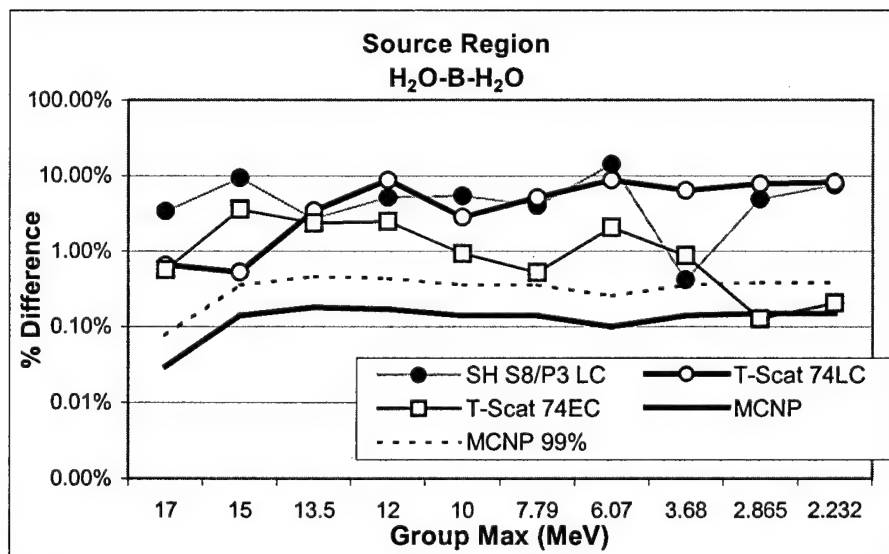


Figure 93. Scalar flux differences of source region relative to MCNP for the $H_2O-^{10}B-H_2O$ problem.

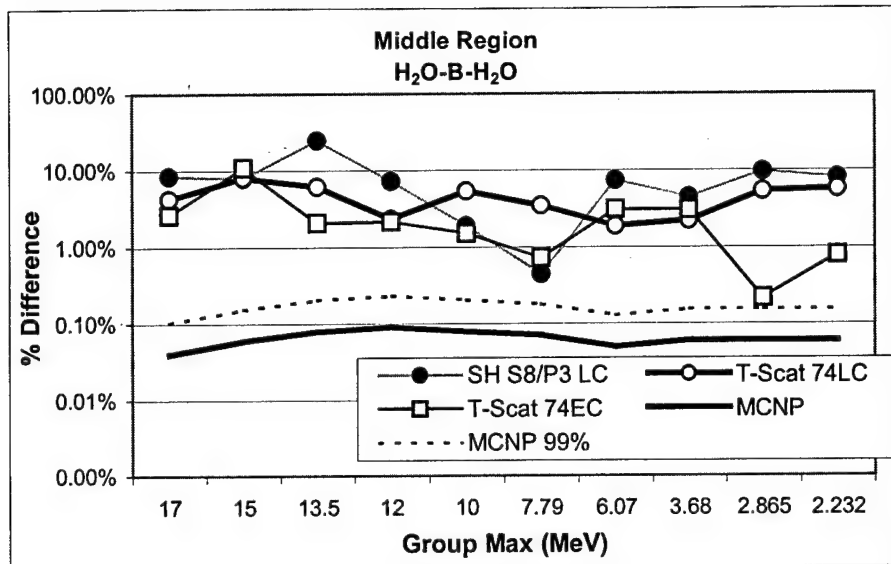


Figure 94. Scalar flux differences of middle region relative to MCNP for the H₂O-¹⁰B-H₂O problem.

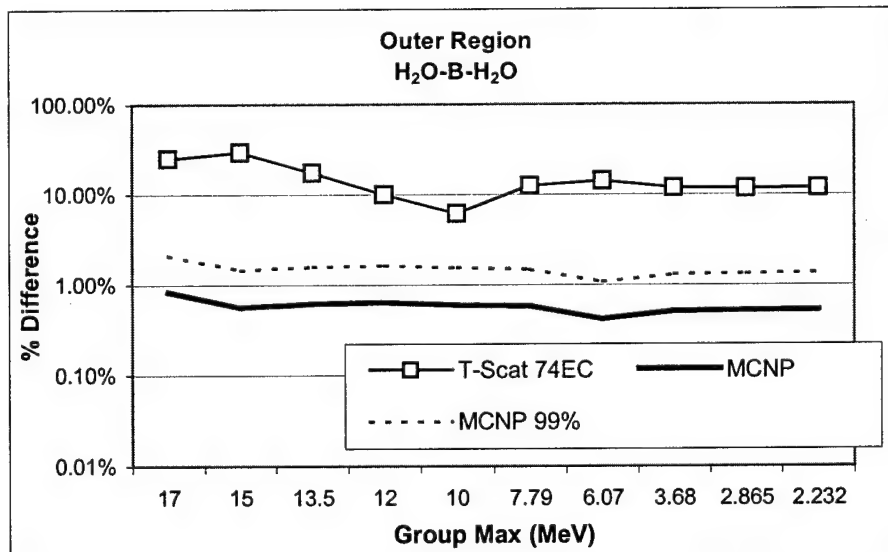


Figure 95. Scalar flux differences of outer region relative to MCNP for the H₂O-¹⁰B-H₂O problem.

While the errors in the external region are high in the first energy groups, examination of Figure 92 shows that the EC method has done an excellent job in tracking with the MCNP solution for the deep penetration problem

considering the substantial attenuation of the flux. A further advantage of the discrete ordinates method is that it can provide a profile of the flux (dependent on the refinement of the mesh). It is possible to take a closer look at exactly where the flux goes negative for the LC problem by using this ability.

I developed a simple plotting routine that, for a given point in space, determines the closest tetrahedron center and reports that tetrahedron's scalar flux. Figure 96 plots the group 1 scalar flux along the x-axis passing through the center of the problem. The charts are expanded to show the negativity just as the exterior water region is entered. The EC method maintains positivity for this problem throughout.

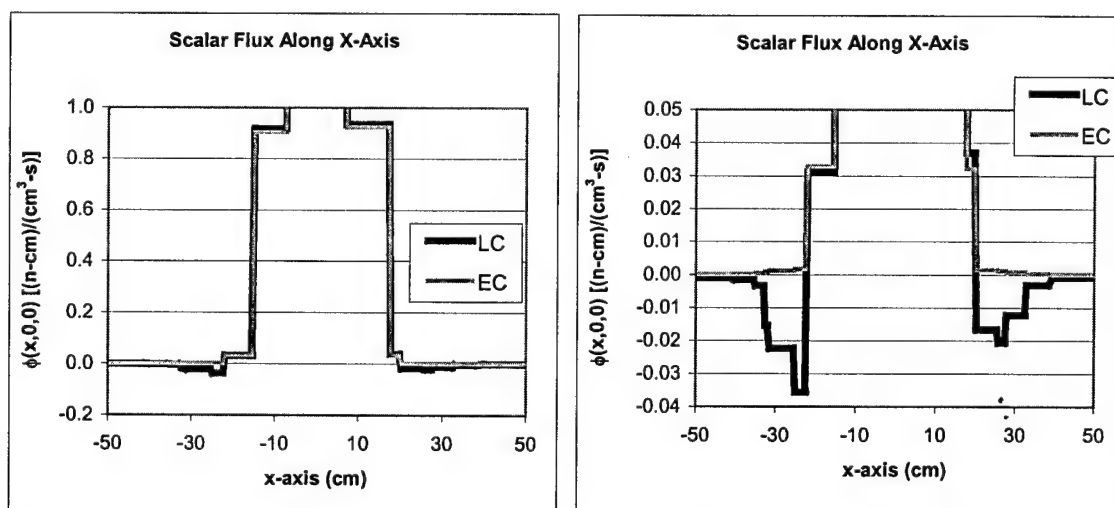


Figure 96. Scalar flux map of the tetrahedra along the x-axis of the water-boron-water problem. LC method fails to maintain positivity.

Plotting the EC method alone on a log scale shows the moderating effect of the water in the external region. This is shown in Figure 97 for the first group (15.0-17.0 MeV) and the 10th group (2.232-1.738 MeV).

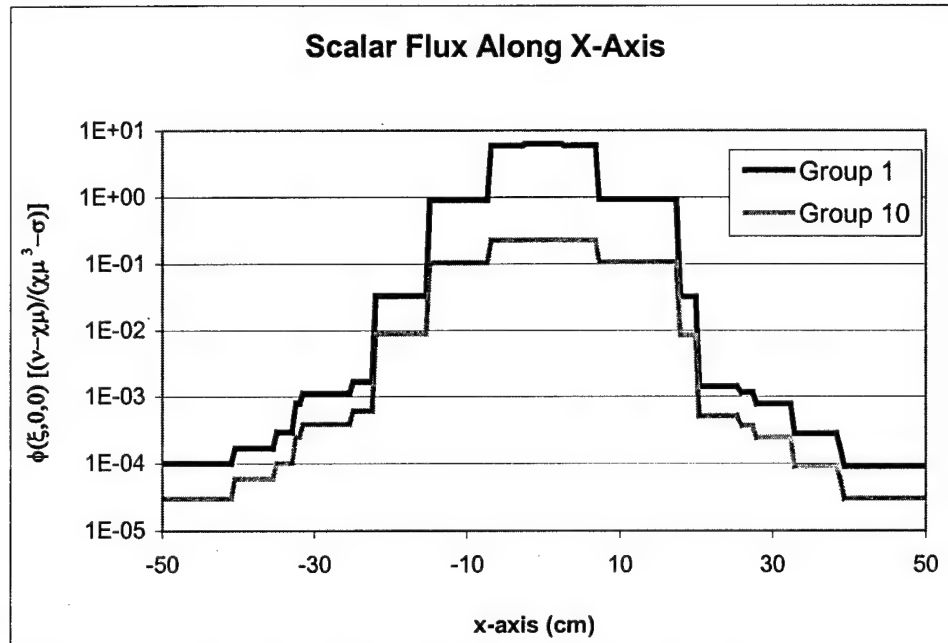


Figure 97. Scalar flux from TETTRAN's EC method for the water-boron-water problem.

Returning to the water-iron-water problem, we apply the same type of chart along the outside surface of the cube to get a profile of the flux at the surface (comparing the spherical harmonic and T-Scat methods). Recall that here the scalar flux was positive for the exterior region. Figure 98 shows that at the corners of the cube the scalar flux was actually negative. Referring to Figure 87, the flux using the LC method was reported as positive, but lower than the MCNP result in the external region across all groups.

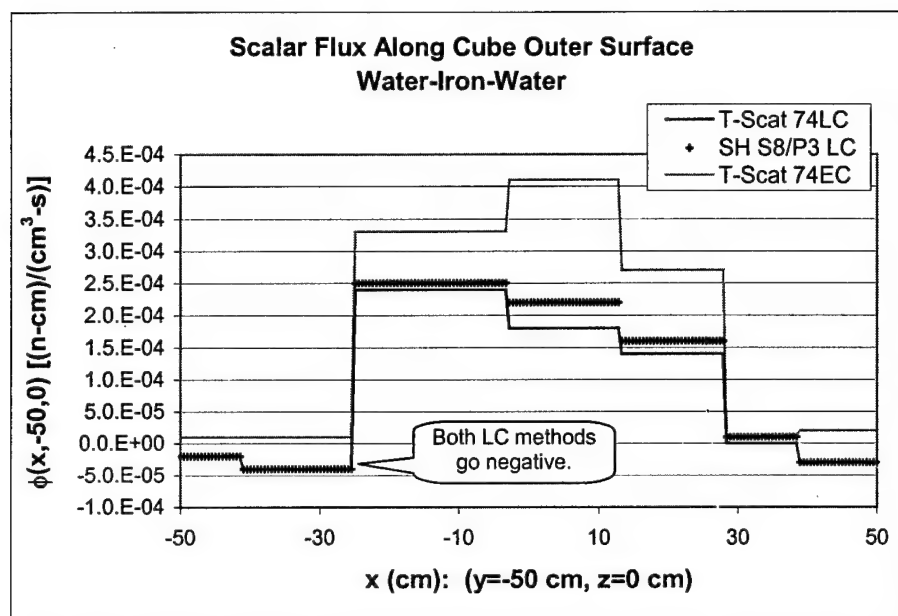


Figure 98. Scalar flux goes negative for water-iron-water problem too.

The scalar fluxes reported by the EC method are not reduced by the non-physical negative flux results obtained using the LC method.

Transport Summary

This chapter has presented only a representative number of materials tested with scattering matrices created using the MC facet method. Its purpose was not to validate the TETRAN code, but rather to demonstrate the viability of the non-negative cross-section libraries we've created. We've shown in particular:

1. a general reduction in scalar flux errors (as compared to SH methods) for comparable quadratures,

2. particular improvement over SH methods with small numbers of ordinates,
3. ability of the MCSN code to use T-Scat multi-group anisotropic scattering data,
4. comparable to better performance (than SH methods) for fine energy groups (noting that ordinate-to-ordinate methods lack angular support for such group structures),
5. the ability to use single, mixed and multiple materials, and
6. the ability to use the EC method on deep penetration problems
 - demonstrating overall superior performance to LC/SH methods and
 - guaranteeing flux positivity with non-negative cross-section matrices.

These observations, together with those of Chapter 9 demonstrate that the MC facet method is a viable technique for general use in discrete ordinates (and MCSN) transport codes.

11. Conclusions

Since the 1970's researchers in the transport community have recognized the problem with the use of spherical harmonics to approximate the scattering source. Such harmonics can create negative sources which, in turn, create non-physical negative fluxes. This research has shown how such fluxes negatively impact the calculation of the scalar flux. In particular, negative fluxes can cause catastrophic failure of transport codes employing the exponential characteristic (EC) method. Such characteristic methods have only been developed within the last few years (here and at the national labs) to make the study of deep penetration problems feasible with the discrete ordinates method. The inability of such methods to perform multi-group, anisotropic scattering because of the negativity of spherical harmonics has only added to the requirement that a new method be developed.

A number of attempts have been made, some quite recently, to solve the problem of negative scattering cross-sections. Unfortunately, as we have seen, each has its major drawbacks. This research has attempted to stay true to the physics, and, in so doing, has avoided the need for complicated interpolations, or negative fix-ups to correct for computational complexities. The result is a method that has significant advantages over its predecessors, is simple to implement and provides quality results.

By just examining the scattering matrices themselves, we've shown that the MC facet method creates a T-Matrix that

- is consistent with the physics,
- has an easily adjustable accuracy,
- guarantees non-negative cross sections,
- guarantees within group and next group scatter, and
- can be rebalanced to conserve the first angular moment of the scatter.

By examining the use of the T-Matrix in a discrete ordinates transport code we've shown that the method can

- reduce scalar flux errors (as compared to SH methods) particularly for comparable low numbers of ordinates,
- facilitate the use of MCSN-like codes to use multi-group anisotropic scattering data,
- improve performance for fine energy groups,
- easily accommodate single, mixed and multiple materials, and
- be used by transport codes employing the EC method for deep penetration problems.

Overall the method promises to be viable for neutral particle transport of all types, including photon transport. Any transport scatter that can be modeled with MCNP can be modeled using the MC facet method.

Appendix A: Sample Mean Monte Carlo Integration

This appendix provides a brief overview of sample mean MC integration. This technique is applied to the average scattering integral to calculate the T-matrix. The description here is completely general and follows the description of Kalos³⁷.

We wish to evaluate an integral of the form

$$G = \int_a^b g(x)f(x)dx \quad (199)$$

where

$$f(x) \geq 0, \quad \int_a^b f(x)dx = 1. \quad (200)$$

Sample the probability distribution function, $f(x)$, to obtain a set of variables $X_1, X_2, X_3, \dots, X_N$, and form the arithmetic mean

$$G_N = \frac{1}{N} \sum_i g(X_i) = G + \delta G_N. \quad (201)$$

It is assumed that $\sigma_{G_N}^2$, and G_N are normally distributed (by the law of large numbers). Thus, the uncertainty estimate can be specified using confidence intervals. For example, there is a 90% chance that

$$|\delta G_N| \leq 1.65 \frac{\sigma}{\sqrt{N}} \quad (202)$$

where

$$\sigma^2 = \int_a^b g^2(x)f(x)dx - G^2. \quad (203)$$

Reapplying MC integration to this integral, the error estimate of the solution is

$$\sigma_N \cong \left[\left(\frac{1}{N} \sum_i g_i^2 \right) - \left(\frac{1}{N} \sum_i g_i \right)^2 \right]^{1/2}, \quad (204)$$

or

$$|\delta G_N| \leq 1.65 \frac{\left[\left(\frac{1}{N} \sum_i g_i^2 \right) - \left(\frac{1}{N} \sum_i g_i \right)^2 \right]^{1/2}}{\sqrt{N}}. \quad (205)$$

The corresponding multiplier for a 95% confidence is 1.96, and for a 99% confidence, 2.58.

If $f(X)$ does not appear explicitly in the integral, one can simply use $f(x) = 1/(b-a)$ and $g(x) = (b-a) \times \text{integrand}$. This choice of $f(x)$ requires a uniform random sampling in $[a, b]$. It is easily implemented, but other choices can improve efficiency by reducing σ^2 . This is a fundamental variance reduction scheme. For more information concerning variance reduction the reader is referred to Kalos³⁶ or Lewis & Miller¹.

Appendix B: The Inelastic Neutron Scattering Laws of MCNP

The full list of neutron scattering laws employed by MCNP follows.

1. Equi-probable energy bins (Law 1)
2. Discrete photon energy (Law 2)
3. Tabular Distribution (Laws 4 & 44)
4. General evaporation spectrum (Law 5)
5. Simple Maxwell fission spectrum (Law 7)
6. Evaporation Spectrum (Law 9)
7. Energy Dependent Watt Spectrum (Law 11)
8. Tabular linear functions (Law 22)
9. Equiprobable energy multipliers (Law 24)
10. N-body phase space distribution (Law 66)
11. Correlated energy-angle scattering (Law 67)

Other special handling techniques include

Fission Inelastic Scattering

$S(\alpha, \beta)$ Thermal Scattering

MCNP also includes photon and charged particle interactions. The MC facet approach can readily be applied to these other interactions.

Appendix C: Scattering Levels of Oxygen (^{16}O)

Oxygen-16: Level Inelastic Energy Loss in Collision

Level	Q
n, n1	-6.0494
n, n2	-6.12989
n, n3	-6.9171
n, n4	-7.11685
n, n5	-8.8719
n, n6	-9.585
n, n7	-9.8445
n, n8	-10.356
n, n9	-10.957
n, n10	-11.08
n, n11	-11.0967
n, n12	-11.26
n, n13	-11.52
n, n14	-11.6
n, n15	-12.049
n, n16	-12.44
n, n17	-12.53
n, n18	-12.796
n, n19	-12.9686
n, n20	-13.15
n, n21	-13.45
n, n22	-13.75
n, n23	-14.05
n, n24	-14.35
n, n25	-14.65
n, n26	-14.95
n, n27	-15.25
n, n28	-15.55
n, n29	-15.85
n, n30	-16.15
n, n31	-16.45
n, n32	-16.75
n, n33	-17.05
n, n34	-17.35
n, n35	-17.65
n, n36	-17.95
n, n37	-18.25
n, n38	-18.55

Appendix D: LANL 30 Group Structure

Energies for the LANL 30 group structure are in eV.

1.39E-04	1.52E-01	4.14E-01	1.13E+00	3.06E+00
8.32E+00	2.26E+01	6.14E+01	1.67E+02	4.54E+02
1.24E+03	3.35E+03	9.12E+03	2.48E+04	6.76E+04
1.84E+05	3.03E+05	5.00E+05	8.23E+05	1.35E+06
1.74E+06	2.23E+06	2.87E+06	3.68E+06	6.07E+06
7.79E+06	1.00E+07	1.20E+07	1.35E+07	1.50E+07

Appendix E: VITAMIN-J 175 Group Structure

Energies for the VITAMIN-J group structure are in eV.

1.00E-05				
1.00E-01	4.14E-01	5.32E-01	6.83E-01	8.76E-01
1.13E+00	1.45E+00	1.86E+00	2.38E+00	3.06E+00
3.93E+00	5.04E+00	6.48E+00	8.32E+00	1.07E+01
1.37E+01	1.76E+01	2.26E+01	2.90E+01	3.73E+01
4.79E+01	6.14E+01	7.89E+01	1.01E+02	1.30E+02
1.67E+02	2.14E+02	2.75E+02	3.54E+02	4.54E+02
5.83E+02	7.49E+02	9.61E+02	1.23E+03	1.58E+03
2.03E+03	2.25E+03	2.49E+03	2.61E+03	2.75E+03
3.04E+03	3.35E+03	3.71E+03	4.31E+03	5.53E+03
7.10E+03	9.12E+03	1.03E+04	1.17E+04	1.50E+04
1.93E+04	2.19E+04	2.36E+04	2.42E+04	2.48E+04
2.61E+04	2.70E+04	2.85E+04	3.18E+04	3.43E+04
4.09E+04	4.63E+04	5.25E+04	5.66E+04	6.74E+04
7.20E+04	7.95E+04	8.25E+04	8.65E+04	9.80E+04
1.11E+05	1.17E+05	1.23E+05	1.29E+05	1.36E+05
1.43E+05	1.50E+05	1.58E+05	1.66E+05	1.74E+05
1.83E+05	1.93E+05	2.02E+05	2.13E+05	2.24E+05
2.35E+05	2.47E+05	2.73E+05	2.87E+05	2.95E+05
2.97E+05	2.98E+05	3.02E+05	3.34E+05	3.69E+05
3.88E+05	4.08E+05	4.50E+05	4.98E+05	5.23E+05
5.50E+05	5.78E+05	6.08E+05	6.39E+05	6.72E+05
7.07E+05	7.43E+05	7.81E+05	8.21E+05	8.63E+05
9.07E+05	9.62E+05	1.00E+06	1.11E+06	1.16E+06
1.22E+06	1.29E+06	1.35E+06	1.42E+06	1.50E+06
1.57E+06	1.65E+06	1.74E+06	1.83E+06	1.92E+06
2.02E+06	2.12E+06	2.23E+06	2.31E+06	2.35E+06
2.37E+06	2.39E+06	2.47E+06	2.59E+06	2.73E+06
2.87E+06	3.01E+06	3.17E+06	3.33E+06	3.68E+06
4.07E+06	4.49E+06	4.72E+06	4.97E+06	5.22E+06
5.49E+06	5.77E+06	6.07E+06	6.38E+06	6.59E+06
6.70E+06	7.05E+06	7.41E+06	7.79E+06	8.19E+06
8.61E+06	9.05E+06	9.51E+06	1.00E+07	1.05E+07
1.11E+07	1.16E+07	1.22E+07	1.25E+07	1.28E+07
1.35E+07	1.38E+07	1.42E+07	1.46E+07	1.49E+07
1.57E+07	1.65E+07	1.69E+07	1.73E+07	1.96E+07

References

- 1 Lewis, E.E. and W.F. Miller, *Computational Methods of Neutron Transport*, American Nuclear Society, Inc., La Grange Park, IL, p. 42, (1993).
- 2 Bell, G.I. and S. Glasstone, *Nuclear Reactor Theory*, Van Nostrand Reinhold Company, (1970).
- 3 Greene, N.M. and J.L. Lucias, "Simple and Efficient Schemes for Processing ENDF/B Scattering Data", *Tr. Am. Nucl. Soc.*, v. 27, p. 395, (1977).
- 4 MacFarlane, R.E. and D.W. Muir, "The NJOY Nuclear Data Processing System, Version 91", Los Alamos National Laboratory, LA-12740, (Oct 1994).
- 5 Brockman, H., "Treatment of Anisotropic Scattering in Numerical Neutron Transport Theory", *Nuclear Science and Engineering*, v. 77, p. 377-414, (1981).
- 6 Dahl, Jon A., "A Non-Linear Method for Representing the Scattering Cross Section for Discrete Ordinates", *Joint International Conference on Mathematical Methods and Supercomputing for Nuclear Applications*, v. 2, p. 1497-1506, American Nuclear Society, Saratoga Springs, (Oct 1997).
- 7 Miller, R.L., "Development of an HPF-Parallel Radiation Transport Code System for Unstructured Meshes of Tetrahedral Cells", Dissertation, Air Force Institute of Technology, AFIT/DS/ENP/98-02, (1998).
- 8 Wareing, T.A. and R.E. Alcouffe, "An Exponential Discontinuous Scheme for X-Y-Z Geometry Transport Problems", *Proceedings of the 1996 Topical Meeting Radiation Protection and Shielding*, v. 1, p. 597-604, American Nuclear Society, La Grange Park, IL, (1996).
- 9 Beraneck, F. and R.W. Conn, "Discrete Cross-Section Expansions for Discrete Ordinates Code," *Trans. Nuc. Soc.*, v. 28, p. 663, (1978).
- 10 Odom, J.P., "Neutron Transport with Highly Anisotropic Scattering" Ph.D. Dissertation, Kansas State University, Manhattan, KS, (1975).
- 11 Mikols, W.J. and J.K. Shultis, "Selection of Angular Quadrature for Anisotropic Transport Computations", *Nuclear Science and Engineering*, v. 63, p. 91-109, (1977).

-
- 12 R.S. Baker, "The XREP Module", LA-UR-95-4473, Los Alamos National Laboratory, (1995).
 - 13 Borsari, R., Fioresi, R., Trombetti, T., "Nonnegativity of the Anisotropic Scattering Source in Two-Angle ($\mu\theta$) Transport", Nuclear Science and Engineering, v. 112, p. 301-320, (1992).
 - 14 Briesmeister, J.F., editor, "MCNP--A General Monte Carlo N-Particle Transport Code", Los Alamos National laboratory, LA-12625-M, Version 4B, (Mar 1997).
 - 15 Drake, M.K., "Data Format Procedures for the ENDF Neutron Cross Section Library," BNL-50279, Battelle Northwest Labs. (Oct 1970).
 - 16 Steinacker, J. Thamm, E. and Maier, U., "Efficient Integration of Intensity Functions on the Unit Sphere", Journal of Quantum Spectroscopy and Radiation Transfer, v. 56, n. 1, p. 97-107, (1996).
 - 17 Daul, C. and S. Daul, "Symmetrical "Nonproduct" Quadrature Rules for a Fast Calculation of Multicenter Integrals." International Journal of Quantum Chemistry, v. 61, p. 219-230, (1997).
 - 18 McLaren, A.D., "Optimal Numerical Integration on a Sphere", Mathematics of Computation, v. 17, n. 84, (Oct 1963).
 - 19 Lebedev, V.I., "Quadratures on a Sphere", Zh. Vychisl. Mat. Mat. Fiz., v. 16, n. 2, p. 293-306, (1976).
 - 20 Press, W.J., et. al. *Numerical Recipes in Fortran 90, The Art of Parallel Scientific Computing*, 2nd ed., Cambridge University Press, (1996).
 - 21 Marchuck, G.I. and V.I. Lebedev, *Numerical Methods in the Theory of Neutron Transport*, Revised 2nd Edition, Hardwood Academic Publishers, (1986).
 - 22 Duderstadt, J.J. and W.R. Martin, *Transport Theory*, John Wiley & Sons, New York, (1979).
 - 23 Drumm, C.R., "Multidimensional Electron-Photon Transport with Standard Discrete Ordinates Codes", Nuclear Science and Engineering, v. 127, p. 1-21, (1997).
 - 24 Mathews, K.A. and M. Suriano, "MCSN—A Monte Carlo S_N Transport Method", Currently under development at AFIT, (1999).

-
- 25 National Nuclear Data Center, Brookhaven National Laboratory, www.nndc.bnl.gov, (1999).
 - 26 T-2 Nuclear Information Service, Los Alamos National Laboratory, t2.lanl.gov/homepage.html, (1999).
 - 27 V. McLane and others "ENDF-102: Data formats and Procedures for the Evaluated Nuclear Data File ENDF-6," BNL report, BNL-NCS-44945, revised, (1995).
 - 28 R.E. MacFarlane, "TRANSX 2: A Code for Interfacing MATXS Cross-Section Libraries to Nuclear Transport Codes", LA-12312-MS, Los Alamos National Laboratory, (July 1992).
 - 29 Larsen , E. W. and R. E. Alcouffe, "The Linear Characteristic Method for Spatially Discretizing the Discrete Ordinates Equations in (X, Y) Geometry", LA-10092-T, Los Alamos National Laboratory, (1981).
 - 30 De Boor, C., *A Practical Guide to Splines*, Springer-Verlag, p. 332-346, also SPLI2D, p. 347-349, (1978).
 - 31 Hong, K.J. and J.K. Shultis, "Accurate Evaluation of Multigroup Transfer Cross Sections and their Legendre Coefficients," Nuclear Science and Engineering, v. 80, p. 570-578, (1982).
 - 32 Davis, P.J. and Rabinowitz, P., *Methods of Numerical Integration*, 2nd ed, Academic Press, San Diego, p. 387, (1984).
 - 33 Mathews, K., Sjoden, G. et al, "Exponential Characteristic Spatial Quadrature for Discrete Ordinates Radiation Transport in Slab Geometry." Nuclear Science and Engineering, v. 118, p. 24-37, (1994).
 - 34 Brennan C.R. "Characteristic Spatial Quadratures for Discrete Ordinates Neutral Particle Transport on Arbitrary Tetrahedral Meshes", Ph.D. Dissertation, Air Force Institute of Technology, AFIT/DS/ENP/96-01, (Jun 1996).
 - 35 Mathews, K.A., and B.M. Minor, "Adaptive Characteristic Spatial Quadratures for Discrete Ordinates Neutral Particle Transport-The rectangular cell case", Transport Theory and Statistical Physics, v. 22, p. 655-686, (1993).
 - 36 Kalos, M.H. and P.A. Whitlock, *Monte Carlo Methods*, vI, John Wiley & Sons, New York, p. 89, (1986).

VITA

J. Mark DelGrande graduated from Oregon State University with a B.S. in Engineering Physics in 1985. He was a distinguished graduate from Air Force ROTC that same year. He was assigned directly to the Air Force Institute of Technology, School of Engineering, Dayton, Ohio. He graduated with an M.S. in Engineering Physics in 1986. He was assigned as a neutral particle beam research officer to the Advanced Weapons Directorate, Air Force Weapons Laboratory, Kirtland AFB, New Mexico from 1986-1988. In 1989, he left space weapons to work as a high power microwave research officer for the newly formed Phillips Laboratory. In 1991, he was selected as a Military Research Associate for the Air Force Office of Scientific Research at Lawrence Livermore National Laboratory. While at Livermore, he worked with the Photonics Group of the Nuclear Test Experimental Science Division. In 1994, he was assigned as an instructor for the Physics Department of the United States Air Force Academy where he was later chosen to be an Assistant Professor of Physics. He was assigned, once again, to the Air Force Institute of Technology, Department of Engineering in 1996 to pursue a Ph.D. in nuclear engineering. Upon graduation, he will be assigned to Los Alamos National Laboratory, X-Division, for the Defense Threat Reduction Agency.

REPORT DOCUMENTATION PAGE			Form Approved OMB No. 0704-0188	
Public reporting burden for this collection of information is estimated to average 1 hour per response, including the time for reviewing instructions, searching existing data sources, gathering and maintaining the data needed, and completing and reviewing the collection of information. Send comments regarding this burden estimate or any other aspect of this collection of information, including suggestions for reducing this burden, to Washington Headquarters Services, Directorate for Information Operations and Reports, 1215 Jefferson Davis Highway, Suite 1204, Arlington, VA 22202-4302, and to the Office of Management and Budget, Paperwork Reduction Project (0704-0188), Washington, DC 20503.				
1. AGENCY USE ONLY (Leave blank)		2. REPORT DATE September 1999		3. REPORT TYPE AND DATES COVERED Doctoral Dissertation
4. TITLE AND SUBTITLE POSITIVE ANISOTROPIC GROUP SCATTERING CROSS SECTIONS FOR RADIATION TRANSPORT			5. FUNDING NUMBERS	
6. AUTHOR(S) J. Mark DelGrande, Major, USAF				
7. PERFORMING ORGANIZATION NAME(S) AND ADDRESS(ES) Air Force Institute of Technology 2750 P Street Wright Patterson AFB, OH 45433-7765			8. PERFORMING ORGANIZATION REPORT NUMBER AFIT/DS/ENP/99-03	
9. SPONSORING/MONITORING AGENCY NAME(S) AND ADDRESS(ES) L. Wayne Brasure, Lt Col, USAF DTRA/NSN MS L-096 Lawrence Livermore National Laboratory, CA 94550-9234 925-422-3717			10. SPONSORING/MONITORING AGENCY REPORT NUMBER	
11. SUPPLEMENTARY NOTES				
12a. DISTRIBUTION AVAILABILITY STATEMENT Approved for public release; Distribution unlimited.			12b. DISTRIBUTION CODE	
13. ABSTRACT (Maximum 200 words) <p>In solving the Boltzmann transport equation, most discrete ordinates codes calculate the source term by first approximating the scattering cross section using a Legendre polynomial expansion. Such expansions are insufficient when scattering is anisotropic and the Legendre expansion is truncated prematurely. This can lead to nonphysical negative cross sections, negative source terms and negative angular fluxes. While negative sources are problematic for standard discrete ordinates methods leading to poor convergence or convergence to incorrect results, they are of particular concern to exponential methods, causing such calculations to fail.</p> <p>We've developed and tested a new technique to solve this problem called the Monte Carlo Facet Method. This method is an extension of standard Monte Carlo techniques. It guarantees non-negative cross sections at all directional ordinates. It also ensures within group and next group scatter.</p> <p>This dissertation outlines previous attempts to handle anisotropic scattering to achieve non-negative sources. It develops the theory of the Monte Carlo facet method and its first angular moment conservation. Results are presented examining the scattering matrices for various materials, and finally demonstrating that these scattering matrices perform exceptionally well in a multi-group, anisotropic, unstructured mesh discrete ordinates transport code.</p>				
14. SUBJECT TERMS Discrete Ordinates; Monte Carlo Method; Cross Sections; Neutron Transport Theory, Radiation Shielding			15. NUMBER OF PAGES 205	
			16. PRICE CODE	
17. SECURITY CLASSIFICATION OF REPORT UNCLASSIFIED	18. SECURITY CLASSIFICATION OF THIS PAGE UNCLASSIFIED	19. SECURITY CLASSIFICATION OF ABSTRACT UNCLASSIFIED	20. LIMITATION OF ABSTRACT UL	